Controlling and Imaging Molecular Motion at the Surface of a Gate-Tunable Graphene Device

By

Franklin Liou

A dissertation submitted in partial satisfaction of the

requirements for the degree of

Doctor of Philosophy

in

Physics

in the

Graduate Division

of the

University of California, Berkeley

Committee in charge:

Professor Michael F. Crommie, Chair
Professor Feng Wang
Professor Kwabena Bediako

Fall 2022

Abstract

Controlling and Imaging Molecular Motion at the Surface of a Gate Tunable Graphene Device

By

Franklin Liou

Doctor of Philosophy in Physics

University of California, Berkeley

Professor Michael F. Crommie, Chair

The ability to control nanoscale molecular motion with device-scale electric fields opens many exciting possibilities for nanotechnology. Collective motion of molecules can be used to assemble new nanostructures, induce mass and charge transport, transform device properties by surface modifications, and can potentially be used as a tool for constructing nanoscale machines. As components for electromechanical devices approach the nanometer length scale, how they interact with local electric fields and currents becomes increasingly important. This dissertation focuses on exploring how macroscopic electric fields and currents can manipulate and probe the collective motion of adsorbed molecules on gate-tunable devices.

The movement of F_4TCNQ molecules on a graphene field-effect transistor was controlled by the application of a gate voltage and source-drain current, and concurrently imaged using a scanning tunneling microscope. Various field-induced molecular phenomena were investigated on the device, including gate-tunable surface molecular concentrations, gate-tunable molecular phase transitions, gate-dependent molecular diffusion, molecule density-dependent current transport, and current-induced electromigration. These phenomena provide insight into how nanoscale molecular motion can be controlled by external electric fields, and how force and momentum are transmitted between electrons and adsorbates under non-equilibrium conditions.

Acknowledgements

"A Ph.D. is an arduous journey with an uncertain outcome." I once heard the phrase at a commencement ceremony, and it has been stuck in my mind ever since. Throughout most of my graduate career, I faced much uncertainty: uncertainty about my research direction, uncertainty about whether the research I am pursuing will bear fruit, and also uncertainty brought on by the COVID-19 pandemic, which seemed to have come out of nowhere and disrupted our lives all of a sudden. Fortunately, throughout these uncertain times, I have had the unwavering support and guidance of some of the smartest, most knowledgeable, patient and kind people to help me successfully navigate through uncertainty and finish this work. I owe the completion of this dissertation to the following people:

First of all, Professor Mike Crommie, who gave me the opportunity to work in his lab and provided guidance to my projects. Mike is the most enthusiastic and encouraging advisor I've had the privilege to work with. I often leave our Friday meetings feeling rejuvenated and excited about my work, ready to chase down new questions raised during our discussions.

I also want to thank fellow graduate student and post-doc Hsin-Zon Tsai, with whom I've worked most closely with for 6 years, and from whom I learned most experimental techniques, including STM, AFM and graphene sample fabrication. I'd like to thank fellow graduate student Andrew Aikawa and undergrad Brian Angeles, who helped with developing the codebase used to analyze molecular motion. I'd like to thank our theory collaborators Professor Johannes Lischner and graduate student Zachary Goodwin for helping me understand the gate-tunable molecular density, phase transition, and molecular diffusion results. I'd also like to thank Young Woo Choi, Sehoon Oh, Dimitry Solenov and Jerry Tersoff for collaborative work on explaining the molecular electromigration phenomenon that we have observed.

I'd like to thank some group members with whom I've worked closely with, and who have helped me in my daily research, fixing the STM, analyzing data, providing helpful discussions, assisting me in experiments, and writing papers with me: graduate students Yiming Yang, Giang Nguyen, post-docs Shaowei Li, Tiancong Zhu, Vida Jamali, Wei Ruan. I'd also like to thank Salman Khan for showing me how to use shadow masks to make graphene devices. I want to especially thank undergrads Kyler Natividad, Ethan Ha, Eric Tang, Michael Hu, Kevin Qi, who helped prepare vital graphene samples. My experiments would not have been possible without their diligent contributions making countless graphene devices.

There are also others in the group who I sometimes work with or discuss things with, who have made life in the lab more enjoyable: Dillon Wang, Chen Chen, Zahra Pedramrazi, Kacey Meaker, Trinity Joshi, Dan Rizzo, Yi Chen, Juwon Lee, Canxun Zhang, Zehao He, Ziyi Wang, and Peter Jacobse.

I'd like to thank Professor Alex Zettl, Professor Feng Wang, and Professor Kwabena Bediako for listening to my talks and giving useful feedback on my projects.

I'd also like to thank the staff in the physics department for advising me, providing administrative assistance, ensuring all the paperwork is completed, shipping and receiving my samples and materials: Anne Takizawa, Donna Sakima, Joelle Miles, Claudia Trujillo, Carlos Bustamante, and Anthony Vitan.

I'd like to give special thanks to Philip, Victoria, and Emma Huie for all their support during my years at Berkeley, and for sending me care packages and homemade food.

Finally, I am grateful towards my parents, Teh-Suan Liou and Hui-Ling Liou Chang, who have inspired, encouraged and always supported me. I owe everything I've achieved to you.

Table of Contents

1 Introduction *1*

1.1 Manipulating Matter at the Nanoscale **1**

1.2 Graphene as a Substrate for Atomic Manipulation **2**

1.3 Dissertation Overview **3**

2 Scanning Tunneling Microscopy *4*

2.1 General Expression for Tunneling **4**

2.2 Scanning Tunneling Microscope Operation **8**

2.3 Scanning Tunneling Potentiometry **9**

3 Theoretical Background for Molecule-decorated Graphene Devices *11*

3.1 Graphene as a Gate-tunable Substrate **11**

3.1.1 Electronic Properties of Graphene 11

3.1.2 Graphene Field-effect Devices 16

3.2 Adsorbates on Graphene **17**

3.2.1 Fermi Level Pinning 17

3.2.2 Green's Functions, LDOS, PDOS, and Hybridization 19

3.2.3 Phase Transitions of Molecular Adsorbates on Surfaces 23

3.2.4 Solid, Liquid and Gas Phases in Two Dimensions 26

3.3 Electron Transport and Impurity Scattering in Graphene **28**

3.3.1 Boltzmann Transport Theory and Conductivity 28

3.3.2 Charged Impurity Scattering in Graphene 32

3.3.3 Resonant Impurity Scattering in Graphene 36

3.4 Diffusion and Electromigration of Surface Adsorbates **39**

3.4.1 Brownian Diffusion 39

3.4.2 Electromigration 41

3.4.3 Non-equilibrium Green's Function (NEGF) Calculations in Electromigration 47

3.4.4 Experimental Measurement of Electromigration Force 49

4 Gate-tunable Molecular Concentration on a Graphene FET *51*

4.1 Introduction **51**

4.2 Methods **52**

4.3 Results **52**

4.4 Discussion **56**

4.5 Conclusion **60**

5 Gate-tunable Molecular Phase Transitions on a Graphene FET *61*

5.1 Introduction **61**

5.2 Methods **62**

5.3 Results **62**

5.4 Discussion **65**

5.5 Conclusion **71**

6 Gate-tunable Molecular Diffusion on a Graphene FET 72

6.1 Introduction 72

6.2 Methods 73

6.3 Results 73

6.4 Discussion 78

6.5 Conclusion 82

7 Resonant Transport in molecule-decorated Graphene Devices 83

7.1 Introduction 83

7.2 Methods 84

7.3 Results 85

7.4 Discussion 88

7.5 Conclusion 89

8 Electromigration of single-molecule adsorbates 90

8.1 Introduction 90

8.2 Methods 91

8.3 Results 91

8.4 Discussion 95

8.5 Conclusion 99

9 Conclusion 100

Appendix A: Capacitive navigation in STM 101

Appendix B: Fitting the Dirac Point Energy from STS 103

Bibliography 104

List of Figures and Tables

Fig. 2.1: Tip and sample Fermi levels under an external bias. 8
Fig. 2.2: Basic setup of a STM. 9
Fig. 2.3: Scanning tunneling potentiometry setup. 10
Fig. 3.1: Real and reciprocal space structure of graphene. 12
Fig. 3.2: π-band structure of graphene. 13
Fig. 3.3: Density of state of graphene. 16
Fig. 3.4: A graphene/hBN field-effect transistor. 17
Fig. 3.5: Fermi level pinning mechanism. 19
Table 3.1: Summary of thermodynamic free energies in closed systems. 24
Fig. 3.6 Shell-like structure of liquids. 27
Fig. 3.7 Two-dimensional solid, liquid, and gas phases. 27
Fig. 3.8 Fermi surface shift under an externally applied electric field. 31
Fig. 3.9 Graphene conductance in Boltzmann transport. 36
Fig. 3.10 Hybridized graphene impurity bands in the continuum model. 38
Fig. 3.11 Conductivity of impurity-decorated Graphene. 39
Fig. 3.12 Hole wind arising from imbalance of states with left- and right-pointing momenta. 43
Fig. 3.13 Schematic of electron scattering in the Landauer transport model. 46
Fig. 3.14 Origin of the Landauer resistivity dipole. 47
Fig. 4.1 Controlling molecular concentration on a graphene field-effect transistor 53
Fig. 4.2 Tuning molecular concentration by using FET gate voltage 53
Fig. 4.3 STM spectroscopy of F_4TCNQ-decorated graphene field-effect transistor 55
Fig. 4.4 Gate-dependence of the graphene Dirac point energy before molecule deposition. 57
Fig. 4.5 Fermi level pinning of F_4TCNQ-doped graphene field-effect transistor. 58
Fig. 5.1 Gate-tunable solid-liquid molecular phase transition. 63
Fig. 5.2 Electronic energy level alignment between graphene and F_4TCNQ molecules, and charge accumulation under electrostatic gating. 64
Fig. 5.3 F_4TCNQ chain freezing and melting under non-equilibrium conditions. 69
Fig. 5.4 Non-equilibrium melting of the F_4TCNQ solid. 71
Fig. 6.1: Tracking molecular diffusion on a graphene surface 74
Fig. 6.2 Gate-dependent molecular diffusion barrier. 74
Fig. 6.3 Gate-dependent molecular displacements during diffusion 77
Fig. 6.4 Schematic of molecular diffusion paths. 79
Fig. 6.5 Molecular diffusion barriers calculated from DFT and diffusion probability maps. 81
Fig. 7.1 Conductance measurement experimental setup. 85
Fig. 7.2 Molecule density on graphene as a function of V_{G-set}. 85
Fig. 7.3 Gate-dependent conductivity of a F_4TCNQ-decorated graphene device as a function of V_{G-set} 87
Fig. 8.1 Electromigration experimental setup. 91
Fig. 8.2 Current-polarity dependent migration of molecules. 92
Fig. 8.3 Molecular trajectories during electromigration. 93

Fig. 8.4 Average drift velocity of molecules.......94
Fig. 8.5 Scanning tunneling potentiometry measurement of the in-plane electric field.......95
Fig. 8.6 Schematic of electron scattering processes in a normal semiconductor and graphene.......97
Fig. 8.7 Atomic structure of the DFT-NEGF calculation......98
Fig. 8.8 Calculated charge distribution obtained from NEGF.......99
Fig. A1. Capacitive pickup current measurement setup.......101
Fig. A2. Graphene device imaged by SEM and capacitive pickup......102

1 Introduction

1.1 Manipulating Matter at the Nanoscale

In his 1959 lecture *There's Plenty of Room at the Bottom*, Feynman invited his audience to venture into the new science of miniaturization, where tiny machines could hypothetically be built and operated using only a small fraction of materials usually needed. A prerequisite of manufacturing such tiny machines is solving the problem of "manipulating and controlling things on a small scale."[1] In the 60 years that have since passed, scientists have answered Feynman's challenge by demonstrating numerous ways to control and image matter at the atomic scale, one of which is scanning tunneling microscopy (STM), where an atomically sharp tip can be used to nudge and pull atoms on a surface to form desired structures. This development has allowed surface scientists to assemble matter in new and interesting ways, enabling the creation of quantum corrals,[2,3] artificial electronic states,[4] and even cascade machines that can be triggered with a slight push from a STM tip.[5,6] Although the STM has effectively provided an "arm" to precisely manipulate matter at the nanoscale, its drawbacks also come from the limited range of the tip's influence, making it less useful as a tool for operating larger and more complex nanomachines. On the other hand, large-scale manipulation of atomic and molecular adsorbates by macroscopic electric fields has long been a core part of electrochemical technologies such as electrocatalysis,[7,8] batteries,[9] supercapacitors,[10,11] neuromorphic devices,[12,13] and electrochemical sensors.[14,15] Interactions between ions and their electrochemical environment are known to induce controllable collective motion on electrode surfaces, such as switching in self-assembly geometries[16–18] and ion migration.[19,20] It is thus natural that state-of-the-art STM has progressed towards probing nanoscale systems while they are being actively driven by external stimuli such as current,[21–25] electric fields,[5,26–28] and light.[29,30]

While nanomachines can conceivably be operated by an electrochemical system, complicated electrolytic environments pose a challenge for imaging nanoscale motion.[31–33] To be able to image atoms and molecules with high resolution under dynamically changing surface configurations, STM imaging is typically done in ultra-high vacuum (UHV). To manipulate surface adsorbates in UHV, electric fields are not applied through an electrolyte, but through electrostatic gating and surface currents in a solid-state device. One example of such a system, which will be a main topic of this dissertation, uses a graphene field effect transistor to control the motion of F_4TCNQ molecules deposited on its surface.[34] Such devices can be used to push molecules around via macroscopic electric fields and currents while concurrently allowing a STM to take atomically-resolved images of the surface. Insights gained from observing such externally driven molecular motion can help us understand how energy, force, and momentum are transmitted at the nanoscale, something of fundamental importance to the operation of nanomachines.

As the components of a machine are shrunk down to ever smaller sizes, their mechanical and electronic properties become vastly different from bulk materials, so there is a need to re-evaluate the principles of motion at the nanoscale. For instance, electric fields permeate materials with reduced dimensionality more easily,[35,36] which can lead to stronger interactions that influence the diffusive motion of molecules on surfaces. Surface atomic corrugation also causes adsorbates to settle into one of a few discrete energetically stable geometries. Perhaps most importantly for electrically-operated nanomachines, the laws of motion are drastically different for electrons and adsorbates, the electron being a quantum mechanical object described by waves, and the atom being a more classical object with more well-defined position and momentum. There is thus a need to rethink how force is transmitted from one object to the other at the nanoscale. Just as understanding fluid mechanics is important for the design of wind turbines, so too is understanding nanoscale force transmission crucial for designing functional nanomachines.

Moreover, machines are devices that turn energy into useful motion. In order for a nanomachine to produce useful motion it must have controllable interactions: essentially the knobs and switches by which the machine is operated. In a molecule-based nanomachine, such controllable interactions can be provided by molecular orbitals which fill or empty of charge based on external stimuli. Such charge-tunable molecules can produce motion through structural bending,[37] rotation,[38] and even via different self-assembly geometries.[17] Molecule-molecule interactions as well as molecule-substrate interactions can also potentially be adjusted by tuning molecular charge through gating.

Lastly, molecules form ideal building blocks for nanomachines since molecular properties are highly tunable through functionalization. Components of different shapes and sizes can conceivably be synthesized to produce different functions, and even linked together to perform complex motion. The versatility of molecular components is one of the reasons molecules of all shapes and sizes can be found throughout nature's most complex biological nanomachines such as ribosomes and motor proteins. Current nanotechnology based on synthetic nanomachines comes nowhere close to the complexity of biological nanomachines. However, as our understanding of nanoscale motion improves, and as new ways to control matter at the nanoscale are developed, one can imagine a day when nanomachines that approach biological nanomachines in functionality and complexity are routinely manufactured.

1.2 Graphene as a Substrate for Atomic Manipulation

Graphene, a single atomic-layer of carbon known for its unique electronic properties, is an ideal substrate for studying molecular adsorbates because of its tunable charge density,[39] atomic flatness, and weak adhesion force to most adsorbed molecules.[40] Due to graphene's low density of states near charge neutrality, its Fermi level can be easily tuned by either electrostatic gating or chemical doping. This means that if a molecular orbital lies close enough in energy to the graphene Fermi level, charges can be either injected or removed from the molecular orbital. Molecule-substrate interactions such as charge screening and adhesion forces can also be adjusted as a result of the tunable Fermi level. Graphene is also atomically flat, especially when layered onto a hexagonal boron nitride (hBN) substrate, so it provides an ideal platform for observing unimpeded motion of molecules. Furthermore, graphene can adsorb many types of molecules, some covalently bound such as NO_2,[14] hydrogen,[41] and oxygen,[42] and others bound by van der Waals interactions such as porphyrins[43] and F_4TCNQ.[26] Molecules which are only loosely bound to the surface remain mobile at low temperatures, and are thus ideal for control and characterization via low-temperature STM.

1.3 Dissertation Overview

This dissertation will address the following questions:

1. How can we control collective molecular motion at the nanoscale?
2. How do adsorbates behave when we change their charge state on a surface?
3. How is force and momentum transmitted between electrons and adsorbates under non-equilibrium conditions?

The main findings of this work are that molecules which have tunable charge states can reconfigure their spatial configuration in response to externally applied electric fields in a predictable way. In particular, charge-carrying molecules can reposition themselves in order to screen external electric fields, thus causing the Fermi level of the substrate to become pinned to molecular energy levels. On graphene, charged molecules tend to disperse uniformly on the surface due to Coulomb repulsion, while uncharged molecules can self-assemble into different types of geometries due to van der Waals interactions. Under non-equilibrium conditions, such as when a current is passed through the substrate, electrons can scatter off potentials created by adsorbates and thus create a wind force that pushes adsorbates forward. The direction and magnitude of the wind force depend on the particular scattering potential that an adsorbate creates.

The overall structure of this dissertation is as follows:

The main experimental method used here to investigate molecular motion is STM, and so the fundamental operating principles of STM and its various imaging modes will be introduced in chapter 2.

An introduction to the background necessary for understanding the various molecular phenomena presented in this work is given in chapter 3, including descriptions of the electronic properties of graphene, gate-tunable graphene devices, adsorbates on graphene, electron transport and scattering in graphene, surface diffusion processes, and electromigration.

In chapter 4, I present one of the main findings of this work, a novel phenomenon where the surface density of F_4TCNQ molecules can be tuned by electrostatically gating a graphene device. The mechanism of adjustable surface molecule density will be further explained in chapter 5 by the existence of self-assembled molecular structures that function as molecular reservoirs in this capacity.

In chapter 6, a closer look at the diffusion processes of F_4TCNQ molecules on graphene is presented, which reveals that the diffusion paths taken by molecules are highly sensitive to electrostatic gating as well.

In chapter 7, the conductance of F_4TCNQ-decorated graphene devices will be presented as a function of applied gate voltage, and I will show that the microscopic surface configurations of molecules induce coherent changes in the devices' conductivity observable at a macroscopic scale.

In chapter 8, I present work on the electromigration phenomenon of F_4TCNQ molecules on graphene, where molecules are pushed along the electron current direction by electrons scattering from the molecular potential.

2 Scanning Tunneling Microscopy

This chapter introduces the basic concepts of scanning tunneling microscopy (STM), including its principle of operation and various imaging and spectroscopy modes used throughout this dissertation.

STM is an imaging technique based on detecting a small current of electrons tunneling through the vacuum between a metal tip and a conductive sample. The vacuum between the tip and sample presents a barrier to the tunneling electron, through which the electron wavefunction decays exponentially, thus leading to an extremely sensitive dependence of tunneling current on the tip-sample separation. To illustrate this principle, let us consider tunneling in a one-dimensional barrier. Solutions of the Schrödinger equation within a one-dimensional tunneling barrier of height V_B take the form of $\psi \propto e^{\pm\kappa z}$, where $\kappa = \sqrt{2m(E - V_B)/\hbar^2}$, E is the energy of the tunneling electrons, and z is the tip-sample separation. Since the tunneling current $I \propto |\psi|^2 \propto e^{-2\kappa z}$, it is very sensitive to the tip-sample separation. Because of this high spatial sensitivity, the tunneling current can be used to spatially map the topography of a conductive surface either by direct detection of the tunneling current while maintaining constant tip-sample distance (constant height mode), or by keeping the current constant while changing the tip-sample distance through a feedback loop (constant current mode). Besides topography information measured through the DC tunneling current, the local density of states of the sample can be measured through the differential conductance of the tunnel junction. The theoretical description of electron tunneling in STM was first formalized by Bardeen,[44] and then applied in a more useful form by Tersoff and Hamann.[45]

2.1 General Expression for Tunneling

To model the tunneling current, one can apply Fermi's Golden Rule to calculate the transition rate of electrons tunneling between the tip and the sample under a perturbing Hamiltonian.[46] Fermi's Golden rule states that given initial and final eigenstates ψ_i and ψ_f of the Hamiltonian H, the transition rate W from state ψ_i to state ψ_f under a perturbing Hamiltonian H' is given by

$$W_{i\to f} = \frac{2\pi}{\hbar}\left|\langle\psi_f|H'|\psi_i\rangle\right|^2 \rho(\mathcal{E}_f)\,, \tag{2.1}$$

where $\rho(\mathcal{E}_f)$ is the total density of states of the system at the energy of the final state $\mathcal{E}_f$. $\rho(\mathcal{E})$ can also be expressed as the product between the density of states of the sample $\rho_s(\mathcal{E})$ and that of the tip $\rho_t(\mathcal{E})$, so that the transition rate from tip to sample $dW_{t\to s}$ at energy $\mathcal{E}$ within an energy range $d\mathcal{E}$ can be expressed as

$$dW_{t\to s} = \frac{2\pi}{\hbar}|\langle\psi_s|H'|\psi_t\rangle|^2 \rho_s(\mathcal{E})\rho_t(\mathcal{E})d\mathcal{E}\ , \tag{2.2}$$

where ψ_s and ψ_t are sample and tip wavefunctions, respectively. Furthermore, a transition from ψ_t to ψ_s can only occur if ψ_t is occupied by an electron and ψ_s is unoccupied. Since the occupancy is given by the Fermi-Dirac distribution $f(\mathcal{E}) = 1/(e^{\frac{\mathcal{E}-\mu}{k_BT}} + 1)$, the density of states $\rho_t(\mathcal{E})$ must be multiplied by the probability that the tip state is occupied, $f(\mathcal{E})$, and the density of states $\rho_s(\mathcal{E})$ must be multiplied by the probability that the sample state is unoccupied, $1 - f(\mathcal{E})$, so that

$$dW_{t\to s} = \frac{2\pi}{\hbar}|\langle\psi_s|H'|\psi_t\rangle|^2\rho_s(\mathcal{E})[1 - f(\mathcal{E})]\rho_t(\mathcal{E})f(\mathcal{E})d\mathcal{E}\ . \tag{2.3}$$

If a voltage V is applied on the sample relative to the tip, both the density of states of the tip and its Fermi-Dirac distribution is shifted down by $|e|V$, where $|e|$ is the magnitude of the electron charge, as shown in Fig. 2.1. The transition rate now becomes

$$dW_{t\to s} = \frac{2\pi}{\hbar}|\langle\psi_s|H'|\psi_t\rangle|^2\rho_s(\mathcal{E})\ [1 - f(\mathcal{E})]\ \rho_t(\mathcal{E} - |e|V)f(\mathcal{E} - |e|V)d\mathcal{E}\ . \tag{2.4}$$

To get the total current, we must also account for electrons that tunnel back from sample states into tip states. The transition rate of such a process is

$$dW_{s\to t} = \frac{2\pi}{\hbar}|\langle\psi_t|H'|\psi_s\rangle|^2\rho_s(\mathcal{E})f(\mathcal{E})\rho_t(\mathcal{E} - |e|V)\ [1 - f(\mathcal{E} - |e|V)]d\mathcal{E}\ . \tag{2.5}$$

The total transition rate summing over all tip states ψ_μ and sample states ψ_ν is then

$$\begin{aligned} W &= \int \sum_{\mu,\nu} dW_{s\to t} - dW_{t\to s} \\ &= -\frac{2\pi}{\hbar}\int_{-\infty}^{\infty} \sum_{\mu,\nu} \left|\langle\psi_\mu|H'|\psi_\nu\rangle\right|^2 \rho_{s,\nu}(\mathcal{E})\rho_{t,\mu}(\mathcal{E} - |e|V)\ [f(\mathcal{E} - |e|V) - f(\mathcal{E})]d\mathcal{E}\,. \end{aligned} \tag{2.6}$$

The total current resulting from tunneling can then be expressed as

$$\begin{aligned} I(V) &= -|e|W \\ &= \frac{2\pi|e|}{\hbar}\int_{-\infty}^{\infty} \sum_{\mu,\nu} \left|\langle\psi_\mu|H'|\psi_\nu\rangle\right|^2 \rho_{s,\nu}(\mathcal{E})\rho_{t,\mu}(\mathcal{E} - |e|V)\ [f(\mathcal{E} - |e|V) - f(\mathcal{E})]d\mathcal{E}. \end{aligned} \tag{2.7}$$

Usually the tip density of states is relatively featureless compared to the sample for a well-prepared tip, so $\rho_t(\mathcal{E})$ can be approximated by a constant ρ_t. In addition, since spectroscopy is typically measured at low temperatures, we can approximate the Fermi-Dirac distribution as a step function, with a chemical potential of $\mathcal{E}_F$, so that the total current can be further simplified and written as

$$I(V) = \frac{2\pi|e|}{\hbar}\rho_t\int_{\mathcal{E}_F}^{\mathcal{E}_F+|e|V} \sum_{\mu,\nu} \left|M_{\mu\nu}\right|^2 \rho_{s,\nu}(\mathcal{E})\ d\mathcal{E}\ , \tag{2.8}$$

where we have denoted the Bardeen matrix elements as $\langle\psi_\mu|H'|\psi_\nu\rangle = M_{\mu\nu}$. Intuitively, one can see that only electrons with energy between $\mathcal{E}_F$ and $\mathcal{E}_F + |e|V$ contribute to the tunneling current.

The Bardeen matrix elements can be evaluated for zero bias elastic tunneling by calculating the volume or surface integrals[44]

$$M_{\mu\nu} = \frac{\hbar^2}{2m}\oint\left(\psi_{t,\mu}\nabla^2\psi_{s,\nu}^* - \psi_{s,\nu}^*\nabla^2\psi_{t,\mu}\right)d\mathbf{r}$$
$$= \frac{\hbar^2}{2m}\oint\left(\psi_{t,\mu}\nabla\psi_{s,\nu}^* - \psi_{s,\nu}^*\nabla\psi_{t,\mu}\right)\cdot\, d\mathbf{A} \quad , \tag{2.9}$$

where **A** is an area that separates the tip from the sample, typically taken to be a horizontal plane between the tip and sample.

Tersoff and Hamann calculated the Bardeen matrix element with the approximation that the tip wavefunctions are localized s-waves centered at position $(\mathbf{x}_t, z_t)$, so that the matrix element $M_{\mu\nu}$ ends up being proportional to the sample wavefunction amplitude $|\psi_s(\mathbf{x}_t, z_t)|^2$. To obtain this important result, one can expand sample states as generalized plane waves decaying in the z-direciton:

$$\psi_{s,\nu}(\mathbf{x}, z) = \int d\mathbf{q}\; a_{\mathbf{q}} e^{-\sqrt{\kappa^2+\mathbf{q}^2}z} e^{i\mathbf{q}\cdot\mathbf{x}} \,. \tag{2.10}$$

Similarly, tip states can be expanded in terms of plane waves, where $\mathbf{x}_t$ and z_t denote the in-plane and out-of-plane position of the tip:

$$\psi_{t,\mu}(\mathbf{x}, \mathbf{x}_t, z, z_t) = \int d\mathbf{q}\; b_{\mathbf{q}} e^{-\sqrt{\kappa^2+\mathbf{q}^2}(z_t - z)} e^{i\mathbf{q}\cdot(\mathbf{x}-\mathbf{x}_t)} \,. \tag{2.11}$$

Taking the surface of integration to be a horizontal plane separating the tip and sample, the tunneling matrix element can then be written as

$$M_{\mu\nu} = \frac{4\pi^2\hbar^2}{m}\int d\mathbf{q}\; a_{\mathbf{q}} b_{\mathbf{q}}^* e^{-\sqrt{\kappa^2+\mathbf{q}^2}z_t} e^{i\mathbf{q}\cdot\mathbf{x}_t} \;=\; A\,\psi_{s,\nu}(\mathbf{r}_t) \;, \tag{2.12}$$

where $\mathbf{r}_t = (\mathbf{x}_t, z_t)$ is the center position of the wavefunction on the tip. This shows that the matrix element is proportional to the sample wavefunction at the center of the tip.

This approximation of the matrix element leads to the useful result that the STM differential conductance is proportional to the sample local density of states, a principle that underlies the interpretation of most scanning tunneling spectroscopy. In the low-temperature regime where $\partial f(\mathcal{E}-|e|V)/\partial V \approx |e|\delta(\mathcal{E}-|e|V-\mathcal{E}_F)$ the differential conductance dI/dV can be expressed as

$$\begin{aligned}\frac{dI}{dV}(\mathbf{r}_t,V) &= \frac{2\pi|e|^2}{\hbar}\rho_t A^2\int_{\mathcal{E}_F}^{\mathcal{E}_F+|e|V}\sum_{\nu}\left|\psi_{s,\nu}(\mathbf{r}_t)\right|^2\rho_{s,\nu}(\mathcal{E})\delta(\mathcal{E}-|e|V-\mathcal{E}_F)d\mathcal{E} \\ &= \frac{2\pi|e|^2}{\hbar}\rho_t A^2\int_{\mathcal{E}_F}^{\mathcal{E}_F+|e|V}\sum_{\nu}\left|\psi_{s,\nu}(\mathbf{r}_t)\right|^2\rho_{s,\nu}(\mathcal{E}_F+|e|V)d\mathcal{E}\,.\end{aligned} \tag{2.13}$$

Since $\rho_{s,\nu}$ is defined as the density of states of a single state $\psi_{s,\nu}$ with the matrix element $\langle\psi_{s,\nu}|H'|\psi_t\rangle$, then $\rho_{s,\nu}(\mathcal{E})=\delta(\mathcal{E}-\mathcal{E}_\nu)$, so that

$$\begin{aligned}\frac{dI}{dV}(\mathbf{r}_t,V) &\propto \sum_{\nu}\left|\psi_{s,\nu}(\mathbf{r}_t)\right|^2\delta(\mathcal{E}_F+|e|V-\mathcal{E}_\nu) \\ &= e^{-2\kappa z_t}\sum_{\nu}\left|\psi_{s,\nu}(\mathbf{x}_t,z_t=0)\right|^2\delta(\mathcal{E}_F+|e|V-\mathcal{E}_\nu) \\ &= LDOS(\mathbf{r}_t,\mathcal{E}_F+|e|V)\,.\end{aligned} \tag{2.14}$$

The differential conductance thus reflects the local density of states at the point of the tip. Since sample wavefunctions decay exponentially through the vacuum, the tunneling current is very sensitive to changes in the tip-sample distance. By keeping the tunneling current constant through a feedback loop, one can map out the topography of a sample. In the following section the different scanning modes used to map out surface topography and spectroscopy will be introduced.

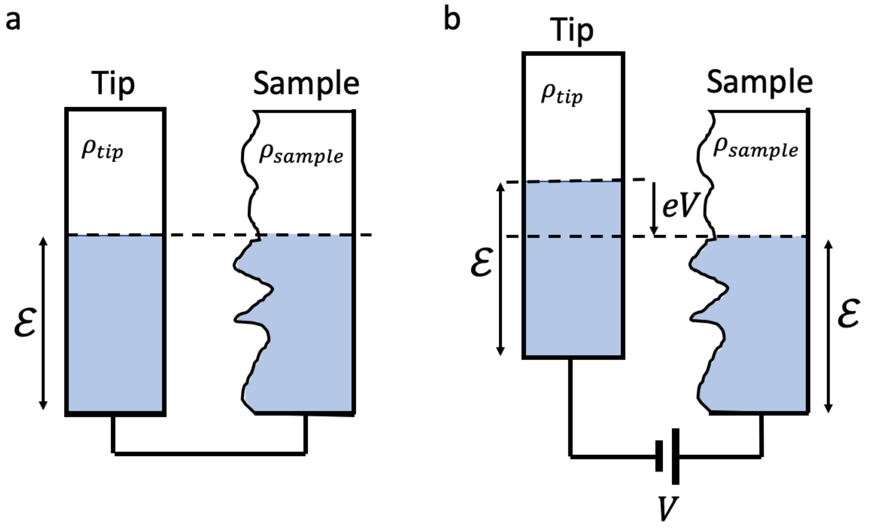

Fig. 2.1: Tip and sample Fermi levels under an external bias. (a) Without an external bias, the Fermi level of the tip and sample are assumed to be the same (b) With an applied bias V to the sample, the density of states of the tip is shifted up by $|e|V$.

2.2 Scanning Tunneling Microscope Operation

A STM maps the surface topography of a sample by using a feedback loop to control the tip-sample separation as the tip is scanned across the surface of the sample. Fig. 2.2 shows the basic setup of a STM operating in constant-current mode. When the z-feedback loop is engaged, the tip-sample separation is changed such that the tunneling current setpoint is maintained. Tunneling currents typically range from 10^{-12} to 10^{-9} A, so a high-gain current amplifier is used to amplify the signal. The current amplifier outputs a measurable voltage in the $-10\text{V} < V_{out} < 10\text{V}$ range, which is read and controlled by a real-time computer in a PID loop. The output voltage of the z-feedback controller is then applied to the z-piezo to maintain constant tunneling current. Control voltages applied to the x- and y-piezos deform the scan tube such that the tip can be scanned across the x-y plane. As the z-piezo responds to changes in the topography of the sample, the control voltage is recorded to obtain a topographic map of the sample. Typically, the voltage bias between the sample and tip is applied onto the sample (although certain configurations can be used to bias the tip by applying a voltage on the non-inverting input of the current amplifier). In STM convention this bias is always thought of as a voltage applied to the sample, even if the negative bias is applied to the tip. If the applied bias is sufficiently small, the tunneling current $I(\mathbf{r}_t, V_S) \sim dI(\mathbf{r}_t, V_S)/dV_S \propto LDOS(\mathbf{r}_t, \mathcal{E}_F + |e|V_S)$ is proportional to the local density of states at $\mathcal{E}_F$, thus a low-bias topograph shows the spatial distribution of electron probability density from orbitals near $\mathcal{E}_F$.

A STM can also be operated in constant-height mode when the sample has a relatively homogeneous local density of states. In constant-height mode the feedback loop is disengaged so that changes in the tunneling current can be interpreted directly as changes in sample topography.

dI/dV spectroscopy is performed by applying a wiggle voltage V_{AC} at a reference frequency onto the sample while detecting the AC current through a lock-in amplifier. The lock-in amplifier picks out the AC component of the tunneling current signal at the reference frequency, which is proportional to $LDOS(\mathbf{r}_t, \mathcal{E}_F + |e|V_S)$. One typically obtains a dI/dV spectrum by keeping the tip at a constant position while sweeping the sample bias. By scanning the tip across the surface while in feedback and monitoring the dI/dV signal, one can obtain a map of the local density of states at a given energy $\mathcal{E}_F + |e|V_S$. Such an image is called a dI/dV map, and reveals the spatial distribution of the surface electron wavefunction at a given energy.

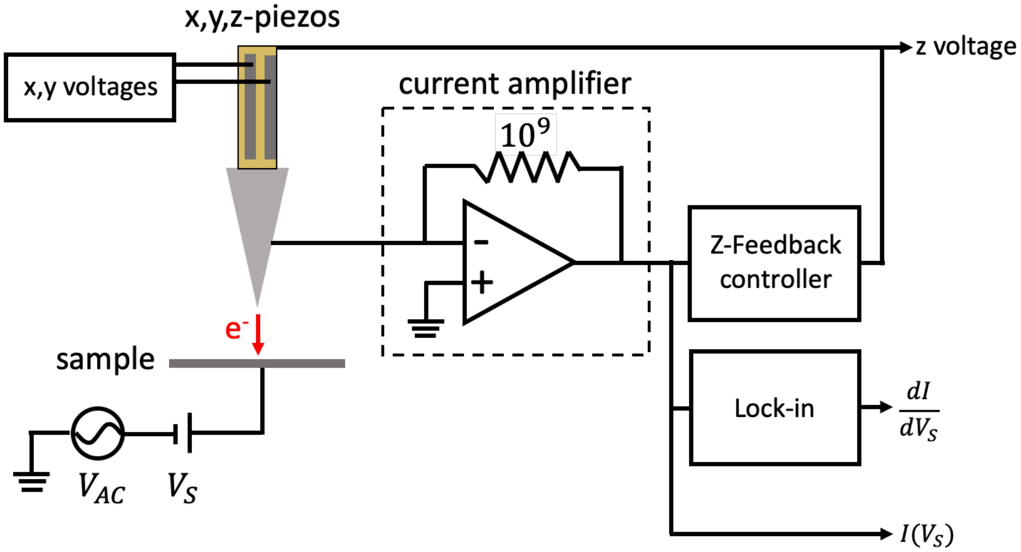

Fig. 2.2: Basic setup of a STM. A STM detects tunneling current through a high-gain current amplifier. In constant current scanning mode the detected current is fed into a feedback controller which outputs a control voltage to the z-piezo to control the tip-sample separation in order to keep the tunneling current constant. An AC wiggle voltage can be applied to the sample to perform dI/dV spectroscopy and dI/dV mapping.

2.3 Scanning Tunneling Potentiometry

Scanning tunneling potentiometry (STP) takes advantage of the high spatial resolution of STM to create detailed electrochemical potential maps of a conductor under current flow. Within a conductor of finite resistance an electrochemical potential gradient develops between source and drain electrodes when an external bias is applied. When a STM tip is placed into the tunneling regime at some point between the source and drain contact, a DC tunneling current will flow between the tip and sample if the electrochemical potential is not equal on both sides. The operating principle of STP is to apply a bias on the tip such that the measured DC current is nulled to zero. The bias needed to make the DC current zero is then equal to the potential at the location of the tip. A feedback loop can be employed to adjust the bias applied to the tip such that the DC current is always kept at zero. A diagram of such a setup is shown in Fig. 2.3. A second feedback loop is needed to keep the tip-sample separation constant. The topography feedback signal used in lieu of a DC current (since the DC current is nulled out) is a small AC wiggle voltage applied between the tip and sample which causes an AC tunneling current. The AC component of the tunneling current is picked up by a lock-in amplifier and used to drive the z-feedback. By keeping the AC tunneling current constant one can perform STM topography in much the same way as STM using DC tunneling current.

STP has been used to map out the potential drop created by residual resistivity dipoles (RRDs) in metal films,[22,24] and, more recently, at the interface of mono- and bi-layer graphene.[21] STP can also be used to obtain the in-plane electric field gradient, a quantity of interest in electromigration processes. This is used in chapter 8 to determine the magnitude and direction of the average in-plane electric field, which allows us to extract the effective charge of migrating molecular adsorbates.

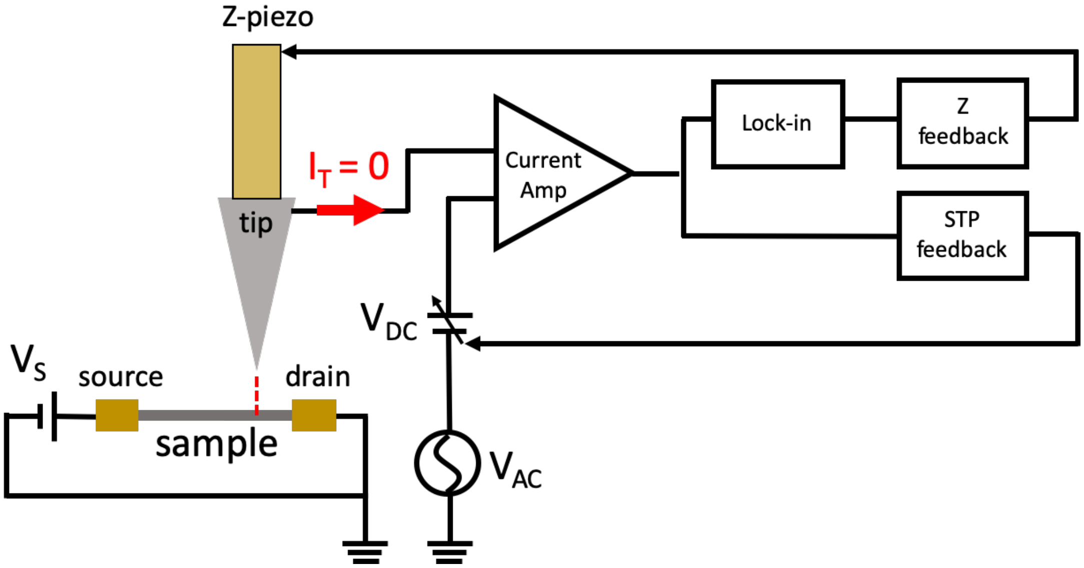

Fig. 2.3: Scanning tunneling potentiometry setup. A STP setup detects the electrochemical potential at the point of measurement by applying an offset voltage to the tip such that the DC current is zero. An AC wiggle voltage creates an AC tunneling current for topography feedback, replacing the DC current in normal STM.

3 Theoretical Background for Molecule-decorated Graphene Devices

The purpose of this chapter is to introduce the necessary theoretical background to understand how electrons and surface adsorbates behave on a graphene field-effect transistor, as well as theoretical concepts and notation frequently used in this field to describe electronic and molecular behavior.

3.1 Graphene as a Gate-tunable Substrate

Graphene, first successfully isolated by Novoselov and Geim in 2004,[47] is a single-atom-thick layer of sp^2-bonded carbon which offers a unique conductive substrate for studying molecular adsorbates due to its special electronic properties. Some of the key features of graphene include its extraordinarily high carrier mobility due to its low concentration of defects, suppressed scattering due to its symmetry-protected Dirac quasiparticles, its ability to sustain high current densities without deterioration, its integrability with other van der Waals layered materials,[39] and (most importantly for this dissertation) the tunability of its charge density through electrostatic gating. By laying graphene flat on an insulating substrate with an electrostatic gate below via a sandwich of hBN/SiO$_2$/Si, electrons can be easily added to the graphene to change its Fermi level. The low density of states of graphene at the Fermi energy allows the Fermi level to be tuned over a range of ± 0.25 eV.

In this section I will introduce the fundamental electronic structure of graphene, which gives rise to a vanishing density of states at charge neutrality. I will then explain the architecture of a typical graphene field effect transistor, as well as how gating affects the Fermi level of graphene.

3.1.1 Electronic Properties of Graphene

The crystal structure of graphene is shown in Fig. 3.1 (a). Graphene has two atoms per unit cell (labeled A and B in Fig.1.1 (a)) with lattice vectors

$$\mathbf{a}_1 = \frac{a}{2}\left(3, \sqrt{3}\right), \qquad \mathbf{a}_2 = \frac{a}{2}\left(3, -\sqrt{3}\right), \tag{3.1}$$

where a is the C-C distance of ≈ 1.42Å. The atoms of the A and B sublattices are arranged in a honeycomb lattice such that each atom in the A sublattice has 3 nearest neighbors in the B sublattice, and each atom in the B sublattice has 3 nearest neighbors in the A sublattice. Of the four valence electrons in carbon's s-p shell, three of them form σ bonds by coupling the sp^2 hybrid orbitals together, leading to the strong backbone of the honeycomb structure. The remaining electron resides in the p$_z$ orbital, which, by overlapping with neighboring p$_z$ orbitals, forms the π and π^* bands. Carrier transport is primarily conducted through the π bands in graphene. The Brillouin zone structure of graphene is a hexagon. The reciprocal lattice vectors are

$$\mathbf{b}_1 = \frac{2\pi}{3a}\left(1, \sqrt{3}\right), \qquad \mathbf{b}_2 = \frac{2\pi}{3a}\left(1, -\sqrt{3}\right). \tag{3.2}$$

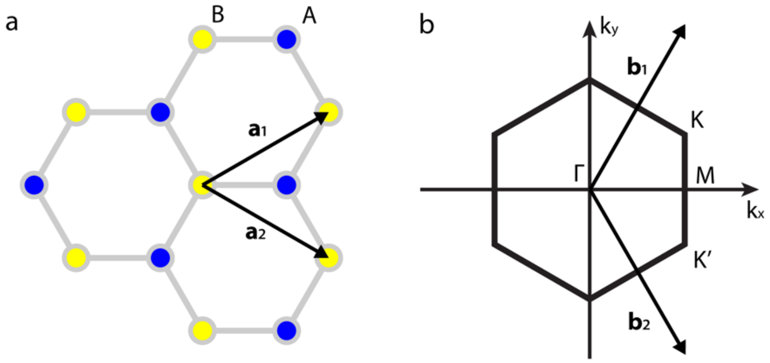

Fig. 3.1: Real and reciprocal space structure of graphene. (a) Atomic structure of graphene. Graphene consists of two sublattices A and B arranged in a honeycomb structure. $\mathbf{a}_1$ and $\mathbf{a}_2$ are the two lattice vectors. (b) Brillouin zone of graphene with the high symmetry points K, K', M and Γ. $\mathbf{b}_1$ and $\mathbf{b}_2$ are the two reciprocal lattice vectors.

Two inequivalent corners of the Brillouin zone are located at

$$\mathbf{K} = \left(\frac{2\pi}{3a}, \frac{2\pi}{3\sqrt{3}a}\right), \qquad \mathbf{K}' = \left(\frac{2\pi}{3a}, -\frac{2\pi}{3\sqrt{3}a}\right). \tag{3.3}$$

These two high symmetry points are important for the electronic structure of graphene because they are the momentum-space locations of the Dirac point.

The band structure of graphene can be understood with a simple tight-binding model. The tight-binding Hamiltonian for electrons in graphene, considering only nearest-neighbor hopping, can be expressed as

$$H = -t \sum_{\langle i,j\rangle,\sigma} a_{\sigma,i}^{\dagger}\, b_{\sigma,j} + H.c.\ , \tag{3.4}$$

where $a_{\sigma,i}$ ($a_{\sigma,i}^{\dagger}$) annihilates (creates) an electron with spin σ on site $\mathbf{R}_i$ of sublattice A, and $b_{\sigma,i}$ ($b_{\sigma,i}^{\dagger}$) annihilates (creates) an electron with spin σ on site $\mathbf{R}_i$ of sublattice B. $t \approx 2.7$eV is the hopping integral between nearest-neighbor orbitals in different sublattices. The vectors δ connecting the A atoms to their nearest neighbors are

$$\boldsymbol{\delta}_1 = \frac{a}{2}\left(1, \sqrt{3}\right), \quad \boldsymbol{\delta}_2 = \frac{a}{2}\left(1, -\sqrt{3}\right), \quad \boldsymbol{\delta}_3 = a(-1,0), \tag{3.5}$$

thus Fourier transforming to momentum space and writing $\mathbf{R}_j = \mathbf{R}_i + \boldsymbol{\delta}$, we obtain

$$\begin{aligned} H &= -t \sum_{\langle i,j\rangle,\sigma} a_\sigma^\dagger(\mathbf{R}_i)\, b_\sigma(\mathbf{R}_j) + H.c. \\ &= -t \sum_{i,\boldsymbol{\delta},\sigma} a_\sigma^\dagger(\mathbf{R}_i)\, b_\sigma(\mathbf{R}_i + \boldsymbol{\delta}) + H.c. \\ &= \ -\frac{t}{N} \sum_{i,\boldsymbol{\delta},\sigma} \sum_{\mathbf{q},\mathbf{q}'} e^{i\mathbf{q}'\cdot\boldsymbol{\delta}}\, e^{i\mathbf{R}_i\cdot(\mathbf{q}'-\mathbf{q})} a_\sigma^\dagger(\mathbf{q})\, b_\sigma(\mathbf{q}') + H.c. \\ &= \ -t \sum_{\boldsymbol{q},\boldsymbol{\delta},\sigma} e^{i\boldsymbol{q}\cdot\boldsymbol{\delta}} a_\sigma^\dagger(\mathbf{q})\, b_\sigma(\mathbf{q}) + H.c. \end{aligned} \tag{3.6}$$

If we define $\psi_\sigma(\mathbf{q}) = \big(a_\sigma(\mathbf{q}), b_\sigma(\mathbf{q})\big)^T$, then H can be rewritten as

$$H = -t \sum_{\boldsymbol{k},\sigma} \psi_\sigma^\dagger(\mathbf{q}) \begin{pmatrix} 0 & f(\mathbf{q}) \\ f^*(\mathbf{q}) & 0 \end{pmatrix} \psi_\sigma(\mathbf{q}) \quad , \tag{3.7}$$

where $f(\mathbf{q}) = e^{-iq_x a} + 2e^{\frac{iq_x a}{2}} \cos\left(\frac{\sqrt{3}\, q_y a}{2}\right)$. Diagonalizing the Hamiltonian, we find the eignevalues

$$E(\mathbf{q}) = \pm t|f(\mathbf{q})| = \pm t \sqrt{3 + 2\cos\big(\sqrt{3} q_y a\big) + 4\cos\left(\frac{\sqrt{3}}{2} q_y a\right) \cos\left(\frac{3}{2} q_x a\right)} \tag{3.8}$$

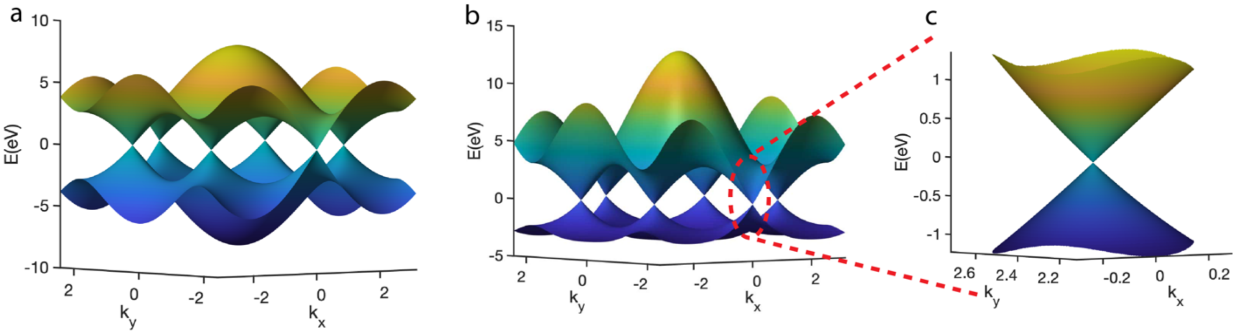

Fig. 3.2: $\boldsymbol{\pi}$-band structure of graphene. (a) The band structure of graphene with $t \approx 2.7$eV (b) The band structure of graphene including second nearest-neighbor hopping, with $t \approx 2.7$eV and $t' \approx -0.2t$. (c) Zoom-in of the graphene band structure near the Dirac point, showing the characteristic linear dispersion.

The resulting band structure is shown in Fig. 3.2 (a). Notably, the upper and lower bands touch at the points **K** and **K**$'$, which lie at zero energy and are known as the Dirac points. Since graphene has one accessible electron per carbon atom, the lower band (π) is fully filled while the upper band (π^*) remains empty. This leads to the result that graphene is a semimetal, with conduction and valence bands touching at the Dirac points $\mathbf{K}$ and $\mathbf{K}'$. Near these special points $f(\mathbf{q})$ can be expanded to first order. Expanding around the $\mathbf{K}$ point, for instance, we define $\mathbf{q} = \mathbf{K} + \mathbf{k}$, where $|\mathbf{k}| \ll |\mathbf{K}|$, and $f(\mathbf{k})$ can be rewritten as

$$f(\mathbf{k}) = \frac{-3a}{2} e^{-i\frac{2\pi}{3}} \left(k_x - ik_y\right), \tag{3.9}$$

dropping the phase factor $e^{-i\frac{2\pi}{3}}$ (since it does not affect the energies), the Hamiltonian becomes

$$H_{\mathbf{K}} = \frac{3at}{2} \begin{pmatrix} 0 & k_x - ik_y \\ k_x + ik_y & 0 \end{pmatrix} . \tag{3.10}$$

Defining the Fermi velocity as $v_F = \frac{3at}{2\hbar}$ and using the Pauli matrices

$$\sigma_x = \begin{pmatrix} 0 & 1 \\ 1 & 0 \end{pmatrix}, \sigma_y = \begin{pmatrix} 0 & -i \\ i & 0 \end{pmatrix}, \tag{3.11}$$

the Hamiltonian can be conveniently expressed as

$$H_{\mathbf{K}} = \hbar v_F (k_x \sigma_x + k_y \sigma_y) = \hbar v_F \mathbf{k} \cdot \boldsymbol{\sigma} . \tag{3.12}$$

Similarly, expanding the Hamiltonian near the $\boldsymbol{K}$ point leads to the result

$$H_{\mathbf{K}'} = \hbar v_F (k_x \sigma_x - k_y \sigma_y) = \hbar v_F\, \mathbf{k} \cdot \boldsymbol{\sigma}^* . \tag{3.13}$$

The $\mathbf{K}$ and $\mathbf{K}'$ valley labels are called the valley isospin, and the equations governing electrons in the two valleys are related to each other by time-reversal symmetry. The form of the Hamiltonian represents a massless Dirac equation in two-dimensions. The eigenenergies of this Hamiltonian are thus

$$\mathcal{E}_{\pm}(\mathbf{k}) = \pm \hbar v_F |\mathbf{k}| , \tag{3.14}$$

and the bands disperse linearly near the Dirac point, as shown in Fig. 1.2(c). The eigenvectors near the $\mathbf{K}'$ point are

$$\psi_{\mathbf{K}',\pm} = \frac{1}{\sqrt{2}} \left(e^{\frac{i\theta_k}{2}}, \pm e^{-\frac{i\theta_k}{2}} \right)^T , \tag{3.15}$$

and near the $\mathbf{K}$ point,

$$\psi_{\mathbf{K},\pm} = \frac{1}{\sqrt{2}} \left(e^{-\frac{i\theta_k}{2}}, \pm e^{\frac{i\theta_k}{2}} \right)^T , \tag{3.16}$$

where $\theta_k = \arctan(k_x/k_y)$ and the $\pm$ signs correspond to the sign of the eigenenergies. These eigenvectors correspond to symmetric and antisymmetric electron wavefunctions on the A and B sublattices, and can be interpreted as spinors. Conservation of this pseudospin (unrelated to the real spin of the electrons) in graphene leads to interesting properties, including suppression of current backscattering in the absence of intervalley scattering.[48]

Inclusion of second-nearest neighbor hopping on the same sublattice does not fundamentally change the electronic properties of graphene near the Dirac point. The Hamiltonian including second-nearest neighbor hopping is

$$H = -t \sum_{\langle i,j\rangle,\sigma} (a_{\sigma,i}^{\dagger} b_{\sigma,j} + H.c.) - t' \sum_{\langle\langle i,j\rangle\rangle,\sigma} (a_{\sigma,i}^{\dagger} a_{\sigma,j} + b_{\sigma,i}^{\dagger} b_{\sigma,j} + H.c.), \tag{3.17}$$

and its eigenenergies are

$$\mathcal{E}(\mathbf{k}) = \pm t|f(\mathbf{k})| - t'\sqrt{f^2(\mathbf{k}) - 3} \tag{3.18}$$

This dispersion relation is plotted in Fig. 3.2 (b). An asymmetry between π and π^* can now be seen as a result of second-nearest neighbor hopping.

The density of states (DOS) of graphene near the Dirac point can be derived from the dispersion relation $\mathcal{E}_{\pm}(\mathbf{k}) = \pm\hbar v_F|\mathbf{k}|$. The DOS for graphene, accounting for spin and valley degeneracies, can be written as

$$DOS(\mathcal{E}) = \frac{1}{L^2}\frac{\partial N}{\partial \mathcal{E}} = \frac{\partial}{\partial \mathcal{E}}\frac{4\pi k^2}{(2\pi)^2}. \tag{3.19}$$

Substituting the expression for k in Eq. (3.14), we obtain the result that the DOS is proportional to the energy $\mathcal{E}$ near the Dirac point.

$$DOS(\mathcal{E}) = \frac{2|\mathcal{E}|}{\pi\hbar^2 v_F^2} \tag{3.20}$$

This leads to vanishing DOS and quantum capacitance near the Dirac point. This property is fundamental to the sensitivity of the Fermi level in graphene to electrostatic gating or chemical charge transfer doping, two important elements of a molecule-decorated graphene field-effect device.

To obtain the full DOS away from the Dirac point, we can numerically integrate the tight-binding band structure in the first Brillouin zone to obtain Fig. 3.3. It can be seen that near the Dirac point, the DOS varies linearly with energy. At higher energies, two peaks in the DOS known as van Hove singularities are seen. The effect of second-nearest neighbor hopping produces a noticeable electron-hole asymmetry in the DOS.

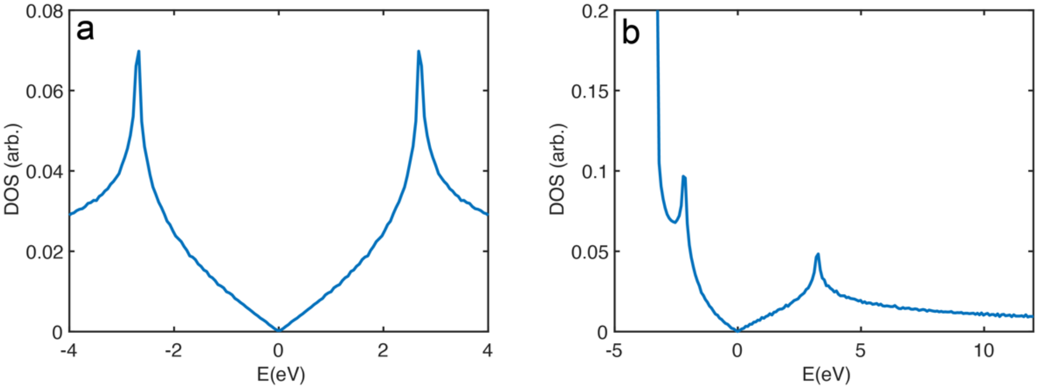

Fig. 3.3: Density of state of graphene. (a) Numerically calculated density of state of graphene using nearest-neighbor hopping integral $t \approx 2.7\text{eV}$. (b) Numerically calculated density of state of graphene using $t \approx 2.7\text{eV}$ and second nearest-neighbor hopping integral $t' \approx -0.2t$. The DOS is skewed with higher weight in the lower band (π).

3.1.2 Graphene Field-effect Devices

In order to study the response of graphene to electric fields and chemical dopants, it is useful to incorporate graphene into a field-effect transistor geometry. A schematic of such a device is shown in Fig. 3.4, where the graphene is stacked on top of hexagonal boron nitride, a 2D insulator, which is transferred on top of a SiO_2 coated Si wafer. Source-drain current parallel to the graphene surface as well as STM tunneling currents can be conducted through metal source/drain contacts deposited on the graphene. A gate voltage can be applied to the doped Si substrate to change the Fermi level of the graphene through electrostatic gating.

When a gate voltage is applied to the graphene device, the Si layer and the graphene act as the two plates of a capacitor, each hosting equal and opposite charges. The total charge density n (expressed in units of one electron charge) on the graphene side of the parallel plate capacitor is

$$n = C(V_G - V_0) = \int_{\mathcal{E}_D}^{\mathcal{E}_F} DOS(\mathcal{E} - \mathcal{E}_D) d\mathcal{E} = \frac{|\mathcal{E}_F - \mathcal{E}_D|^2}{\pi \hbar^2 v_F^2}\,, \qquad (3.21)$$

where $\mathcal{E}_F$ is the Fermi level, $\mathcal{E}_D$ is the Dirac point energy, C is the unit area capacitance and V_0 accounts for any gate voltage offset induced by chemical doping. A typical value of C for our graphene transistors is $5 \times 10^{10}\ e^- V^{-1} cm^{-2}$. A typical value of the Fermi velocity v_F is $1.1 \times 10^6\ m\ s^{-1}$. The Fermi level and applied gate voltage are thus simply related by

$$\mathcal{E}_F - \mathcal{E}_D = sign(V_G - V_0)\ \hbar v_F \sqrt{\pi C |V_G - V_0|}\,, \qquad (3.22)$$

enabling the Fermi level (and by extension the carrier density) to be easily controlled by the applied gate voltage.

In the Drude model the carrier density n is proportional to the conductivity σ by $\sigma = ne\mu$, and so we expect the conductivity of graphene to be smaller at the Dirac point energy. This means a two-terminal gated graphene device can act like a transistor, since its conductivity is gate-tunable. In reality, graphene is far from a Drude metal, since electrons in graphene devices scatter in a more complex way, and so the conductivity of graphene is never zero at charge neutrality. To describe the full picture of electron transport through graphene, one must analyze the mobility μ, and so the scattering time τ is needed. This will be further discussed in section 3.3.

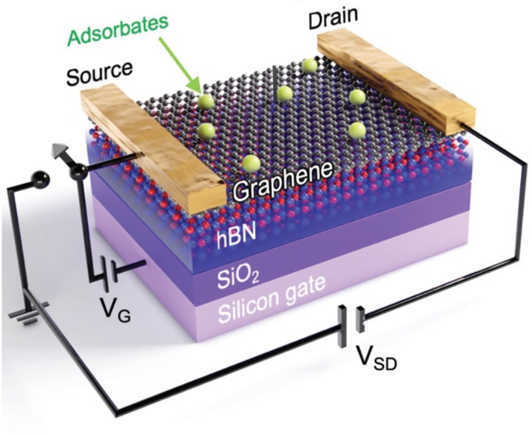

Fig. 3.4: A graphene/hBN field-effect transistor. A sheet of graphene is laid on top of dielectric layers of hBN and SiO_2. A gate voltage can be applied to the silicon substrate to electrostatically gate the graphene. Source and drain contacts are used to drive current through the device. Adsorbates can be deposited on the graphene and then controlled by the gate voltage and source-drain current.

3.2 Adsorbates on Graphene

When adsorbates are placed on the surface of a conducting substrate the previously localized electronic wavefunction of the adsorbate bleeds into the conductor, hybridizing with the conducting continuum states. Depending on the strength of hybridization, molecules can become weakly or strongly coupled to the substrate, resulting in either physisorption or chemisorption. In graphene chemisorbed adsorbates that break the sublattice symmetry (such as atomic hydrogen) change the symmetry of bonding orbitals in graphene and lead to zero modes localized near the defect site.[41,49] On the other hand, physisorbed adsorbates mainly act as donor/acceptor levels that can host extra charge, such as K and NO_2.[50,51] These adsorbates induce chemical doping on graphene by changing the graphene Fermi level through charge transfer, but are otherwise chemically inert, and are easily removed from the surface by heating. In the case of F_4TCNQ molecules, the lowest unoccupied molecular orbital (LUMO) is so close in energy to the graphene Dirac point that they accept the electrons in graphene until either all the molecules become negatively charged with an electron or the Fermi level becomes pinned to the LUMO level (whichever comes first).

3.2.1 Fermi Level Pinning

One type of Fermi level pinning occurs when a material with a high density of states at its Fermi level, such as a metal, is brought into contact with a material with low density of states and a different Fermi level. When the two materials come into contact, electrons are transferred from one material to the other until the Fermi level is equal in both materials. Since the Fermi level of the material with high density of states is not easily shifted, the Fermi level of the low density of states material changes to match that of the high density of states material.

To quantify the tendency of the Fermi level $\mathcal{E}_F$ of a material to shift with charge transfer, it is useful to define the quantum capacitance C_q which can be written as

$$C_q = \frac{dQ}{dV_q} = e^2 \frac{dn}{d\mu} , \tag{3.23}$$

where the induced charge is $dQ = -|e|dn$ (n is number of electrons introduced, $|e|$ is the magnitude of the electron charge), and the change in the chemical potential is $-\frac{d\mu}{|e|} = dV_q$. In a material with high quantum capacitance, more charge is needed to shift the Fermi level.

Fig. 3.5 shows a schematic of the relevant energies when a material with low density of states is brought into contact with a reservoir with high density of states (such as a metal). Initially, the reservoir and the low density of state material have different work functions, Φ_1 and Φ_2, which represent the energy needed to move an electron at the Fermi level of the materials to the vacuum level. The reservoir and the material share the same vacuum level because there is no electric field between them. However, when they are brought into contact, charge ΔQ is transferred between reservoir and material so that the electrochemical potential of electrons (*i.e.* the Fermi level) becomes equal on both sides. The charge transfer shown in Fig. 3.5 has two effects: 1) it raises the chemical potential of electrons and 2) because electrons are charged, it raises the electric potential of the material, as indicated by the material's raised vacuum level. The first effect generates a change in the chemical potential $\delta\mu_q = -\frac{\delta Q}{|e|C_q}$, and the second effect generates another change in the chemical potential that can be attributed to the electric field $\delta\mu_{geo} = -\frac{\delta Q}{|e|C_{geo}}$ which also raises the vacuum level of the material. Here C_{geo} is the geometric capacitance between the two materials. The total change in Fermi level is thus

$$\delta E_F = \delta\mu_q + \delta\mu_{geo} = -\frac{1}{|e|}\left(\frac{1}{C_q} + \frac{1}{C_{geo}}\right)\delta Q = -\frac{1}{|e|}\frac{\delta Q}{C} , \tag{3.24}$$

where we have defined C as the total effective capacitance, equal to the sum of the geometric and quantum capacitance in series. In the case of graphene field effect devices where the parallel plates are separated by hundreds of nanometers, typically $C_{geo} \ll C_q$, so $C_{geo} \approx C$, and the contribution from C_q can be ignored. This is why only the geometric capacitance needs to be considered when calculating gate-induced charge density in typical solid-state graphene field effect devices. On the other hand, in cases where the gate is extremely close to the graphene, such as in electrochemical cells where a Helmholtz layer of ions directly contacts the graphene, $C_{geo} \gg C_q$, so $C_q \approx C$, and the contribution from C_{geo} can be ignored. In these types of devices, the quantum capacitance of graphene can be directly measured.[52] In this case charge is transferred between the reservoir and the material without significantly raising the electric potential because of the large geometric capacitance, but the charge transfer does shift the chemical potential of the electrons in the graphene.

Typically Fermi level pinning is thought of as a process where a metal contact shifts the electrochemical potential of an adsorbate system. However, in Chapter 4 and 5 we present a “tail-wags-dog” system where the adsorbate density is so high that it shifts the Fermi level of the graphene and pins it to a molecular level. This phenomenon underlies the behavior of the tunable-density adsorbate system that we have discovered when adsorbates are placed on graphene.

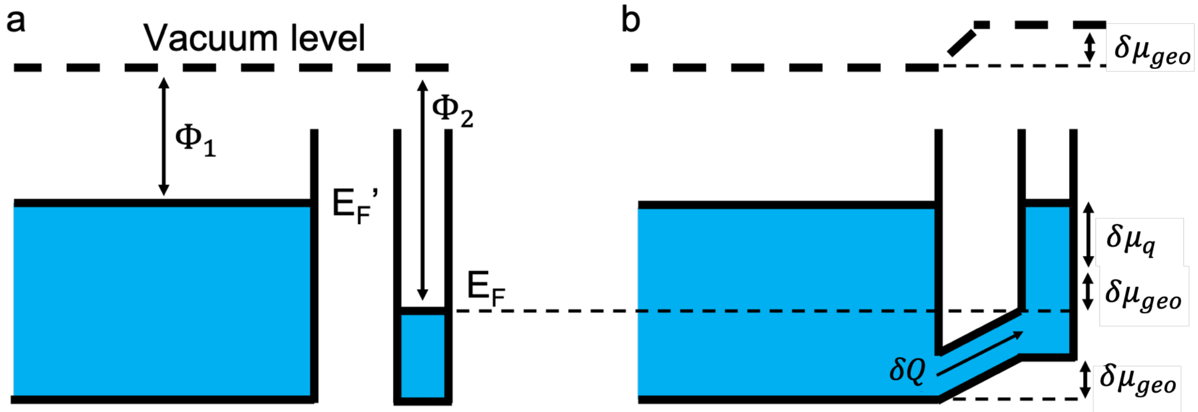

Fig. 3.5: Fermi level pinning mechanism. (a) Two materials with different work functions are initially spatially separated and share a vacuum level. The left material acts as a reservoir of charge, with a significantly higher quantum capacitance than the right material. (b) The two materials are brought into contact, which causes the electrochemical potential to equilibrate on both sides. Charge transfer causes the electric potential and chemical potential to rise for the right material. The rise in the electric versus chemical component of the electrochemical potential depends on the ratio of the geometric versus quantum capacitance.

3.2.2 Green’s Functions, LDOS, PDOS, and Hybridization

Some important quantities for characterizing the spatial extent and hybridization of electronic states for graphene and adsorbates are the local density of states (LDOS) and the projected density of states (PDOS). In STM dI/dV measurements are proportional to LDOS, as shown previously in chapter 2. LDOS can be measured as a function of the bias voltage between tip and sample by monitoring the dI/dV signal as the bias voltage is swept, a technique called scanning tunneling spectroscopy (STS). Maps of LDOS on the surface can be produced by recording the dI/dV signal while scanning the tip at a fixed bias voltage. The LDOS of a system with Hamiltonian H and eigenstates $|n\rangle$ and eigenenergies $\mathcal{E}_n$ is formally defined as

$$\mathrm{LDOS}(\mathbf{r},\mathcal{E}) = \sum_n |\langle \mathbf{r}|n\rangle|^2 \;\delta(\mathcal{E}-\mathcal{E}_n)\,, \tag{3.25}$$

where projection of state $|n\rangle$ onto a position basis $|\mathbf{r}\rangle$ is the wavefunction $\psi_n(\mathbf{r})$, and the Dirac delta function picks out the probability density of the wavefunctions at energy $\mathcal{E}$.

PDOS is closely related to LDOS, but instead of projecting onto the position basis $|\mathbf{r}\rangle$, another basis state $|\phi\rangle$ is used.

$$\mathrm{PDOS}(|\phi\rangle, \mathcal{E}) = \sum_{n} |\langle\phi|n\rangle|^2 \ \delta(\mathcal{E} - \mathcal{E}_n)\,, \tag{3.26}$$

The state $|\phi\rangle$ can be chosen to be an unperturbed eigenstate of an impurity atom, before hybridization with the substrate orbitals. $\mathrm{PDOS}(|\phi\rangle, \mathcal{E})$ then represents the amount of the system's wavefunction probability density that lies in the state $|\phi\rangle$ at energy $\mathcal{E}$.

The total density of states (DOS) can be defined as the LDOS integrated over all space,

$$\mathrm{DOS}(\mathcal{E}) = \int \mathrm{LDOS}(\mathbf{r}, \mathcal{E}) \ d\mathbf{r}\,, \tag{3.27}$$

A powerful way of modeling the electronic properties of adsorbates on a surface is through Green's function methods, which can be used to describe hybridization of adsorbate orbitals with the substrate. This is also used throughout chapters 7 and 8 to calculate scattering and electromigration behavior of adsorbates on graphene.

A Green's function is the solution to the linear differential equation

$$\mathrm{D}\, G(x,s) = \delta(x - s)\,, \tag{3.28}$$

where D is a linear differential operator, and $G(x,s)$ can be thought of as the response of the system evolving under D for an impulse at $x = s$. Green's functions are useful for solving inhomogeneous linear differential equations such as D $u(x) = f(x)$ because the source term $f(x)$ can be decomposed into a linear combination of Dirac delta functions $\delta(x - s)$, enabling the solution $u(x)$ to be written as a linear combination of Green's functions $G(x,s)$, specifically

$$u(x) = \int G(x,s) f(s) ds. \tag{3.29}$$

However, the Green's function for a system may not be unique, since adding the homogeneous solution $v(x)$ (where D $v(x) = 0$) to a Green's function also satisfies the original linear differential equation. In some cases, it is possible to find a Green's function that is non-vanishing for only $x \geq s$, which is called a retarded Green's function, and another Green's function that is non-vanishing for only $x \leq s$, which is called an advanced Green's function. In scattering theory, the retarded Green's function represents outgoing waves after scattering with a scatterer while the advanced Green's function represents incoming waves before scattering.

We can recast the formalism of Green's functions in terms of quantum states and operators for the Schrödinger equation $\hat{H}|\psi\rangle = i\hbar\frac{\partial}{\partial t}|\psi\rangle$. For the time-independent Hamiltonian H, we define the differential operator

$$\hat{D}_S(t) = i\hbar\frac{\partial}{\partial t} - \hat{H}. \tag{3.30}$$

Let us now define the Green's operator $\hat{G}(t)$ which satisfies

$$\hat{D}_S(t)\hat{G}(t) = \delta(t)\,. \tag{3.31}$$

We notice that the time evolution operator $\hat{U}(t) = e^{-i\hat{H}t/\hbar}$ satisfies the homogeneous equation $\hat{D}_S(t)\hat{U}(t) = 0$. To solve the inhomogeneous equation, we need a function which produces the Dirac delta function upon differentiation, which would be a Heaviside function $\theta(t)$, thus we can manufacture the Green's operator

$$\hat{G}^R(t) = \frac{1}{i\hbar}\theta(t)e^{-i\hat{H}t/\hbar} \quad where \quad \theta(t) = \begin{cases} 1\,, & t > 0 \\ 0\,, & t \le 0 \end{cases}\,. \tag{3.32}$$

We can then check that $\hat{D}_S(t)\hat{G}^R(t) = \hat{U}(t)\delta(t) = \hat{U}(0)\delta(t) = \delta(t)$, satisfying the inhomogeneous equation. $\hat{G}^R(t)$ defined this way is a *retarded Green's operator*. The Green's operator describes how the system evolves with time. However, this is not the only choice of function which satisfies (3.31). Another option is called the *advanced Green's operator*, where

$$\hat{G}^A(t) = \frac{1}{-i\hbar}\theta(-t)e^{-i\hat{H}t/\hbar} \quad where \quad \theta(-t) = \begin{cases} 0\,, & t > 0 \\ 1\,, & t \le 0 \end{cases}\,. \tag{3.33}$$

The Green's operator describes how the system evolves with time. We are also interested in information about the energy of the system, which can be obtained by recasting the Green's operator into the energy domain through a Fourier transform. The retarded Green's operator as a function of energy is

$$\hat{G}^R(\mathcal{E}) = \int_{-\infty}^{\infty} e^{i(\mathcal{E}+i\alpha)t/\hbar}\hat{G}^R(t)\,dt = \frac{1}{i\hbar}\int_0^{\infty} e^{i(\mathcal{E}+i\alpha-\hat{H})t/\hbar}\,dt = \frac{1}{\mathcal{E}-\hat{H}+i\alpha}\,, \tag{3.34}$$

where a small imaginary term $i\alpha$ ($\alpha > 0$) was used to make the integral converge. α will be taken to zero when evaluating functions of $\hat{G}(\mathcal{E})$. Following similar steps, one can obtain the result of the advanced Green's operator as a function of energy:

$$\hat{G}^A(\mathcal{E}) = \int_{-\infty}^{\infty} e^{i(\mathcal{E}-i\alpha)t/\hbar}\hat{G}^A(t)\,dt = \frac{1}{-i\hbar}\int_{-\infty}^{0} e^{i(\mathcal{E}-i\alpha-\hat{H})t/\hbar}\,dt = \frac{1}{\mathcal{E}-\hat{H}-i\alpha}\,. \tag{3.35}$$

$\hat{G}(\mathcal{E})$ is directly related to the LDOS of the system. To obtain the LDOS, we first express $\hat{G}^R(\mathcal{E})$ in the basis $|n\rangle$ which are eigenstates of $\hat{H}$,

$$\hat{G}(\mathcal{E}) = \sum_n \frac{|n\rangle\langle n|}{\mathcal{E}-\mathcal{E}_n+i\alpha}\,, \tag{3.36}$$

Note that in the basis $|n\rangle$, $\hat{G}^R$ and $\hat{G}^A$ are related by $\hat{G}^A = \left(\hat{G}^R\right)^\dagger$, so for simplicity, we will refer to $\hat{G}^R$ as $\hat{G}$ and $\hat{G}^A$ as $\hat{G}^\dagger$. Then projecting the Green's operator into real space, we can write the Green's function as

$$G(\mathbf{r}, \mathcal{E}) = \langle \mathbf{r}|\hat{G}(\mathcal{E})|\mathbf{r}\rangle = \sum_n \frac{\langle \mathbf{r}|n\rangle\langle n|\mathbf{r}\rangle}{\mathcal{E} - \mathcal{E}_n + i\alpha} \tag{3.37}$$

$$= \sum_n |\psi_n(\mathbf{r})|^2 \left[\frac{1}{\mathcal{E} - \mathcal{E}_n} - i\frac{\alpha}{(\mathcal{E} - \mathcal{E}_n)^2 + \alpha^2}\right].$$

We see that the imaginary part of the Green's function is a Lorentzian. Upon taking the limit $\alpha \to 0$, this term turns into a delta function with a normalization factor of π, so we can write

$$\mathrm{Im}\{G(\mathbf{r}, \mathcal{E})\} = -\pi \sum_n |\psi_n(\mathbf{r})|^2 \delta(\mathcal{E} - \mathcal{E}_n) = -\pi\, \mathrm{LDOS}(\mathbf{r}, \mathcal{E})\,. \tag{3.38}$$

An important quantity that appears frequently in theoretical literature is called the spectral operator $\hat{A}(\mathcal{E})$ and is defined as:

$$\hat{A}(\mathcal{E}) = -2\mathrm{Im}\{G(\mathcal{E})\} = i[G(\mathcal{E}) - G^\dagger(\mathcal{E})]\,, \tag{3.39}$$

thus the spectral operator is related to the LDOS with

$$\mathrm{LDOS}(\mathbf{r}, \mathcal{E}) = \frac{1}{2\pi}\langle \mathbf{r}|\hat{A}(\mathcal{E})|\mathbf{r}\rangle\,. \tag{3.40}$$

Similarly, PDOS is related to the Green's function by

$$\mathrm{Im}\{G(\phi, \mathcal{E})\} = -\pi \sum_n |\langle \phi|n\rangle|^2\, \delta(\mathcal{E} - \mathcal{E}_n) = -\pi\, \mathrm{PDOS}(\phi, \mathcal{E})\,. \tag{3.41}$$

If an adsorbate is placed on a continuum, and the eigenstates of the Hamiltonian are $|n\rangle$, then we can also express the expectation value of the Green's operator in terms of the original unhybridized localized state $|\phi\rangle$ as

$$\langle \phi|\hat{G}(\mathcal{E})|\phi\rangle = \lim_{\alpha \to 0} \sum_n \frac{|\langle \phi|n\rangle|^2}{\mathcal{E} + i\alpha - \mathcal{E}_n} = \frac{1}{\mathcal{E} - \mathcal{E}_\phi - [\Delta(\mathcal{E}) + i\Gamma(\mathcal{E})]}\,, \tag{3.42}$$

where $\Delta(\mathcal{E}) + i\Gamma(\mathcal{E})$ is called the retarded self-energy. The imaginary part of the expectation value, and therefore PDOS, can thus be rewritten in terms of the real and imaginary parts of the retarded self-energy:

$$-\frac{1}{\pi}\mathrm{Im}\{G(\phi,\mathcal{E})\} = \frac{1}{\pi}\frac{\Gamma(\mathcal{E})}{\left[\mathcal{E}-\mathcal{E}_{\phi}-\Delta(\mathcal{E})\right]^{2}-\Gamma(\mathcal{E})^{2}} = \mathrm{PDOS}(\phi,\mathcal{E}) \ . \qquad (3.43)$$

Here we see that the resonance peak in PDOS is renormalized to around $\mathcal{E} = \mathcal{E}_{\phi} + \Delta(\mathcal{E})$, and the width of the resonance is renormalized by the imaginary part of the self-energy $\Gamma(\mathcal{E})$. These are the two main effects of hybridization, namely, broadening and shifting the adsorbate energy levels. We will later discuss the effects of adsorbate hybridization on transport characteristics in graphene in section 3.3.2.

3.2.3 Phase Transitions of Molecular Adsorbates on Surfaces

Phase transitions are ubiquitous in the natural world. Some exhibit dramatic changes in structural symmetry, while others show only gradual changes. In the modern classification of phase transitions there are two distinct categories: first-order and continuous phase transitions.[53] First order phase transitions exhibit a discontinuity in the first derivative of the free energy with respect to some thermodynamic variable, for instance at the phase transition point of ice melting into liquid water, the entropy increases discontinuously as a function of temperature as the system transforms from an ordered solid into a disordered liquid. A latent heat $Q = T\Delta S$ is associated with this phase transition, where the heat provided is used to increase the entropy by ΔS at the transition temperature T. Another characteristic of first-order phase transitions is coexistence of phases within the material with clearly defined phase boundaries. Such phase transitions include temperature driven transitions (such as water boiling), pressure driven transitions (such as ice melting under pressure), magnetic field driven transitions (such as type-I superconductors), and charge driven transitions (such as the one described in chapter 5). Charge-induced first-order phase transitions in few-layer transition metal dichalcogenides have also been demonstrated.[54]

On the other hand, continuous phase transitions (which include second-order phase transitions) have continuous first derivatives of the free energy. These phase transitions do not involve latent heat and are thus more gradual. A well-known example is the ferromagnetic transition at the Curie temperature. In addition, exotic continuous phase transitions with non-simultaneous breaking of orientational and translational symmetry can occur in reduced dimensions due to strong fluctuations.[55]

In discussing phase transitions, it is useful to consider a system and its surrounding environment, with which some thermodynamic quantities can be exchanged. Systems that can exchange energy with the environment (either in the form of heat or work), but not particles are called closed systems. Systems that can exchange both energy and particles with the environment are called open systems. In closed systems, four useful energies can be defined for application to different scenarios.[56] These energies are summarized in Table 3.1.

Name	Definition	Change in energy	Meaning in closed system	Use cases
Internal energy	U	$dU = -pdV + TdS + \sum_i \mu_i dN_i$	Total energy to create isolated system	Ideal gas
Enthalpy	$H = U + pV$	$dH = Vdp + TdS + \sum_i \mu_i dN_i$	Under constant p, maximum amount of extractable heat or other non-pV work	Exothermic/endothermic chemical reactions at constant pressure
Helmholtz free energy	$F = U - TS$	$dF = -pdV - SdT + \sum_i \mu_i dN_i$	Under constant T, maximum amount of extractable work (pV or otherwise)	Isothermic reactions with changing pressure and volume, *e.g.* explosions
Gibbs free energy	$G = U + pV - TS$	$dG = Vdp - SdT + \sum_i \mu_i dN_i$	Under constant p, T, maximum amount of extractable non-pV work	Isothermic, isobaric reversible reactions, *e.g.* melting, acid dissociation, electrolysis

Table 3.1: Summary of thermodynamic free energies in closed systems. The four different energies each apply to different scenarios: isolated systems, isothermic, isobaric, and both isothermic and isobaric.

The Gibbs free energy is particularly useful for many physical phase transitions such as solid-liquid or liquid-gas transitions. One useful property of the Gibbs free energy is that it tends to minimize under constant pressure p and temperature T. This can be shown by considering the tendency of the system plus reservoir to maximize its total entropy. If the change in the entropy of the system is dS_{sys} and the change in the entropy of the reservoir is dS_{res}, then the increase in total entropy is

$$dS_{total} = dS_{sys} + dS_{res} \quad . \tag{3.44}$$

Applying the thermodynamic identity in the form of

$$dS = \frac{1}{T} dU + \frac{p}{T} dV - \frac{\mu}{T} dN \quad , \tag{3.45}$$

and assuming no particles are exchanged between system and reservoir (*i.e.* $dN = 0$), we can express the total entropy in terms of the reservoir's thermodynamic variables as

$$dS_{total} = dS_{sys} + \frac{1}{T_{res}} dU_{res} + \frac{p_{res}}{T_{res}} dV_{res} \quad . \tag{3.46}$$

Since at equilibrium, the temperature and pressure of the system and the reservoir are the same, and the gain in the reservoir's internal energy is equal to the loss in the system's internal energy $dU_{res} = -dU_{sys}$, and by the same reasoning $dV_{res} = -dV_{sys}$, we can rewrite the total entropy as

$$dS_{total} = -\frac{1}{T_{sys}} \left(dU_{sys} - T_{sys} dS_{sys} + p_{sys} dV_{sys} \right) = -\frac{1}{T_{sys}} dG_{sys} \quad . \tag{3.47}$$

This shows that since the total entropy tends to increase, the Gibbs free energy of the system tends to decrease. Equilibrium is reached when the total entropy is maximized, or equivalently, when the Gibbs free energy of the system is minimized, *i.e.* $dG = 0$. This means that given two different material phases with Gibbs free energies G_1, G_2, the system tends to choose the phase with the lowest Gibbs free energy. On the other hand, if a material is equally stable in either phase, then $G_1 = G_2$. This is the condition for finding the phase transition point. The phase boundary can be expressed in terms of variables such as pressure and temperature by finding the line where the derivatives of the Gibbs free energies are equal to each other, *i.e.* $dG_1 = dG_2$. This yields the Clausius-Clapeyron relation, which describes the slope of the phase boundaries.

If, however, the system can exchange particles with the reservoir in addition to heat under constant temperature and chemical potential, then the relevant free energy that is minimized is the grand potential, which is defined as

$$\Phi = U - TS - \mu N \ . \tag{3.48}$$

Following the reasoning of (3.47), we find that

$$\begin{aligned} dS_{total} &= dS_{sys} + \frac{1}{T_{res}} dU_{res} - \frac{\mu_{res}}{T_{res}} dN_{res} \\ &= -\frac{1}{T_{sys}}\left(dU_{sys} - T_{sys} dS_{sys} - \mu_{sys} dN_{sys}\right) = -\frac{1}{T_{sys}} d\Phi_{\mathrm{sys}} \ , \end{aligned} \tag{3.49}$$

so the grand potential tends to minimize in such a system.

It is instructive to consider the case of a system of molecules that has a charged liquid phase as well as an electrically neutral solid (*i.e.* condensed) phase. In this example the important thermodynamic variable is the electron chemical potential of the substrate, which determines the molecular phase. The electron chemical potential can be altered by electron exchange with a charge reservoir, but the number of molecules remains fixed. This is thus a half-open system (it is, in fact, a system that we have explored experimentally as described in chapter 5). In this case, the grand potential only includes the chemical potential of particles that can be exchanged with the reservoir, which are the electrons, so the grand potential is written as

$$\Phi = U - TS - \mathcal{E}_F N_e \ , \tag{3.50}$$

where N_e is the number of electrons in the system, and $\mathcal{E}_F$ is the chemical potential of the electrons. The thermodynamic identity for this system includes the chemical potential for molecules in the liquid and condensed phase, μ_l and μ_c

$$dU = -SdT - pdV - N_e d\mathcal{E}_F + \mu_l dN_l + \mu_c dN_c \ , \tag{3.51}$$

where N_l is the number of molecules in the isolated phase, and N_c is the number of molecules in the condensed phase. Since the total number of molecules is conserved, $dN_c = -dN_l$, and we find that under conditions of constant temperature, constant volume, and a given number of liquid molecules N_l,

$$\left.\frac{d\Phi(T,V,N_l)}{d\mathcal{E}_F}\right|_{T,V,N_l} = -N_e \ . \tag{3.52}$$

In chapter 5, we discuss the observed phase transition between liquid and condensed phase molecules using the grand potential formalism, where we show that the phase transition is first order.

3.2.4 Solid, Liquid and Gas Phases in Two Dimensions

Adsorbates on surfaces can self-assemble due to interatomic forces to form solid or liquid phases. While a solid is characterized by both orientational and translational order and a clearly defined periodicity, liquids generally lack such rigid structure and instead show a shell-like structure as depicted in Fig. 3.6. Gases, on the other hand, have completely uncorrelated particle distributions. To characterize the structure of different phases, we introduce two quantities which summarize the structural distribution of constituent particles: the radial distribution function and the structure factor.

The radial distribution function $g(r)$ represents the average probability of finding a particle at radius r with respect to a central particle, and is defined as

$$g(r) = \left\langle \frac{N_i(r, r+dr)}{\rho 2\pi r dr} \right\rangle , \tag{3.53}$$

where $N_i(r, r+dr)$ is the number of particles located within a shell of width dr a radius r away from particle i. ρ is the average density of particles over the sample area, and the average in $g(r)$ is taken over all possible central particles i.

The radial distribution function $g(r)$ is actually a reduced case of the pair correlation function $g(\mathbf{r}_1, \mathbf{r}_2)$ for an isotropic system (*i.e.* one that only depends on $\mathbf{r} = |\mathbf{r}_1 - \mathbf{r}_2|$), and can therefore be written as $g(\mathbf{r})$. The pair correlation function is the probability of finding particles at both $\mathbf{r}_1$ and $\mathbf{r}_2$. The structure factor is related to $g(\mathbf{r})$ by a Fourier transform

$$S(\mathbf{q}) = 1 + \rho \int d\mathbf{r}\, e^{-i\mathbf{q}\cdot\mathbf{r}} g(\mathbf{r}) \, . \tag{3.54}$$

In terms of discrete particle positions, $S(\mathbf{q})$ is also defined as

$$S(\mathbf{q}) = \frac{1}{N} \sum_{i,j} e^{-i\mathbf{q}\cdot(\mathbf{R}_i - \mathbf{R}_j)} \ , \tag{3.55}$$

where N is the number of particles in the sample area, and $\mathbf{R}_i$ and $\mathbf{R}_j$ denote pairs of particle positions.

Fig. 3.7 (a)-(c) show the real space structure as well as $g(r)$ and $S(\mathbf{q})$ for a two-dimensional solid, liquid, and gas. In the solid triangular lattice phase $g(r)$ shows crystalline peaks and $S(\mathbf{q})$ reflects the periodicity of the close-packed triangular lattice. In the liquid phase (simulated by a Monte Carlo method with Lennard-Jones interparticle potentials) $g(r)$ shows oscillating peaks of roughly equal distance, reflecting the shell-like structure of liquids. $g(r)$ also eventually decays to 1, reflecting the loss of long-range correlation. $S(\mathbf{q})$ here shows oscillations and is isotropic. In the gas phase, the particle positions are uncorrelated, and both $g(r)$ and $S(\mathbf{q})$ (except for the delta function peak at 0) are identically 1 everywhere.

In chapter 5, we show that molecular adsorbates with repulsive Coulomb interparticle potentials on graphene exhibit liquid-like structure by analyzing their $g(r)$ and $S(\mathbf{q})$.

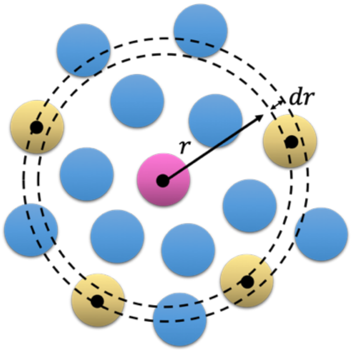

Fig. 3.6 Shell-like structure of liquids. The structure of a liquid shows concentric shells of particles, but has no long range orientational order. The radial distribution function counts the number of particles within dr of radius r, normalized by the average probability of finding a particle within the area of the ring.

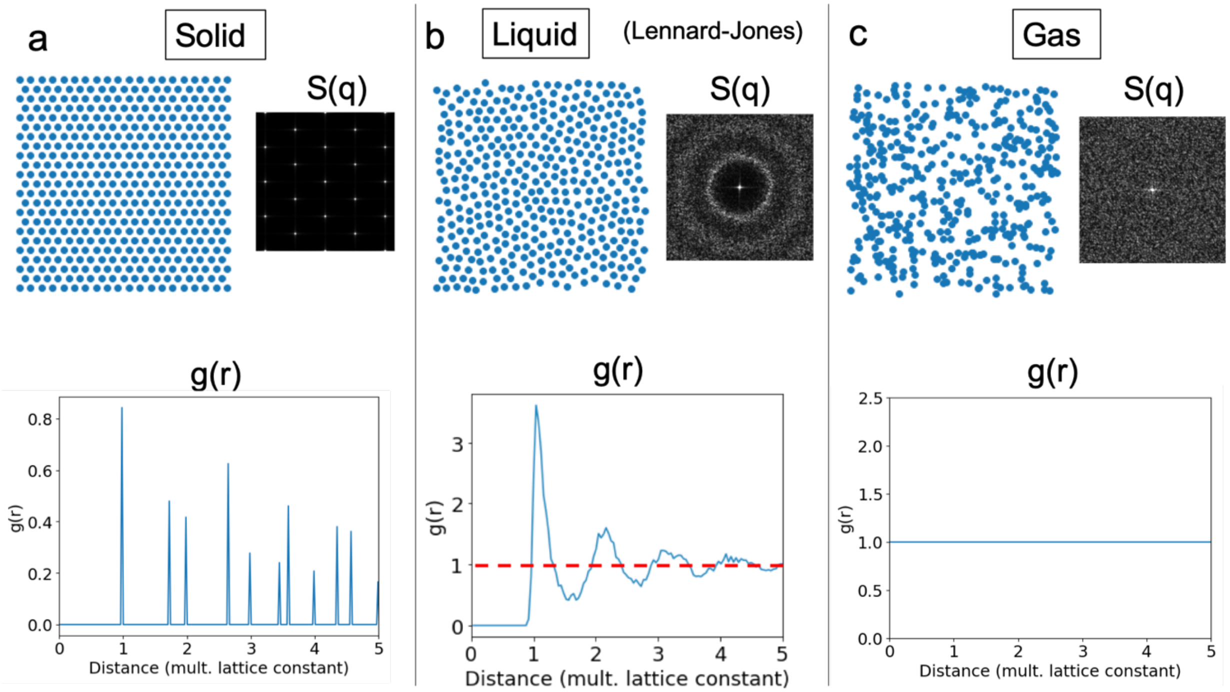

Fig. 3.7 Two-dimensional solid, liquid, and gas phases. (a) A close-packed two-dimensional solid exhibits sharp peaks in the radial distribution function and the structure factor. (b) The distribution of particles in a Lennard-Jones liquid shows a shell-like structure in the radial distribution function and an isotropic structure factor. (c) The distribution of particles in a gas is uncorrelated and its radial distribution function is uniform everywhere. The structure factor is also featureless.

3.3 Electron Transport and Impurity Scattering in Graphene

Adsorbates not only produce charge transfer, but they can also act as scatterers for electrons in graphene. In this section I will explain how adsorbates influence electron transport in graphene. I will first introduce the concept of conductivity in an isotropic conductor from Boltzmann transport theory.[57] I will then follow the T-matrix formalism for calculating the scattering time constant for resonant adsorbates.[58,59] These theoretical foundations are the basis for the gate-dependent conductivity observed in our molecule-decorated graphene devices, and also for molecular electromigration phenomena.

3.3.1 Boltzmann Transport Theory and Conductivity

In the Boltzmann theory of transport, electrons undergo collisions which hinder their motion forward. Unlike the Drude model, which assumes a fixed mean-free scattering time τ overall, the Boltzmann theory allows for a position, wavevector, and band index-dependent mean free time: $\tau = \tau_n(\mathbf{r}, \mathbf{k})$, where n is the band index, $\mathbf{r}$ is the position of the electron, and $\mathbf{k}$ is its wavevector. Collisions drive the distribution of electrons towards local thermodynamic equilibrium by obliterating any information about the non-equilibrium distribution function $g_n(\mathbf{r}, \mathbf{k}, t)$ prior to the collision, and by maintaining the local equilibrium distribution function in the form of a Fermi-Dirac distribution (with a well-defined local chemical potential μ).

$$g_n^0(\mathbf{r}, \mathbf{k}) = \frac{1}{e^{(\mathcal{E}_n - \mu(\mathbf{r}))/k_B T(\mathbf{r})} + 1}. \tag{3.56}$$

Since the probability that an electron suffers a collision that changes its wavevector and/or band index in time dt is $dt/\tau_n(\mathbf{r}, \mathbf{k})$, and the number of electrons which scatter out of the state $(n, \mathbf{r}, \mathbf{k})$ must equal the number of those which scatter into the state in equilibrium, we obtain

$$dg_n(\mathbf{r}, \mathbf{k}, t) = \frac{dt}{\tau_n(\mathbf{r}, \mathbf{k})} g_n^0(\mathbf{r}, \mathbf{k}), \tag{3.57}$$

This statement is known as the relaxation-time approximation. Given this assumption, we can calculate the non-equilibrium distribution function in the presence of external fields and temperature gradients.

Let us consider the number of electrons dN in a volume element $d\mathbf{r}\, d\mathbf{k}$ about $(\mathbf{r}, \mathbf{k})$, given the distribution function $g_n(\mathbf{r}, \mathbf{k}, t)$. dN can be expressed as

$$dN = g_n(\mathbf{r}, \mathbf{k}, t) \cdot 2 \frac{d\mathbf{r}\, d\mathbf{k}}{(2\pi)^d}, \tag{3.58}$$

in d dimensions and accounting for spin degeneracy. Now let us consider how the electrons in dN arrived at the volume element $d\mathbf{r}\, d\mathbf{k}$ about $(\mathbf{r}, \mathbf{k})$. In order to get to this volume element, some electrons must have suffered a collision at time t' prior to t which transported them from $d\mathbf{r}'\, d\mathbf{k}'$ about $(\mathbf{r}(t'), \mathbf{k}(t'))$ towards $(\mathbf{r}(t), \mathbf{k}(t))$ deterministically by the semiclassical equations of motion. The number of electrons which emerge from collisions at $(\mathbf{r}(t'),\mathbf{k}(t'))$ and are transported to $(\mathbf{r}(t),\mathbf{k}(t))$ in this way is

$$\frac{dt'}{\tau_n(\mathbf{r}(t'),\mathbf{k}(t'))} g_n^0(\mathbf{r}(t'),\mathbf{k}(t')) \cdot 2\frac{d\mathbf{r}\,d\mathbf{k}}{(2\pi)^d}, \tag{3.59}$$

where we have used Liouville's theorem to replace $d\boldsymbol{r}'\,d\boldsymbol{k}'$ with $d\boldsymbol{r}\,d\boldsymbol{k}$. However, of this number of electrons, only some fraction $P_n(\mathbf{r},\mathbf{k},t,t')$ manage to reach $(\mathbf{r}(t),\mathbf{k}(t))$ without suffering another collision. Therefore, the total number of electrons dN that actually arrive at $(\mathbf{r}(t),\mathbf{k}(t))$ is found by integrating all prior collision times t', accounting for attrition by further collisions, so we find

$$dN = 2\frac{d\mathbf{r}\,d\mathbf{k}}{(2\pi)^d}\int_{-\infty}^{t} \frac{dt' g_n^0(\mathbf{r}(t'),\mathbf{k}(t'))P_n(\mathbf{r},\mathbf{k},t,t')}{\tau_n(\mathbf{r}(t'),\mathbf{k}(t'))}, \tag{3.60}$$

Comparing (3.60) with (3.58) yields

$$g_n(\mathbf{r},\mathbf{k},t) = \int_{-\infty}^{t} \frac{dt' g_n^0(\mathbf{r}(t'),\mathbf{k}(t'))P_n(\mathbf{r},\mathbf{k},t,t')}{\tau_n(\boldsymbol{r}(t'),\mathbf{k}(t'))}. \tag{3.61}$$

For the sake of simpler notation, let us drop the indices $\mathbf{r},\mathbf{k}$ and n, with the understanding that they denote a particular state in phase space, for a particular band. To calculate the probability of scattering between t and t', which is $P(t,t')$, one can first consider that the probability of an electron suffering a collision between t' and $t'+dt'$, which is just $dt'/\tau(t')$. Then the probability that an electron survives and continues to be transported to time t without a collision is $[1-dt'/\tau(t')]P(t,t'+dt')$, which is equal to $P(t,t')$,

$$P(t,t') = \left[1-\frac{dt'}{\tau(t')}\right]P(t,t'+dt'). \tag{3.62}$$

The resulting differential equation from taking $t'\to 0$ is

$$\frac{\partial}{\partial t'}P(t,t') = \frac{P(t,t')}{\tau(t')}. \tag{3.63}$$

The solution of this differential equation is an exponential decay

$$P(t,t') = e^{-\int_{t'}^{t}\frac{d\bar{t}}{\tau(\bar{t})}}. \tag{3.64}$$

If τ is time-independent (*i.e.* only depends on $\mathbf{k}$ through $\mathcal{E}(\mathbf{k})$), such as for isotropic systems, $P(t,t')$ can be further reduced to

$$P(t,t') = e^{-(t-t')/\tau(\mathcal{E}(\mathbf{k}))}. \tag{3.65}$$

Using (3.63), we can now rewrite (3.61) as

$$g(t) = \int_{-\infty}^{t} dt' g^0(t') \frac{\partial}{\partial t'} P(t,t') \, , \tag{3.66}$$

which upon integration by parts, using the physical constraint $P(t, -\infty) = 0$ becomes

$$g(t) = g^0(t) - \int_{-\infty}^{t} dt' P(t,t') \, \frac{d}{dt'} g^0(t') \, . \tag{3.67}$$

This means that the non-equilibrium distribution function can be expressed as the equilibrium distribution function plus a small correction term. In order to understand how this correction term reacts to external driving forces such as electric field, temperature gradient and chemical potential gradient, we can consider the form of the total derivative on the equilibrium distribution

$$\frac{dg^0(t')}{dt'} = \frac{\partial g^0}{\partial \mathcal{E}} \boldsymbol{\nabla}_{\mathbf{k}} \mathcal{E} \cdot \frac{d\mathbf{k}}{dt'} + \frac{\partial g^0}{\partial T} \boldsymbol{\nabla}_{\mathbf{r}} T \cdot \frac{d\mathbf{r}}{dt'} + \frac{\partial g^0}{\partial \mu} \boldsymbol{\nabla}_{\mathbf{r}} \mu \cdot \frac{d\mathbf{r}}{dt'} \, . \tag{3.68}$$

Taking derivatives of (3.56) and using the semiclassical equations of motion,

$$\frac{d\mathbf{r}}{dt} = \mathbf{v}(\mathbf{k}) = \frac{1}{\hbar} \boldsymbol{\nabla}_{\mathbf{k}} \mathcal{E} \, , \tag{3.69}$$

$$\hbar \frac{d\mathbf{k}}{dt} = -e[\mathbf{E} + \frac{1}{c} \mathbf{v}(\mathbf{k}) \times \mathbf{H}(\mathbf{r}, t)] \, , \tag{3.70}$$

and taking the magnetic field to be zero ($\mathbf{H} = 0$), we find that

$$g(t) = g^0(t) + \int_{-\infty}^{t} dt' P(t,t') \frac{\partial f}{\partial \mathcal{E}} \mathbf{v} \cdot (e\mathbf{E} + \boldsymbol{\nabla} \mu + \frac{\mathcal{E} - \mu}{T} \boldsymbol{\nabla} T) \, , \tag{3.71}$$

where f is the Fermi function evaluated at the local temperature and chemical potential. Under conditions of no chemical potential gradient or temperature gradient, and using the assumption of time-independent τ in (3.65), we arrive at the non-equilibrium distribution function of DC electrical transport in a conductor

$$g(\mathbf{k}) = g^0(\mathbf{k}) - e\mathbf{E} \cdot \mathbf{v}(\mathbf{k}) \tau\big(\mathcal{E}(\mathbf{k})\big) \frac{\partial f}{\partial \mathcal{E}} \, , \tag{3.72}$$

The Fermi surface of the non-equilibrium distribution function $g(\mathbf{k})$ under an externally applied electric field **E** is visualized in Fig. 3.8. For both hole-like and electron-like carriers, the Fermi surface is seen to shift uniformly in the opposite direction of the applied electric field.

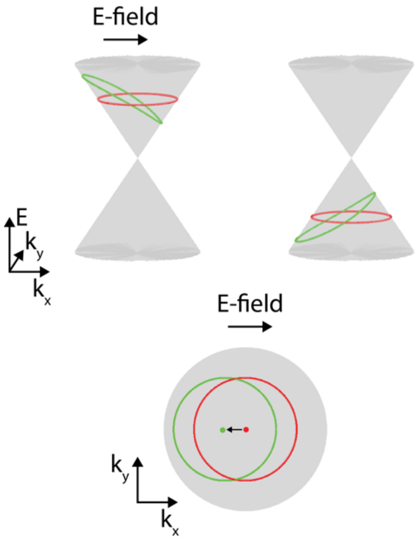

Fig. 3.8 Fermi surface shift under an externally applied electric field. The Fermi surface of electron- and hole-doped graphene near the K point is shown. The red circles indicate the Fermi surfaces under equilibrium conditions, without applying an electric field. The green circles indicate the shifted Fermi surfaces due to an externally applied electric field.

To calculate the conductivity in a single band, we first express the current density **j** as the number of electrons with momentum **k** multiplied by their velocity and integrated over momentum space:

$$\mathbf{j} = -e \int 2 \frac{d\mathbf{k}}{(2\pi)^d} \mathbf{v}(\mathbf{k}) g(\mathbf{k}) \, . \tag{3.73}$$

Arranged into the form of $\mathbf{j} = \boldsymbol{\sigma}\mathbf{E}$, we see that the conductivity tensor for band n is

$$\boldsymbol{\sigma}_n = e^2 \int 2 \frac{d\mathbf{k}}{(2\pi)^d} \tau_n\big(\mathcal{E}_n(\mathbf{k})\big) \mathbf{v}_n(\mathbf{k}) \mathbf{v}_n(\mathbf{k}) \left(-\frac{\partial f}{\partial \mathcal{E}}\right)\bigg|_{\mathcal{E}=\mathcal{E}_n(\mathbf{k})} , \tag{3.74}$$

so that the total conductivity tensor is

$$\boldsymbol{\sigma} = \sum_{\boldsymbol{n}} \boldsymbol{\sigma}_n \ . \tag{3.75}$$

The DC conductivity in the direction parallel to the current is then

$$\sigma_{xx} = e^2 \sum_{\boldsymbol{n}} \int \frac{d^2k}{2\pi^2} \tau_n\big(\mathcal{E}_n(\mathbf{k})\big) v_{nk,x}^2 \left(-\frac{\partial f}{\partial \mathcal{E}}\right)\bigg|_{\mathcal{E}=\mathcal{E}_n(\mathbf{k})} , \tag{3.76}$$

where $v_{nk,x}$ denotes the component of the band velocity parallel to the current direction. Furthermore, we can make the extra assumption that the band structure is isotropic near the Dirac point for low adsorbate densities, so that we can substitute $v_{nk,x} = v_{nF}\cos(\theta)$, where v_{nF} is the isotropic Fermi velocity of band n and θ is the angle between the current and the band velocity. The isotropic assumption also leads to the property that the scattering time τ_n only depends on $\mathbf{k}$ through $\mathcal{E}_n(\mathbf{k})$, and not on $\mathbf{k}$ explicitly. In addition, since $\partial f/\partial\mathcal{E}$ is only non-zero in an interval of order k_BT around the Fermi level, at zero temperature, $-\partial f/\partial\mathcal{E}$ reduces to the Dirac delta function, so that we can further simplify the DC conductivity to

$$\begin{aligned}\sigma_{xx} &= \frac{e^2}{2\pi^2}\sum_{\boldsymbol{n}}\tau_n(\mathcal{E}_F)\int v_{nF}^2\cos^2(\theta)\,d\theta\,\delta\big(\mathcal{E}-\mathcal{E}_n(k)\big)\,k\,dk \\ &= \frac{e^2}{2\pi}\sum_{\boldsymbol{n}}\tau_n(\mathcal{E}_F)v_{nF}^2\int k\delta\big(\mathcal{E}-\mathcal{E}_n(k)\big)dk \\ &= \frac{e^2}{2\pi}\sum_{\boldsymbol{n}}\tau_n(\mathcal{E}_F)v_{nF}^2\cdot\frac{k_{nF}}{\hbar v_{nF}} \\ &= \frac{2e^2}{h}\sum_{\boldsymbol{n}}v_{nF}k_{nF}\tau_n(\mathcal{E}_F)\ .\end{aligned} \tag{3.77}$$

In order to obtain the conductivity of graphene in the presence of scattering impurities, it remains to calculate the scattering time constant τ as a function of the Fermi level.

3.3.2 Charged Impurity Scattering in Graphene

Adsorbates on a conductor's surface not only provide additional energy levels for electrons to hop into, but can also induce potentials that scatter incoming electrons. These processes change the conductivity of the material. In order to understand the effects of hybridization on the conductive substrate, we can employ Green's function methods to calculate the scattering time constant, and thereby model the conductivity of the system.[58]

A simple but crude framework to describe an adsorbate-metallic continuum system with a very localized adsorbate-induced potential is the Fano-Anderson model. In this model, a localized impurity state $|\phi\rangle$ with unhybridized energy $\mathcal{E}_i$ is brought into contact with a host atom n in the metal with states $|n\rangle$. γ is the hopping strength from the adsorbate to the host atom. The Hamiltonian of the system can then be written as

$$\begin{aligned}H &= -t\sum_{\langle l,m\rangle}c_l^\dagger c_m + \mathcal{E}_i a^\dagger a + \gamma(c_n^\dagger a + a^\dagger c_n) \\ &= -t\sum_{\langle l,m\rangle}|l\rangle\langle m| + \mathcal{E}_i|\phi\rangle\langle\phi| + \gamma|n\rangle\langle\phi| + \gamma|\phi\rangle\langle n|.\end{aligned} \tag{3.78}$$

Here a (or $a^\dagger$) annihilates (or creates) an electron in the local impurity state, c_l or $c_l^\dagger$ annihilates and creates an electron in metal atom l while c_n or $c_n^\dagger$ annihilates and creates an electron in the host metal atom. By writing the electron wavefunction as a linear combination of atomic orbitals $|\Psi\rangle = \sum_l \psi_l |l\rangle + \varphi|\phi\rangle$, and projecting the Schrödinger equation onto the impurity state $\langle\phi|$, we can write

$$\langle\phi|\mathcal{E} - H|\Psi\rangle = 0\,, \tag{3.79}$$

This expression can be used to relate the amplitude φ to the other amplitudes ψ_l, specifically, the non-vanishing cross terms yield:

$$\varphi = \frac{\gamma}{\mathcal{E} - \mathcal{E}_i}\psi_n\,, \tag{3.80}$$

where ψ_n is the wavefunction amplitude on the host atom. This allows us to eliminate the amplitude φ by writing a hybridized state

$$|\xi\rangle = \psi_n\left[|n\rangle + \frac{\gamma}{\mathcal{E} - \mathcal{E}_i}|\phi\rangle\right]. \tag{3.81}$$

If we want to express $H|\xi\rangle$ in terms of an effective potential on the carbon site, then

$$V = \langle\xi|H|\xi\rangle = \frac{\gamma^2}{\mathcal{E} - \mathcal{E}_i}\,, \tag{3.82}$$

and the Hamiltonian can be reduced to

$$\widetilde{H} = -t\sum_{\langle l,m\rangle} c_l^\dagger c_m + V c_n^\dagger c_n \text{ ,where } V = \frac{\gamma^2}{\mathcal{E} - \mathcal{E}_i} \tag{3.83}$$

and the problem of electrons scattering in the impurity-graphene system is reduced to a problem of electron scattering in an effective potential V induced by the adsorbate.

Electrons scattering in a potential can be treated with the formalism of Green's functions. The Hamiltonian in Eq. (3.83) can be seen as the sum of two parts, an unperturbed Hamiltonian of electrons in the conductor $\widehat{H}^0 = -t\sum_{\langle l,m\rangle} c_l^\dagger c_m$ and the perturbing self-energy imposed by the impurity on the host atom site $\widehat{V} = V c_n^\dagger c_n$. With these two parts, the full Green's operator can be defined as

$$\widehat{G}(\mathcal{E}) = \left(\mathcal{E} - \widehat{H}^0 - \widehat{V} + i\alpha\right)^{-1}\,, \tag{3.84}$$

and the unperturbed Green's operator can be defined as

$$\widehat{G}^0(\mathcal{E}) = \left(\mathcal{E} - \widehat{H}^0 + i\alpha\right)^{-1}\,. \tag{3.85}$$

The full Green's operator can actually be expressed in terms of the unperturbed Green's operator and the perturbing potential by writing

$$\hat{G}(\mathcal{E}) = \left(\mathcal{E} - \hat{H}^0 - \hat{V} + i\alpha\right)^{-1} \qquad (3.86)$$
$$= \left[\mathcal{E} - \hat{H}^0 + i\alpha\right]^{-1}\left[1 - \hat{V}\left(\mathcal{E} - \hat{H}^0 + i\alpha\right)^{-1}\right]^{-1}$$
$$= \hat{G}^0\left(1 - \hat{V}\hat{G}^0\right)^{-1} .$$

This can be further expanded to yield

$$\hat{G}(\mathcal{E}) = \hat{G}^0\left(1 - \hat{V}\hat{G}^0\right)^{-1} = \hat{G}^0 + \hat{G}^0\hat{V}\hat{G}^0 + \hat{G}^0\hat{V}\hat{G}^0\hat{V}\hat{G}^0 + \cdots \qquad (3.87)$$
$$= \hat{G}^0 + \hat{G}^0\left(\hat{V} + \hat{V}\hat{G}^0\hat{V} + \cdots\right)\hat{G}^0$$
$$= \hat{G}^0 + \hat{G}^0\hat{T}\hat{G}^0 \quad ,$$

where the T-matrix is defined as the series sum $\hat{V} + \hat{V}\hat{G}^0\hat{V} + \cdots$, whose terms can be collected and re-expressed as

$$\hat{T}(\mathcal{E}) = \left(1 - \hat{V}\hat{G}^0\right)^{-1}\hat{V} \quad . \qquad (3.88)$$

If we define the local unperturbed Green's function $g_0(\mathcal{E}) = \hat{G}^0(\mathbf{k}, \mathcal{E}) = \sum_{\mathbf{k}}(\mathcal{E} - \mathcal{E}_k + i\alpha)^{-1}$, then the resulting T-matrix can be reduced to

$$\langle \mathbf{k}'|T|\mathbf{k}\rangle \equiv T(\mathcal{E}) = \frac{\gamma^2}{\mathcal{E} - \mathcal{E}_i - \gamma^2 g_0(\mathcal{E})} \quad . \qquad (3.89)$$

Assuming the conductivity is isotropic, as in the case of graphene due to C_6 symmetry, the structure of the T-matrix does not depend explicitly on the incoming and outgoing wavevectors **k** and $\mathbf{k}'$, but only on **k** and $\mathbf{k}'$ through the energy of the electrons $\mathcal{E}(\mathbf{k})$. The T-matrix is important because it can be used to calculate the probability of an electron scattering from **k** to $\mathbf{k}'$, and is thus proportional to the scattering amplitude $f(\mathbf{k}', \mathbf{k})$:

$$f(\mathbf{k}', \mathbf{k}) = -\frac{m}{2\pi\hbar^2}\langle \mathbf{k}'|\hat{T}(\mathcal{E})|\mathbf{k}\,\rangle . \qquad (3.90)$$

The transition rate is then given by Fermi's golden rule:

$$\tau^{-1} = \frac{2\pi}{\hbar} n_i |T(\mathcal{E})|^2 \nu_0(\mathcal{E}) \quad , \qquad (3.\ 91)$$

where n_i is the density of impurities, and $\nu_0(\mathcal{E})$ is the local density of states. For graphene, $\nu_0(\mathcal{E})$ is modeled by

$$\nu_0(\mathcal{E}) = \frac{|\mathcal{E}|}{D^2}\Theta(D - |\mathcal{E}|)\,, \tag{3.92}$$

where Θ is the Heaviside function, and D is a high energy cutoff $\sim 6\ eV$, such that there is an overall normalization of one electron per carbon atom: $\int_{-D}^{D} \nu_0(\mathcal{E}) = 1$. Knowledge of $\nu_0(\mathcal{E})$ actually fully defines $g_0(\mathcal{E})$, and therefore $T(\mathcal{E})$ and $\tau_{\mathbf{k}}^{-1}$. This is because $g_0(\mathcal{E})$ is related to $\nu_0(\mathcal{E})$ by

$$\begin{aligned} g_0(\mathcal{E}) &= \mathcal{P}\sum_{\mathbf{k}} \frac{1}{\mathcal{E} - \mathcal{E}_{\mathbf{k}}} - i\pi \sum_{\mathbf{k}} \delta(\mathcal{E} - \mathcal{E}_{\mathbf{k}}) \\ &= \mathcal{P}\int_{-\infty}^{\infty} \frac{\nu_0(\mathcal{E}')}{\mathcal{E} - \mathcal{E}'} d\mathcal{E}' - i\pi\nu_0(\mathcal{E}), \end{aligned} \tag{3.93}$$

where $\mathcal{P}$ denotes the Cauchy principal value. For graphene, $g_0(\mathcal{E})$ can thus be re-expressed as

$$g_0(\mathcal{E}) = \frac{\mathcal{E}}{D^2}\ln\left|\frac{\mathcal{E}^2}{D^2 - \mathcal{E}^2}\right| - i\pi\frac{|\mathcal{E}|}{D^2}\Theta(D - |\mathcal{E}|)\,. \tag{3.94}$$

This result can be plugged back into (3.89) to calculate $T(\mathcal{E})$, which can then be used to determine the scattering time constant τ in (3. 91), which yields the conductivity in graphene

$$\sigma_g(\mathcal{E}) = \frac{2e^2}{h}(2\pi n_i|T(\mathcal{E})/D|^2)^{-1}\,. \tag{3.95}$$

The result of this expression is plotted in Fig. 3.9. One can observe that scattering with impurities produces asymmetric conductivities in graphene above and below the Dirac point. In particular, when the impurity resonance is above the Dirac point, the conductance is suppressed in the electron band and enhanced in the hole band. The opposite trend is predicted when the impurity resonance is below the Dirac point.

In contrast to the case of a constant scattering time, which predicts that conductivity varies linearly with carrier concentration in graphene, the Fano-Anderson model predicts a sublinear conductivity. In addition, it also predicts a strong asymmetry in electron and hole conductivity for orbital energies more than 100 meV away from the Dirac point energy. These predictions have both been observed in potassium-doped graphene samples.[60,61] Since potassium energy levels are far away from the graphene Dirac point energy and thus do not directly contribute to the density of states at the Fermi level, no atomic orbital resonance is directly seen in the conductance curve. However, it is also possible for an adsorbate to change the conductivity of graphene by directly contributing its orbital to the density of states at the Fermi level, in which case contributions from each hybridized band will need to be summed up in (3.77).

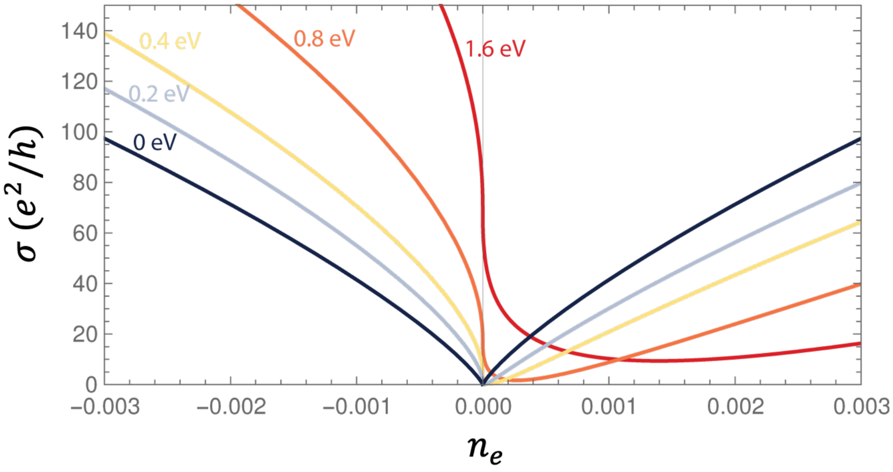

Fig. 3.9 Graphene conductance in Boltzmann transport. The conductance of graphene is plotted as a function of carrier concentration for different impurities with resonance energies 0 eV, 0.2 eV, 0.4 eV, 0.8 eV, and 1.6 eV. The impurity density $n_i = 0.06\%$, and hybridization energy $\gamma = 5.2$ eV. A significant asymmetry can be seen in the electron and hole-bands.

3.3.3 Resonant Impurity Scattering in Graphene

The model above does not account for impurity band formation at high impurity concentrations. To take this effect into account, we employ a slightly more sophisticated model that couples an impurity level to a continuum of graphene Dirac band states in a periodic Anderson model, where impurities adsorb on only one of the two sublattices in a periodic array. The impurities themselves form a superlattice, and impurity levels hybridize with graphene Dirac bands to form impurity bands. Here we assume the impurity level hybridizes with the lower Dirac band, as observed in the case of F_4TCNQ molecules (see chapter 7). The model Hamiltonian of such a system can be written as

$$H_{\mathbf{k}} = -\hbar k v_F (c^\dagger_{K,\mathbf{k}} c_{K,\boldsymbol{k}} + c^\dagger_{K',\boldsymbol{k}} c_{K',\boldsymbol{k}}) + \mathcal{E}_i a_i^\dagger a_i \\ +\Delta_K(\mathbf{k})\, a_i^\dagger c_{K,\boldsymbol{k}} + \Delta_{K'}(\mathbf{k})\, a_i^\dagger c_{K',\boldsymbol{k}} + H.c.\ , \tag{3.96}$$

where $a_i^\dagger$ and a_i destroys and creates a state $|\psi_L(\mathbf{k})\rangle$ in the impurity band, $c^\dagger_{K,k}$ and $c_{K,k}$ destroys and creates a state $\left|\psi_{K,-}(\mathbf{k})\right\rangle$ in the K band of graphene, and $c^\dagger_{K',k}$ and $c_{K',k}$ destroys and creates a state $\left|\psi_{K',-}(\mathbf{k})\right\rangle$ in the K' band. $\mathcal{E}_i$ is the impurity energy. These states can also be written in the basis of localized states on the impurity $|\phi_{L\mathbf{R}}\rangle$ and localized states on the A/B sublattices, $\left|\chi_{K,A}(\mathbf{k})\right\rangle$ and $\left|\chi_{K,B}(\mathbf{k})\right\rangle$ with

$$|\psi_L(\mathbf{k})\rangle = \frac{1}{\sqrt{N}} \sum_{\mathbf{R}} e^{i\mathbf{k}\cdot\mathbf{R}}\ |\phi_{L\mathbf{R}}\rangle\ , \tag{3.97}$$

and

$$\left|\psi_{K,-}(\mathbf{k})\right\rangle = \frac{1}{\sqrt{2}}[e^{-\frac{i\theta_{\mathbf{k}}}{2}}\left|\chi_{K,A}(\mathbf{k})\right\rangle - e^{\frac{i\theta_{\mathbf{k}}}{2}}\left|\chi_{K,B}(\mathbf{k})\right\rangle] \ , \tag{3.98}$$

$$\left|\psi_{K',-}(\mathbf{k})\right\rangle = \frac{1}{\sqrt{2}}[e^{\frac{i\theta_{\mathbf{k}}}{2}}\left|\chi_{K,A}(\mathbf{k})\right\rangle - e^{-\frac{i\theta_{\mathbf{k}}}{2}}\left|\chi_{K,B}(\mathbf{k})\right\rangle] \ , \tag{3.99}$$

Where

$$\left|\chi_{K,A}(\mathbf{k})\right\rangle = \frac{1}{\sqrt{N'}}\sum_{\mathbf{R}'} e^{i\mathbf{k}\cdot\mathbf{R}'} \ |\phi_{\mathbf{R}'A}\rangle \, , \tag{3.100}$$

And where $\mathbf{R}$ is a sum over the $N \times N$ supercell lattice vectors, $\mathbf{R}'$ is a sum over the $N' \times N'$ primitive cell lattice vectors of graphene, and N is a multiple of 3, such that the K and K' points of the graphene Brillouin zone maps to the origin of the supercell. $\theta_{\mathbf{k}}$ is the angle of $\mathbf{k}$ with respect to the real axis.

The hybridization Hamiltonian couples a state on the A sublattice to a state on the impurity and can be expressed as

$$H_{hyb} = V\sum_{\mathbf{R}} a_{i\mathbf{R}}^{\dagger} a_{iA\tau=0} + H.c. \ , \tag{3.101}$$

where τ is the vector that points from the origin of the supercell to the origin of the various primitive cells of graphene within the supercell. To obtain the off-diagonal term $\Delta(\mathbf{k})$ which couples the impurity and graphene bands, we evaluate the term $\langle\psi_L(\mathbf{k})|H_{hyb}\left|\psi_{K,-}(\mathbf{k})\right\rangle$, which yields

$$\Delta_K(\mathbf{k}) = \langle\psi_L(\mathbf{k})|H_{hyb}\left|\psi_{K,-}(\mathbf{k})\right\rangle = \frac{V}{\sqrt{2}N}e^{\frac{i\theta_{\mathbf{k}}}{2}} \ . \tag{3.102}$$

Similarly, we also find that

$$\Delta_{K'}(\mathbf{k}) = \langle\psi_L(\mathbf{k})|H_{hyb}\left|\psi_{K',-}(\mathbf{k})\right\rangle = \frac{V}{\sqrt{2}N}e^{-\frac{i\theta_{\mathbf{k}}}{2}} \ , \tag{3.103}$$

so that $\Delta_{K'}(\mathbf{k}) = \Delta_K^*(\mathbf{k})$, so the Hamiltonian takes the form

$$H_{\mathbf{k}} = \begin{bmatrix} \mathcal{E}_i & \Delta(\mathbf{k}) & \Delta^*(\mathbf{k}) \\ \Delta^*(\mathbf{k}) & -\hbar k v_F & 0 \\ \Delta(\mathbf{k}) & 0 & -\hbar k v_F \end{bmatrix}. \tag{3.104}$$

Diagonalizing this Hamiltonian yields the characteristic equation

$$(-\hbar k v_F - \mathcal{E}_{nk})[(\mathcal{E}_i - \mathcal{E}_{nk})(-\hbar k v_F - \mathcal{E}_{nk}) - 2|\Delta(\mathbf{k})|^2] = 0. \tag{3.105}$$

This shows that one linear band is unaffected by the impurity and does not hybridize at all. The unaffected linear band is the antisymmetric sum of the bands from the K and K' points. We also find that the dispersion is isotropic and only depends on k, since $|\Delta(\mathbf{k})|^2 = V^2/(2N^2)$. The remaining eigenvalues can be explicitly solved:

$$\mathcal{E}_{nk} = \frac{\mathcal{E}_i - \hbar k v_F}{2} - \frac{1}{2}\sqrt{(\mathcal{E}_i + \hbar k v_F)^2 + \frac{4V^2}{N^2}}\ . \tag{3.106}$$

The band structure of this system and its corresponding density of states is plotted in Fig. 3.10. The density of states shows the impurity resonance close to $\mathcal{E}_i$, which exhibits a characteristic Fano line shape with higher density of states closer to the Dirac point energy.

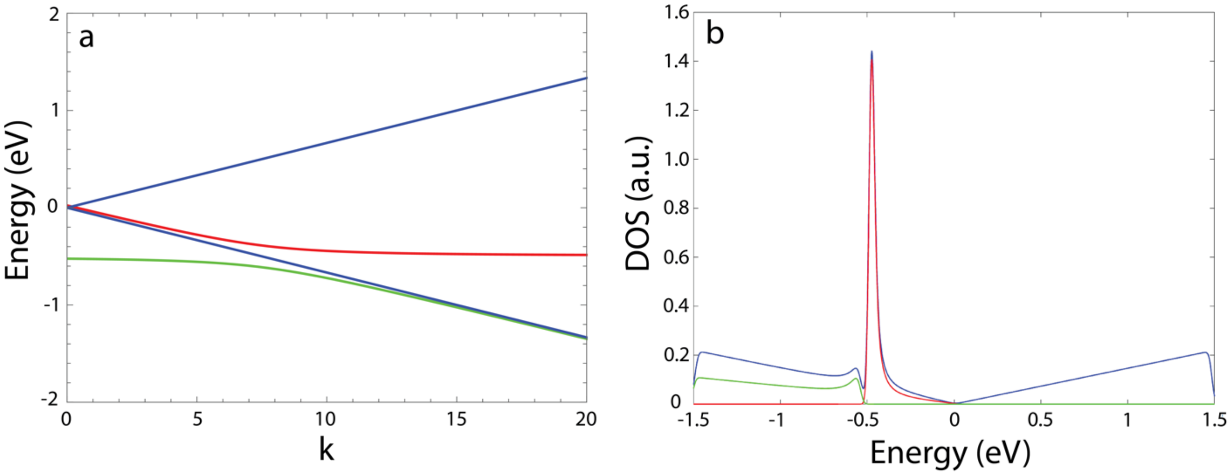

Fig. 3.10 Hybridized graphene impurity bands in the continuum model. (a) Band structure of a periodic lattice of impurities on graphene near the K point. The impurity energy is set to -0.5 eV relative to the graphene Dirac point. The resulting band structure shows two hybridized impurity bands (red and green) and unhybridized graphene Dirac bands (blue). (b) The resulting density of states from the band structure shown in (a) is plotted. The density of states of the upper impurity band is plotted in red, and the density of state of the lower impurity band is plotted in green. The blue curve shows the total density of states of the system, including unhybridized graphene density of states. Calculations done by J. Lischner.

Assuming a constant scattering time τ without dependence on energy or band index, we can sum up contributions from each band and calculate the conductivity following (3.77). We thus arrive at a crude model of the conductivity as a function of Fermi level and gate voltage. The calculated conductivity from such a band structure is plotted in Fig. 3.11 (a). When the conductivity is plotted as a function of Fermi level, a pronounced dip is seen at the energy of the molecular resonance, in addition to the linearly varying background conductivity of the graphene Dirac bands. The conductivity of graphene is reduced when the Fermi level is close to the molecular orbital energy due to electrons becoming trapped in the molecular orbitals. Furthermore, at high molecular densities, the molecular orbitals contribute a significant density of states to the system as well, which results in a Fermi level pinning effect. As electrons are added to the system through gating, instead of raising the Fermi level, they fill in empty molecular orbitals at energy of the DOS peak. As a result, the Fermi level does not change for a range of gate voltages. In this regime, the conductivity also remains roughly constant. The conductivity of molecule-decorated graphene is plotted as a function of applied gate voltage in Fig. 3.11 (b). A plateau in conductivity is observed whose range in gate voltage varies linearly with the surface molecule concentration. This model describes the basic phenomenology of gate-dependent conductance measurements of F_4TCNQ decorated-graphene devices presented in chapter 7.

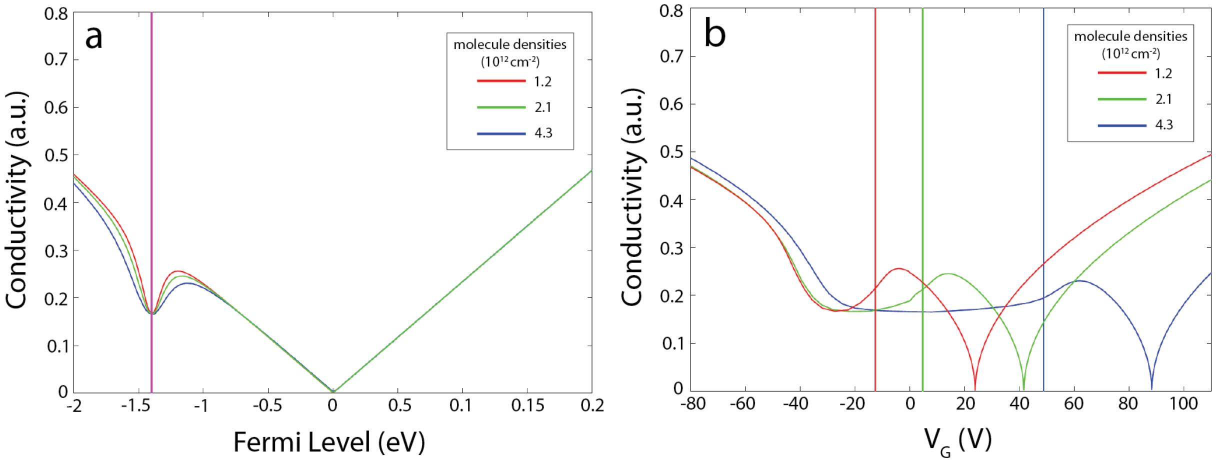

Fig. 3.11 Conductivity of impurity-decorated Graphene. The conductivity of a periodic lattice of impurities simulating F_4TCNQ on graphene is plotted in (a) as a function of Fermi level, and in (b) as a function of applied gate voltage. The impurity energy is set to -0.14 eV relative to the graphene Dirac point. The red, green, and blue curves correspond to a molecular density of 1.2×10^{12}, 2.1×10^{12} and 4.3×10^{12} molecules cm^{-2}, respectively. The red, green, and blue vertical lines correspond to the gate voltage used to induce the molecular density, which are respectively -12.6V, 4.7V, and 48.8V, given a device capacitance of 5×10^{10} electron charges cm$^{-2}V^{-1}$ (see chapter 7 for additional details, calculations by J. Lischner).

3.4 Diffusion and Electromigration of Surface Adsorbates

Diffusion and electromigration of surface adsorbates are two thermally activated processes that are important for dynamical changes in adsorbate-decorated graphene. The background theory for these topics are introduced in the following sections, whereas our specific experiments in these areas will be the focus of later chapters 6 and 8.

3.4.1 Brownian Diffusion

Brownian diffusion is a simple model that describes thermally activated motion of adsorbates on a surface. In one-dimensional Brownian diffusion, the probability of finding a particle at position x is given by the probability density function (PDF)

$$p(x,t) = \frac{1}{\sqrt{4\pi Dt}} e^{-\frac{(x-x_0)^2}{4Dt}} , \qquad (3.107)$$

where D is the diffusion constant, x_0 is the initial position of the particle, and t is the time passed. This "spreading Gaussian" PDF is a solution of the diffusion equation

$$\frac{\partial p(x,t|x_0)}{\partial t} = D\frac{\partial^2 p(x,t|x_0)}{\partial x^2} \ , \tag{3.108}$$

where $p(x,t|x_0)$ is the probability of finding the particle at position x at time t, given that it started out at position x_0 at $t = 0$ with the initial condition $p(x_0, t = 0|x_0) = \delta(x - x_0)$. Since this PDF is a Gaussian function with the expectation value $\langle x - x_0 \rangle = 0$, so on average the particle is still centered on its original position. However, the expectation value $\langle |x - x_0|^2 \rangle$ is equal to the variance of the Gaussian, which is $\sigma = 2Dt$. This means that, although on average the probability of finding the particle is still centered around its original position, its mean squared displacement (MSD) is proportional to the time elapsed. In *d*-dimensions, these properties hold true since the particle position in each coordinate is uncorrelated, so the MSD can be written as

$$\langle |\mathbf{r} - \mathbf{r}_0|^2 \rangle = \langle \Delta\mathbf{r}^2 \rangle = 2dDt\,. \tag{3.109}$$

By keeping track of the MSD of particles as a function of time, we can extract the diffusion constant D.

In the case of tracer diffusion (*i.e.* when particle concentrations are low and particles do not impede each other's motion), the MSD can also be written as a function of the hopping frequency ν, elapsed time t, and the step length a. By definition, the MSD after n steps is

$$\langle \Delta\mathbf{r}_n^2 \rangle = \langle (\mathbf{r}_{n-1} + \boldsymbol{\delta})^2 \rangle \ , \tag{3.110}$$

where $\boldsymbol{\delta}$ is the displacement at step n, and $\mathbf{r}_{n-1}$ is the displacement after $n - 1$ steps. The average is taken over all adatoms. Expanding the terms inside the average, we obtain

$$\langle \Delta\mathbf{r}_n^2 \rangle = \langle \mathbf{r}_{n-1}^2 \rangle + \langle 2\mathbf{r}_{n-1}\boldsymbol{\delta} \rangle + \langle \boldsymbol{\delta}^2 \rangle \ . \tag{3.111}$$

The term $\langle 2\mathbf{r}_{n-1}\boldsymbol{\delta} \rangle$ averages to zero because $\boldsymbol{\delta}$ is uncorrelated with the previous history of displacements, thus the MSD can be expressed recursively as

$$\begin{aligned} \langle \Delta\mathbf{r}_n^2 \rangle &= \langle \mathbf{r}_{n-1}^2 \rangle + \langle \boldsymbol{\delta}^2 \rangle \\ &= \langle \mathbf{r}_{n-2}^2 \rangle + \langle \boldsymbol{\delta}^2 \rangle + \langle \boldsymbol{\delta}^2 \rangle \\ &= n\langle \boldsymbol{\delta}^2 \rangle \qquad . \end{aligned} \tag{3.112}$$

Since the number of steps taken is just the hopping frequency multiplied by the elapsed time and the expectation value $\langle \boldsymbol{\delta}^2 \rangle = a^2$ (where a is the isotropic step length), we can express the MSD as

$$\langle \Delta\mathbf{r}^2 \rangle = \nu a^2 t\,. \tag{3.113}$$

Since adsorbate hopping from site to site is a thermally activated process which requires surmounting of a diffusion barrier E_a, we expect the hopping frequency to have a Boltzmann factor: $\nu = \nu_0 \exp\left(-E_a/k_b T\right)$, where ν_0 is the oscillation frequency of the adsorbate in the potential well of the adsorption site (*i.e.* the "attempt" frequency). Combining (3.109) and (3.113), we therefore obtain an expression for the diffusion constant in two dimensions, which allows us to extract E_a and ν_0 by fitting experimentally observed values of D as a function of temperature:

$$D = \frac{a^2 \nu_0}{4} e^{-\frac{E_a}{k_B T}} \ . \tag{3.114}$$

This simple model forms the basis of our analysis of gate-dependent molecular diffusion presented in chapter 6.

3.4.2 Electromigration

Electromigration is a phenomenon where impurities or adsorbates in a conductor diffuse in response to an electrical current. Electromigration is an important concern in the design of interconnects in integrated circuits because as metal wires are made ever smaller, electromigration of constituent atoms is a main source of failure in microelectronics. Although electromigration of bulk materials has been observed at the microscale and nanoscale,[23,62] no previous work has ever measured the electromigration force at the single-impurity level.

The electromigration force is typically discussed as having two separate components, the direct force ($\mathbf{F}_D$) and the wind force ($\mathbf{F}_W$): $\mathbf{F}_{\text{total}} = \mathbf{F}_D + \mathbf{F}_W$. The direct force is the force applied by the external electric field on the bare ion of the electromigrating atom (with valence Z) and can thus be straightforwardly expressed as $\mathbf{F}_D = Ze\mathbf{E}$. The wind force, on the other hand, is the force applied on the electromigrating atom by impinging electrons scattering off the atom. Since the wind force involves quantum mechanical scattering of electrons, it is much more complicated to calculate. To calculate the quantum mechanical expectation value of force $\langle \mathbf{F} \rangle$ on an electromigrating ion core, Ehrenfest's theorem can be used to evaluate either the momentum change of the electrons or the ions: $\langle \mathbf{F}_\mathrm{W} \rangle = \frac{d\langle \mathbf{P} \rangle}{dt} = -\frac{d\langle \mathbf{p} \rangle}{dt}$, where $\mathbf{P}$ is the momentum operator of the ion ($\mathbf{P} = -i\hbar\nabla_\mathbf{R}$), and $\mathbf{p}$ is the momentum operator of incoming electrons ($\mathbf{p} = -i\hbar\nabla_\mathbf{r}$).

We will first consider the momentum change of the electrons during scattering. In a free electron gas scattering off a long-ranged potential, the total momentum change of an electron due to scattering is calculated by summing over all pairs of allowed initial and final states with momentum $\mathbf{k}$ and $\mathbf{k}'$. The wind force can then be expressed as

$$\langle \mathbf{F}_W \rangle = -\sum_{k,k'} \hbar(\mathbf{k}' - \mathbf{k})\Gamma_{k'k} \ , \tag{3. 115}$$

where the transition rate is given by Fermi's golden rule:

$$\Gamma_{k'k} = \frac{2\pi}{\hbar} \left|\widetilde{U}_{k'k}\right|^2 [1 - g(\mathbf{k}')] g(\mathbf{k}) \delta(\mathcal{E}_{k'} - \mathcal{E}_k) \ . \tag{3. 116}$$

Here $\widetilde{U}_{k'k}$ is the transition matrix element $\langle k'|\widetilde{U}|k\rangle$, where $\widetilde{U}$ is the screened interaction potential between the ion core and electrons. $g(\mathbf{k})$ is the steady-state electron distribution function obtained in (3.72). We have also assumed only elastic scattering is allowed. However, the ballistic scattering model just described does not account for band structure effects. In a solid, electrons are *not* in eigenstates of the momentum operator $\mathbf{p}$, but are instead in Bloch states, which are a sum of plane waves with crystal momenta $\mathbf{k}+\mathbf{G}$ ($\mathbf{G}$ is a reciprocal lattice vector), so a change in the crystal momentum cannot be directly associated with the change in total momentum if significant Umklapp scattering occurs. Nevertheless, if the potential is long-ranged enough (varying on scales larger than the electron wavelength), the ballistic scattering model can still be applied in the semiclassical limit.

In order to apply the semiclassical model to Bloch states, several assumptions need to be made: (1) since Bloch wavefunctions $\psi_{n,\mathbf{k}}$ and $\psi_{n,\mathbf{k+G}}$ are completely equivalent ways of describing the *same* electron state, the wavevector $\mathbf{k}$ is defined only in the first Brillouin zone. (2) no "interband transitions" are allowed, so the band index *n* is a constant throughout the electron's motion. (3) electrons behave like wavepackets with a reasonably well-defined momentum $\mathbf{k}$ having a spread of wavevectors $\Delta\mathbf{k}$ such that $\mathbf{k}'-\mathbf{k}$ reasonably describes the momentum change of the scattered electron, and hence the usual classical equations of motion (3.69) and (3.70) are obeyed. Here the band structure only serves to dictate the dispersion relation $\mathcal{E}(\mathbf{k})$ and no other information about the periodic potential of ions is known. This approach has been taken by Solenov *et al.* to predict the electromigration force in a poorly screened environment such as graphene, where Coulomb potentials from adsorbates can be long-ranged.[63,64]

One interesting consequence of scattering in the semiclassical limit is the concept of a *hole wind* when the Fermi level is near the top of a valence band. To understand how an electron hole can transfer momentum to a scatterer, one must first understand how electrons and holes move in an applied electric field. When an electric field is applied to a material with a hole-like Fermi surface whose cross section along the electric field direction is shown in Fig. 3.12(a), the Fermi surface is shifted opposite to the direction of the electric field (*i.e.* to the right), which results in an imbalance of electrons with right-pointing and left-pointing crystal momentum. The total crystal momentum of the electrons is defined as the sum of all filled electron state momenta: $\mathbf{p}_{\text{xtal}} = \Sigma\ \hbar\mathbf{k}_{e,filled}$. Under the left-pointing electric field shown in Fig. 3.12, there are more filled electron states with momenta pointing to the left than those with momenta pointing to the right, therefore the total crystal momentum is pointing towards the left, even though on average the electrons are moving towards the right (since there are more electrons on the band with right-going velocity $\mathbf{v}(\mathbf{k}) = \frac{1}{\hbar}\nabla_{\mathbf{k}}\mathcal{E}$). If scattering is limited to wavevectors within the first Brillouin zone, one can see that states with larger left-pointing momenta scatter to the right in momentum space with a change in momentum $\hbar\Delta\mathbf{k}$, which results in a momentum transfer to the scatterer $-\hbar\Delta\mathbf{k}$ that points to the left. By the semiclassical equation of motion, $\sum_{\mathbf{k}}\hbar\frac{d\mathbf{k}}{dt} = \mathbf{F}_e$, this change in momentum generates a corresponding force $\mathbf{F}_{scat} = -\mathbf{F}_e$ acting on the scatterer, which also points to the left. An equivalent picture is to consider the charge carriers as positively-charged holes which carry the opposite momentum of empty electron states. The total momentum can be calculated by summing $\mathbf{p} = \Sigma\ \hbar\mathbf{k}_{h,filled} = \Sigma - \hbar\mathbf{k}_{e,empty}$. In this picture, there are more holes with left-pointing momenta than those with right-pointing momenta, thus the total crystal momentum is also pointing to the left. The corresponding total momentum transfer to the scatterer is thus also pointing to the left. Since the direction of the resulting force is in the same direction as the direction of motion for holes, such a force is known as a *hole wind* force.

The hole wind force has been experimentally observed to migrate interstitial atoms such as carbon, nitrogen and hydrogen in metallic wires along the electric current direction.[65,66] In addition, by varying the transition metals used as the host conductor, it has been shown that the direction of electromigration can be switched between electron- and hole-directions as carriers are switched from electrons to holes.[65,66] This shows that the semiclassical model of holes can be useful for explaining electromigration in some cases. However, if scattering wavevectors beyond the first Brillouin zone are allowed, the intuitive scattering picture for the hole wind force quickly breaks down. In order to rigorously justify the electromigration force in the regime where the spatial variation of the potential is comparable to the electron wavelength, a fully quantum mechanical treatment is needed.

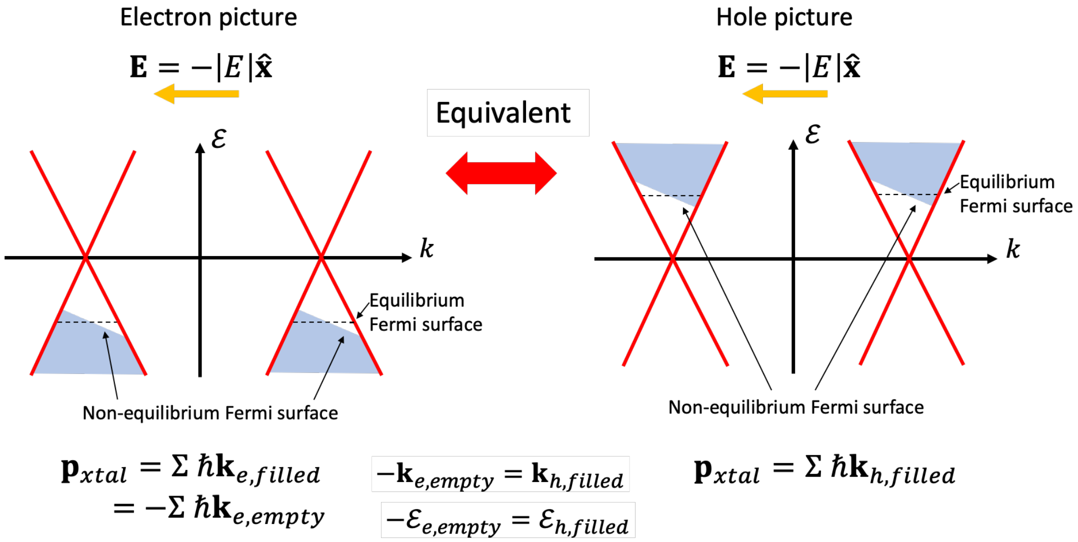

Fig. 3.12 Hole wind arising from imbalance of states with left- and right-pointing momenta. A left-pointing electric field results in a shift of the Fermi surface to the right, which causes an increase of filled -k electron states and a decrease of filled +k electron states. The resulting net momentum points to the left. Upon scattering, this momentum is transferred to the scatterer, which generates a left-pointing force. An equivalent picture is to think of the momentum carried by holes (absence of electrons). There are also more -k hole states than +k hole states, which results in a net momentum pointing to the left.

The inadequacy of the semiclassical model is especially apparent in complex extended scatterers composed of many atoms, such as F_4TCNQ where inter-atomic distances within the molecular scatterers are comparable to the lattice constant of graphene, which means that the scattering potential has strong components at the Brillouin zone boundary. Since the Fermi surface of charge neutral graphene is also near the Brillouin zone boundary, this means that the potential is not varying slowly enough compared to electron wavelengths in graphene, thus strong Umklapp scattering is expected. These processes scatter electron states far outside the first Brillouin zone, resulting in large and complicated momentum changes, thus the semiclassical model cannot be directly applied.

Furthermore, many-body effects complicate evaluation of scattering matrix elements.[63] An important many-body effect to consider in electromigration is the Landauer dipole,[67] which arises from electrons piling up in the material around the scatterer, and which induces screening charges around the scatterer. Because of these effects, it is often more useful to consider the quantum mechanical expectation value of the ion's momentum change $\frac{d\langle \mathbf{P}\rangle}{dt}$ rather than the electron's momentum change (as shown above). The theory of electromigration described in the following section takes this alternative perspective and describes the model presented by Sorbello,[68] as well as the implementation of the wind force calculation by Bevan *et al.* with non-equilibrium Green's function methods.[69,70]

Here we consider the many-body Hamiltonian $\mathcal{H}$ of an adatom-conductor system where the adatom is located at position $\mathbf{R}$, and an external electric field $\mathbf{E}$ is applied to the system. The total Hamiltonian can be written as:

$$\mathcal{H} = \sum_i e\mathbf{r}_i \cdot \mathbf{E} - Ze\mathbf{R} \cdot \mathbf{E} + H_{el-el} + H_{ion-ion} + v_{el-ion} \quad , \tag{3. 117}$$

where $\mathbf{r}_i$ is the position operator of the i-th electron, Z is the valence of the electromigrating adatom, H_{el-el} is the electron-electron interaction Hamiltonian without electron-ion interaction, $H_{ion-ion}$ is the ion-ion interaction Hamiltonian without the electron-ion interaction, and v_{el-ion} is the electron-ion interaction potential. By treating the ion as a very massive classical object (in the spirit of the Born-Oppenheimer approximation) we can make some simplifications. Since ions are now immobile classical objects, the ionic wavefunction is not considered and $\mathbf{R}$ becomes a classical parameter instead of an operator. The basis states of the Hamiltonian are now only eigenstates of the conduction electrons. The quantum mechanical force on the ion given the many-body electron wavefunction can then be expressed using the Ehrenfest theorem as:

$$\begin{aligned} \langle \mathbf{F} \rangle &= \frac{d\langle \mathbf{P} \rangle}{dt} \\ &= \frac{1}{i\hbar}\langle [\mathbf{P}, \mathcal{H}] \rangle \\ &= -\langle \nabla_{\mathbf{R}} \mathcal{H} \rangle \, , \end{aligned} \tag{ 3.118 }$$

where we have used the momentum operator of the ion $\mathbf{P} = -i\hbar\nabla_{\mathbf{R}}$. Applying the momentum operator to the Hamiltonian now yields:

$$\langle \mathbf{F} \rangle = Ze\mathbf{E} - \langle \nabla_{\mathbf{R}} v_{el-ion} \rangle \quad . \tag{ 3.119}$$

The first term may be identified as the "direct force" ($\mathbf{F_D}$) on the electromigrating adatom, which describes the force experienced by the bare adatom ion core when an electric field $\mathbf{E}$ is applied. The second term is identified as the "wind force" ($\mathbf{F_W}$), which describes the force experienced by the adatom due to interaction with the non-equilibrium conduction electron charge density around it.

To evaluate the wind force $\mathbf{F_W}$ in the low-field regime, the Kubo linear-response formalism can be applied to obtain the simple result[71]:

$$\langle \mathbf{F_W} \rangle = -\sum_{\mathbf{k}} [g(\mathbf{k}) - g^0(\mathbf{k})] \langle \psi_{\mathbf{k}} | \nabla_{\mathbf{R}} v(|\mathbf{r} - \mathbf{R}|) | \psi_{\mathbf{k}} \rangle , \tag{3.120}$$

where $g(\mathbf{k}) - g^0(\mathbf{k})$ is the difference between the non-equilibrium and equilibrium electron distribution function as defined in Eq. (3.72) (for brevity v_{el-ion} is represented by v). Converting this expression to the real-space basis yields a readily interpretable result:

$$\langle \mathbf{F_W} \rangle = -\int \delta\rho(\mathbf{r}) \nabla_{\mathbf{R}} v(|\mathbf{r} - \mathbf{R}|) \, d\mathbf{r}. \tag{3.121}$$

The term in the integrand is just the force applied on the induced charge density change $\delta\rho$ by the electric field of the adatom core: $\mathbf{E} = -\nabla_{\mathbf{r}} v = \nabla_{\mathbf{R}} v(|\mathbf{r} - \mathbf{R}|) = \nabla_{\mathbf{R}} \left(-\frac{e}{|\mathbf{r}-\mathbf{R}|} \right) = \frac{e}{|\mathbf{r}-\mathbf{R}|} \, (\mathbf{r} - \mathbf{R})$. The opposite of this force is thus the force applied on the adatom core due to the induced charge density change $\delta\rho$, which is the wind force. Experimentally, the wind force is usually found to be an order of magnitude greater than the direct force, and usually pushes impurities in the direction of electron flow.[23] In order to explain these characteristics of the wind force it is necessary to describe the charge distribution around the scatterer ($\delta\rho(\mathbf{r})$).

Although $\delta\rho$ is complex, anisotropic, and depends on the adatom location with respect to the surface unit cell, it can be qualitatively described by the Landauer model of ballistic transport.[72] In this model incoming electrons are reflected by a scatterer (an impurity) which causes an imbalance in forward and backward going electron distributions. This imbalance in electron distributions is schematically represented in Fig. 3.13. For simplicity we assume the device has ideal ballistic contacts where electrons transmit freely from the contacts to the conductive channel material. The electrochemical potential of electrons (Fermi level) μ_L, μ_R are well-defined in the left and right contacts, respectively. Near the impurity, however, the electron distributions are in a highly non-equilibrium state. To the immediate left of the impurity, right-going electrons with momentum $+k$ arrive from the left contact with perfect transmission. They reflect from the impurity with probability $1 - T$, which then populate the states with momentum $-k$. To the immediate right of the impurity, electrons with momentum $+k$ transmit through the impurity with probability T, populating the right-going states. The left-going states with momentum $-k$ are occupied by electrons coming from the right contact. It can be seen that a sharp drop-off in the quasi-Fermi level (defined as the average of the electrochemical potentials of the $+k$ and $-k$ states) occurs around the impurity. The remainder of the electrochemical potential drop-off occurs at the contacts and corresponds to the contact resistance of $h/2e^2$ of a perfect ballistic channel.

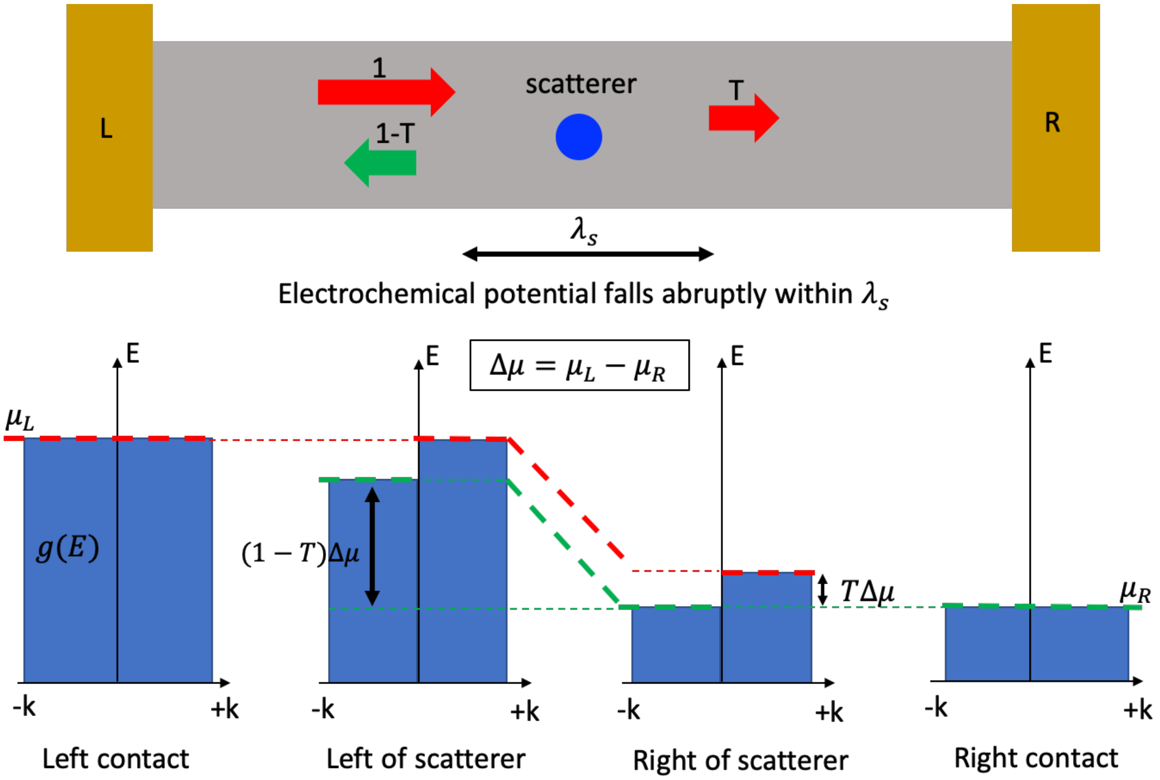

Fig. 3.13 Schematic of electron scattering in the Landauer transport model. Electrons arriving from the left contact transmit with probability T through the scattering impurity and reflect with probability $1 - T$. This causes a highly non-equilibrium distribution function around the impurity and results in a sharp drop-off of the electrochemical potential near the impurity.

While the drop-off in electrochemical potential is abrupt near the impurity, the electrostatic potential follows a much smoother curve due to the finite screening length in the conductor. As a result, the conduction band bottom does not vary congruently with the electrochemical potential, which causes a pileup of charge around the impurity forming a mesoscopic dipole known as the "residual resistivity dipole" (RRD), or the Landauer dipole (shown in Fig. 3.14 (a)). Landauer first analyzed the local transport field generated by a scatterer in his well-known paper in 1957.[67] Landauer found that negative charge accumulates on the upwind side of oncoming electrons, while positive charge accumulates on the downwind side. This produces a dipole field $\mathbf{E}_{dip}$ which accelerates electrons around the scatterer, enabling electrons to traverse the scattering region. Landauer's analysis of microscopic scattering processes provides an important connection to the macroscopic concept of Ohm's law because the RRD establishes the field necessary to define a local resistivity, $\mathbf{E}_{dip}/\mathbf{J} = \rho$. One should note that the direction of the RRD actually *reduces* the magnitude of the overall wind force on a positive impurity ion core. To explain why the positive impurity ion core is pushed along the direction of electron flow, one must additionally consider the local polarization of the scattering impurity. Taking a closer look at bound electrons of the impurity, one finds that they form a dipole opposite to the direction of the RRD, which can be interpreted as a screening response of the valence electrons of the impurity to the RRD. The resulting dipole formed on the impurity itself is much closer to the impurity ion core than the RRD (as indicated by the charges on the adatom itself in Fig. 3.14), and thus exerts a stronger force on the impurity. Since this localized dipole is opposite in direction to the RRD, the net force pushes the impurity in the direction of electron flow. The self-consistently calculated charge density distribution can thus be used to calculate the total wind force.

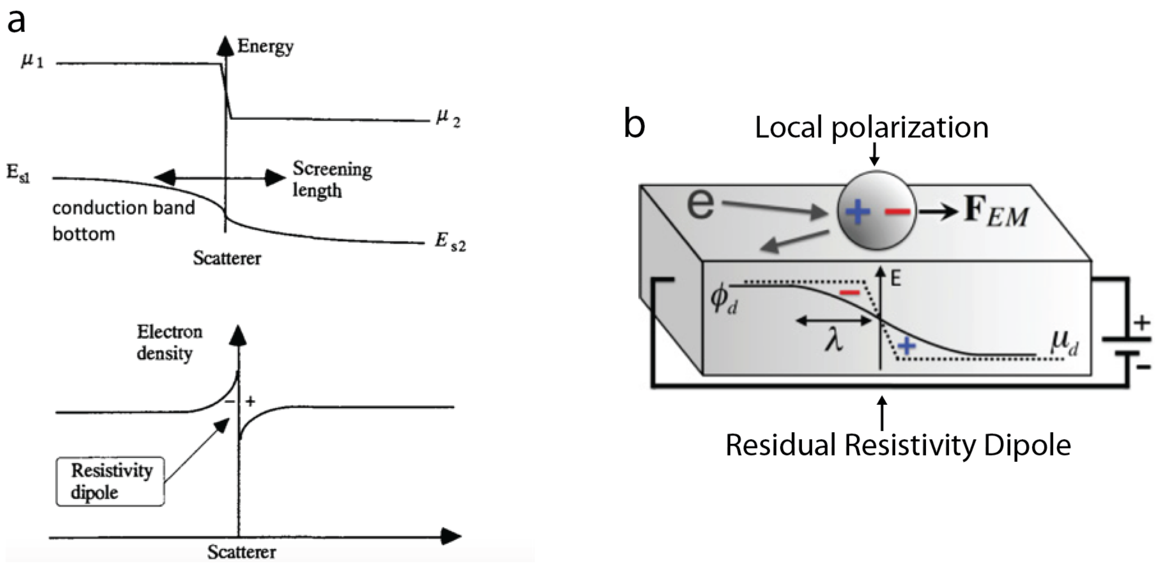

Fig. 3.14 Origin of the Landauer resistivity dipole. (a) Schematic of local variation of the electrochemical potential, conduction band edge (electric potential), and charge accumulation around the residual resistivity dipole. Schematic adapted from [72]. (b) Schematic of the charge distribution surrounding an electromigrating adatom. The RRD exists mainly in the conductive substrate, while bound electrons *in the adatom* form an opposite local dipole. Figure adapted from [69].

3.4.3 Non-equilibrium Green's Function (NEGF) Calculations in Electromigration

The charge distribution around a scatterer during electromigration can be extremely complex and depends on the specific position of the scatterer on the conducting material, as well as electronic structure of the conducting material and scatterer itself. In addition, while conventional DFT methods are useful for treating finite or periodic systems, real devices are open systems where electrons are exchanged with semi-infinite leads with well-defined electrochemical potentials. Consequently, in order to calculate the charge distribution under current flow, NEGF methods are often used. The two-contact configuration of NEGF presented here is described by Datta[72] and used in Bevan's treatment of the electromigration force.[70]

To introduce the NEGF method, we start by writing down the retarded Green's function for a known Hamiltonian H of a finite system in the basis of a set of orthogonal atomic orbitals:

$$G = [(E + i\alpha)S - H]^{-1}\,, \tag{3.122}$$

where S is the overlap matrix between atomic basis functions. Now suppose the system were contacted by one infinite lead, where orbital p_i in the lead p is connected to orbital i in the conductor C. The Green's function can now be broken down into submatrices representing the contact and the material:

$$\begin{bmatrix} G_p & G_{pC} \\ G_{Cp} & G_C \end{bmatrix} = \begin{bmatrix} (E + i\alpha)S_p - H_p & \tau_p \\ \tau_p^\dagger & (E + i\alpha)S_C - H_C \end{bmatrix}^{-1} , \tag{ 3.123}$$

where H_p is the Hamiltonian of the lead, H_C is the Hamiltonian of the conductor, and S_p, S_C are the overlap matrix between atomic basis functions in the lead and conductor, respectively. τ_p is the coupling matrix between orbitals in the lead and orbitals in the conductor (which is only non-zero for adjacent pairs (p_i, i)). Since there are an infinite number of orbitals in the lead, (3.123) is an infinite dimensional matrix. However, we really only care about states within the finite conductor, so we would like to obtain the finite dimensional Green's function G_C. To do this, we multiply the left and right hand side of (3.123) to obtain the identity matrix, which yields two equations:

$$\left[(E + i\alpha)S_P - H_p\right]G_{pC} + \tau_p G_C = 0\,, \tag{3.124}$$

And

$$[(E + i\alpha)S_C - H_C]G_C + \tau_p^\dagger G_{pC} = I\,. \tag{3.125}$$

Solving for G_C, we obtain the expression

$$G_C = \left[(E + i\alpha)S_C - H_C - \tau_p^\dagger g_p^R \tau_p\right]^{-1} , \tag{3.126}$$

where $g_p^R = \left[(E + i\alpha)S_p - H_p\right]^{-1}$. Since τ_p is only non-zero for orbitals adjacent to each other at the interface between the contact and the conductor, the element $\left[\tau_p^\dagger g_p^R \tau_p\right]_{ij} = t^2 g_p^R\left(p_i, p_j\right) = \Sigma_p(i, j)$, where Σ_p is defined as the self-energy of contact p. The Green's function for an isolated lead g_p^R can be solved analytically, thus reducing an infinite-dimensional matrix inversion problem to a finite one. The resulting Green's function for the conductor with left and right contacts is thus

$$G = [(E + i\alpha)S_C - H_C - \Sigma_L - \Sigma_R]^{-1}\,, \tag{3.127}$$

where the DFT time-independent electronic Hamiltonian of the conductor H_C can be written explicitly as

$$H_C = -\frac{1}{2}\nabla^2 + V_{nl}^{ps} + V^{NA} + \delta V^H + V^{XC}\,, \tag{3.128}$$

where V_{nl}^{ps} is the non-local pseudopotential term, V^{NA} is the sum of all screened neutral atom potentials, δV^{H} is the self-consistent Hartree term, and V^{XC} is the exchange-correlation term.[70] The obtained Green's function can then be used to calculate the charge density through

$$\begin{aligned}\Delta\rho &= \Delta\rho_L + \Delta\rho_R \\ &= \sum_{k,s}\left|\psi_{k,s}^{(L)}\right|^2\left(f_L - f_{eq}\right) + \left|\psi_{k,s}^{(R)}\right|^2\left(f_R - f_{eq}\right) \\ &= \int_{-\infty}^{\infty}\{G\Gamma_{\mathrm{L}}G^{\dagger}\left(f_L - f_{eq}\right) - G\Gamma_{\mathrm{R}}G^{\dagger}\left(f_R - f_{eq}\right)\}\frac{dE}{\pi},\end{aligned} \qquad (3.129)$$

where $\Delta\rho_L$ and $\Delta\rho_R$ represent the non-equilibrium charge density induced by scattering, which can be expressed as a sum of the density of states coming from the L or R electrodes $|\psi_{k,s}^{(L,R)}|^2$ multiplied by their occupation $f_{L,R} = 1/(1 + e^{(E-\mu_{L,R})/k_B T})$ relative to the equilibrium occupation f_{eq}. Here $\mu_{L,R}$ refers to the electrochemical potential of the left and right electrodes, which are set unequal under non-equilibrium conditions. We then define $\Gamma_{\mathrm{L,R}} = i(\Sigma_{\mathrm{L,R}} - \Sigma_{\mathrm{L,R}}{}^{\dagger})$, which enables us to express the density of state in terms of the spectral function as $|\psi_{k,s}^{(L,R)}|^2 = \frac{1}{2\pi}A^{(L,R)} = \frac{1}{2\pi}G\Gamma_{\mathrm{L,R}}G^{\dagger}$. Accounting for the spin degeneracy, this yields the final expression in (3.129). Therefore, by evaluating the Green's function, we can obtain the current-induced charge distribution $\Delta\rho$, which allows us to calculate the wind force by (3.121).

3.4.4 Experimental Measurement of Electromigration Force

Although the electromigration force has been estimated for mesoscopic objects in a variety of conducting systems, including metal clusters on carbon nanotubes,[62] silver islands on silver thin films,[23] and metal clusters on graphene[73], electromigration of single isolated adsorbates has never been resolved at the atomic scale. The results presented in chapter 8 are the first studies of single-molecule resolved electromigration. By using F_4TCNQ molecules deposited on a graphene FET at T=4K, we are able to track electromigration of single molecules as electric current pushes them across the surface.

In most existing experimental studies, the electromigrating object is found to move along the direction of electron flow, with the wind force estimated to be typically 10~1000 greater in magnitude than the direct force.[23] In the literature of experimental electromigration studies, a quantity known as the effective valence Z^* is often used to characterize the total electromigration force, where Z^* is defined as

$$Z^* = \frac{F_{total}}{eE}\ , \qquad (3.130)$$

where F_{total} is the total electromigration force, e is the electron charge, and E is the local in-plane electric field which drives the electromigration. In other words, Z^* describes the response of an electromigrating object moving in an in-plane electric field as if it were an object carrying charge Z^*e. Since the direct force is just $\mathbf{F}_D = Ze\mathbf{E}$ and the total force is the sum of direct and wind forces, $Z^* e\mathbf{E} = \mathbf{F}_D + \mathbf{F}_W$, the wind force can then be expressed as $\mathbf{F}_W = (Z^* - Z)e\mathbf{E}$. The ratio of wind to direct force is then $\frac{\mathbf{F}_W}{\mathbf{F}_D} = Z^*/Z - 1$. Since the wind force is typically several orders of magnitude larger than the direct force, $|Z^*|$ is also typically much larger than $|Z|$.

To estimate the total force F_{total}, we make use of the Einstein relation to relate the mobility μ (and F_{total}) to the diffusion constant D

$$\mu = \frac{v_d}{F_{total}} = \frac{D}{k_b T}, \tag{3.131}$$

where v_d is the drift velocity of the migrating object, and T is the temperature, thus by measuring the average drift velocity and diffusion constants of adsorbed molecules across the conductor, one can measure the total electromigration force ($F_{total} = kTv_d/D$). Using the average in-plane electric field measured by scanning tunneling potentiometry during current flow, one can then estimate the effective valence Z^* ($F_{total} = Z^* eE$), and thus infer the value of the wind force ($F_W = (Z^* - Z)eE$).

4 Gate-tunable Molecular Concentration on a Graphene FET

In surface science adsorbates such as alkali atoms and molecules are commonly deposited onto surfaces in vacuum to induce chemical doping through charge transfer. However, once deposited, the spatial arrangement of adsorbates cannot be reversibly tuned because there is typically a large energy difference between donor/acceptor levels and the Fermi level of the substrate, which causes permanent charge transfer and stabilizes the surface adsorbate configuration.

In this chapter I will discuss a system where molecular orbital levels are close enough in energy to the substrate Fermi level for electrostatic gating to change the molecular charge state. Application of an external out-of-plane electric field causes molecules to become charged and change their surface concentration in response to the external field. This process is imaged on a gate-tunable graphene field-effect transistor (FET) using STM. The gate-tunable molecular concentration is explained by a dynamical molecular rearrangement process that reduces total electronic energy by maintaining Fermi level pinning in the device substrate. The molecular surface concentration is fully determined by the device back-gate voltage, its geometric capacitance, and the energy difference between the graphene Dirac point and the molecular LUMO level. The content here is based on our published paper: F. Liou *et al.*, "Imaging Reconfigurable Molecular Concentration on a Graphene Field-Effect Transistor", *Nano Lett.* **21**, 20, 8770–8776 (2021).[34]

4.1 Introduction

One important way in which adsorbates modify surfaces is by inducing localized electronic defect states that trap electrons and cause Fermi level pinning.[74–77] Typically, Fermi level pinning is considered a "one-way" process where defects may change the location of electrons (i.e., by trapping them) but electrons do not change the location of defects. Here we reverse this idea by implementing a condensed matter system where defect concentration can be continuously and reversibly tuned by adding or removing electrons from the system. We observe this unique behavior for F_4TCNQ molecules adsorbed onto the surface of a graphene field-effect transistor (FET). When a voltage is applied to the back-gate of such a device under proper conditions then the resulting electric field is not screened by the graphene Dirac band electrons, but is rather unexpectedly screened by ionized molecules that mechanically rearrange themselves on the device surface. The devices in which this occurs are not electrochemical cells[17,78,79] attached to some external reservoir of material. Instead they are composed of ultraclean monolayers of graphene on hBN that are dosed with a submonolayer molecular coverage and then held at cryogenic temperature in ultrahigh vacuum (UHV). The adsorbate rearrangement process observed on our devices arises from a physical mechanism whereby adsorbate-induced Fermi level pinning helps to minimize graphene Dirac band electronic energy. The energetics of Fermi level pinning in this 2D system is so strongly tied to the adsorbate arrangement that it allows reversible, mechanical alteration of the surface defect concentration by adding or removing electrons using the FET back-gate.

This behavior arises due to the proximity in energy of the F_4TCNQ lowest unoccupied molecular orbital (LUMO) to the graphene Dirac point.[26,80–83] The resulting high electron affinity of F_4TCNQ on graphene has been exploited previously to p-dope graphene.[84,85] STM measurements have also shown that charge flows easily into and out of F_4TCNQ molecules on graphene.[5,26,81,86] No previous studies, however, have demonstrated reversible control over the geometric arrangement of F_4TCNQ adsorbates on graphene.

The strategy here will be to first explain the experimental procedure by which we control the surface concentration of F_4TCNQ molecules on a graphene FET via electrical signals sent to the device. This technique has enabled us to discover that the F_4TCNQ surface concentration on graphene FETs varies linearly with applied gate voltage. We have characterized this unexpected behavior by performing STM spectroscopy on molecule-decorated graphene devices for different molecular coverages. These measurements allow us to establish a connection between gate-dependent molecular surface concentration and Fermi level pinning in graphene FETs. We have distilled these observations into a simple theoretical model that connects the energetics of graphene electrons to the geometric arrangement of surface adsorbates, and which allows us to predict molecular surface concentration for any given back-gate voltage. The connection established here between molecular electronic structure and molecular surface concentration provides a new technique for quantitatively determining molecular energy levels by simply counting the number of molecules on a clean graphene surface.

4.2 Methods

Our technique for reversibly changing molecular concentration on graphene devices starts with the deposition of a submonolayer coverage of F_4TCNQ molecules onto a clean graphene/hBN FET held at room temperature in UHV. We then cool the molecule-decorated device down to 4.5 K without breaking vacuum, at which point the molecules can be stably imaged by our STM. In order to set the molecular surface concentration to a desired value, a set-voltage (V_{G-set}) is applied to the device back-gate while a source-drain current (I_{SD}) is *simultaneously* passed through the graphene as sketched in Fig. 4.1 (I_{SD} provides thermal energy to facilitate molecular diffusion). The molecules freeze in place as soon as I_{SD} is set to zero, resulting in a well-defined and reversible surface concentration that is determined by V_{G-set}. After the molecules are frozen in place, the gate voltage is set to zero for STM imaging.

4.3 Results

The resulting control over molecular surface concentration can be seen in the differently prepared molecular concentrations shown in Fig. 4.2 (a)-(f) (all measured at the same spot on the surface). At a high set-voltage of V_{G-set}= 60 V the resulting molecular surface concentration is correspondingly high (n_M = 6 x 10^{12} cm^{-2}) and the roughly evenly-spaced molecular distribution suggests that the molecules are charged during the surface concentration-setting process and repel each other (Fig. 4.2 (a)). As V_{G-set} is reduced, the resulting molecular concentration correspondingly reduces (Fig. 4.2 (b)-(f)). A plot of molecule surface concentration vs. V_{G-set} (Fig. 4.2 (g)) shows that the molecular concentration is almost perfectly linear over the gate-voltage range -10 V < V_{G-set} < 60 V and remains nearly zero for V_{G-set}< -10 V. The gate-tunable molecular concentration is observed to be non-hysteretic since the forward sweep and backward sweep data lie almost perfectly on top of each other. The molecular concentration within our STM field of view is thus precisely and reversibly controlled by tuning the graphene FET electrical device parameters.

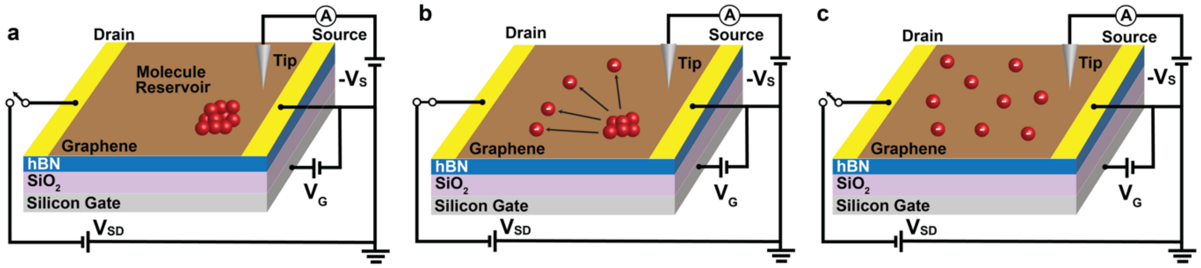

Fig. 4.1 Controlling molecular concentration on a graphene field-effect transistor (a) Sketch representing the F_4TCNQ molecular configuration (red balls) in the "as grown" state after thermal evaporation onto a graphene FET. A representative circuit shows the biases applied to the device. (b) Application of a back-gate voltage, V_{G-set}, to the FET while simultaneously flowing a source-drain current I_{SD} through the graphene causes the molecules to diffuse out onto the graphene surface. Typical values of V_{G-set} range from -60 V to 60 V. Typical values of V_{SD} used for changing the molecular concentration range from 2V to 6V, and typical I_{SD} values range from 0.5 mA to 2 mA. (c) When the source-drain current is turned off the device cools and the molecules freeze in place. The gate voltage V_G is then returned to 0 V and a sample bias (relative to the tip) of V_S = 2 V with current setpoint of 2 pA can then be used for stably scanning the molecules.

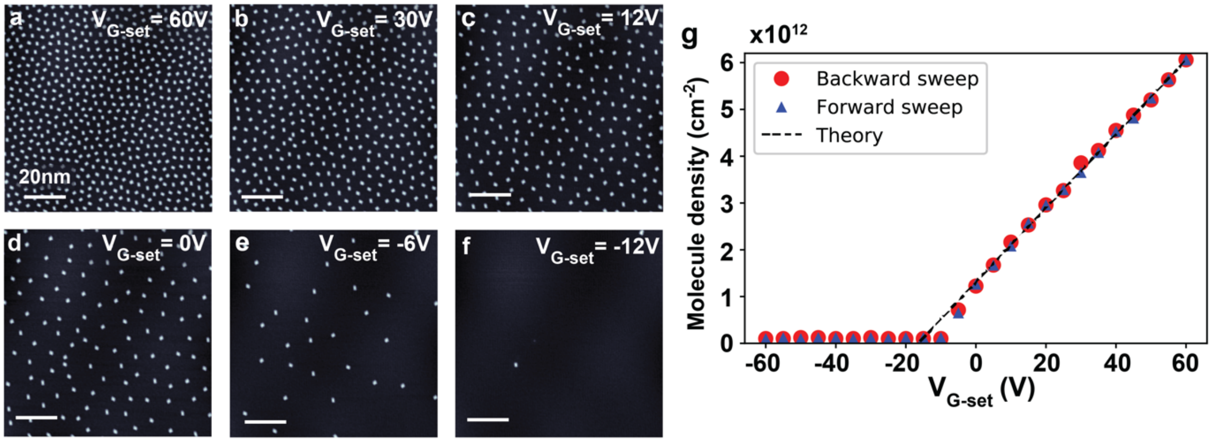

Fig. 4.2 Tuning molecular concentration by using FET gate voltage (a)-(f) STM topographs of the same area on the surface of a graphene field-effect transistor after tuning the molecular surface concentration with different values of gate set-voltage over the range -12 V $< V_{G-set} <$ 60 V. (g) Measured molecular concentration as a function of V_{G-set}. No hysteresis is observed for forward and backward sweeps. The dashed line shows a theoretical fit to the data using Eq. (4.5).

The molecular concentration across the entire device surface, however, cannot be completely uniform since the molecules have to *go somewhere* when their concentration is reduced and *come back from somewhere* when their concentration is increased, and this "somewhere" cannot have the same concentration as the STM field of view seen in Fig. 4.2. However, the process described above for setting the molecular surface concentration is surprisingly robust and can be observed over a majority of the surface area that we have scanned (~80 %) on multiple devices. This observation suggests that there are regions of the surface act as *local reservoirs* that store F_4TCNQ molecules in a compact, condensed phase, as will later be shown in the chapter 5. F_4TCNQ molecules must flow in and out of these condensation regions (due to electrostatic potential inhomogeneities) to enable the precise concentration control that we observe over a large majority of the surface.

The fact that we observe no significant decrease in molecule concentration over multiple cycles of density changing operations suggests that the molecular storage and release process is fully reversible. To explain why molecules aggregate in a condensed phase we hypothesize that a highly negative gate voltage draws electrons out of the device and thus removes charge from the molecules. This reduces repulsive Coulomb interactions between them, thereby causing attractive intermolecular forces (such as van der Waals) to become more dominant. Weak molecule-substrate interactions allow the molecules to diffuse easily to defective regions where they can be captured.

In order to understand the microscopic mechanism that underlies the process of tuning molecular surface concentration we must understand how charge readjusts itself in a graphene device decorated by mobile, charge-tunable molecules as the gate voltage is changed. Here the molecule-decorated graphene forms one side of a capacitor while the back-gate electrode forms the other, and so the total charge that flows to the molecule/graphene system can be determined straightforwardly from the device capacitance and applied gate-voltage ($Q_T = -V_{G-set} C_T$). Electrons transferred to the graphene side of the capacitor can either occupy graphene Dirac fermion band states or, alternatively, the LUMO states of the adsorbed molecules. To clarify how charge is distributed between these two choices we performed STM spectroscopy directly on adsorbed F_4TCNQ molecules as well as on bare graphene patches between the molecules for different applied gate-voltages and different molecular concentrations. This enabled us to track the energetic alignment of the F_4TCNQ LUMO energy (E_L) and the graphene Dirac point energy (E_D) with respect to the graphene Fermi level (E_F), thus providing snapshots of how charge in the device is distributed under different conditions. Our observations in this regard provide the basis for a simple model that quantitatively predicts gate-tunable molecular surface concentration.

We first describe the negative gate-voltage regime, $V_G < -10$ V, where the electronic configuration of the molecule/graphene system is qualitatively represented by the sketch in the inset to Fig. 4.3 (c). Here the graphene is p-doped since E_F lies below E_D. The molecular LUMO level, E_L, lies below E_D but remains unfilled by electrons since it is still higher than E_F. Experimental evidence for this type of electronic behavior is seen in the "on-molecule" and "off-molecule" dI/dV_S spectra of Fig. 4.3 (a) and (b), where V_S is the sample bias of the tunnel junction (all dI/dV_S spectra shown in Fig. 4.3 were acquired after "freezing" the molecules by setting I_{SD} to zero -- spectroscopy was never acquired under "diffusive" conditions where $I_{SD} \neq 0$). Molecular spectra are only shown for $V_S > 0$ since negative V_S induced tip electric fields that caused the molecules to charge and adsorb onto the tip. The top curve in Fig. 4.3 (a) shows an on-molecule dI/dV_S spectrum measured with the STM tip held above the center of an F_4TCNQ molecule for a gate-voltage of $V_G = -60$ V and a fixed molecular surface concentration of $n_M = 0.8 \times 10^{12}$ cm^{-2} (see inset). The F_4TCNQ LUMO level (arrow) sits at a sample bias of $V_S \approx 0.2$ V above the Fermi energy (which is at $V_S = 0$). The precise energy position of the LUMO is determined following the protocol of ref. [26] after accounting for known inelastic tunneling effects.[26,87,88] We note that the each LUMO arrow is shifted slightly to the left of the spectrum maximum due to a 35 meV phonon mode (found by fitting high-resolution STS measurements as described in ref.[26]) that broadens the LUMO peak[26] and results in the LUMO energy being lower than the apparent maximum by ~35 meV. A previously reported satellite peak due to a 183 meV phonon mode is also visible at $V_S \approx 0.4$ V.[26]

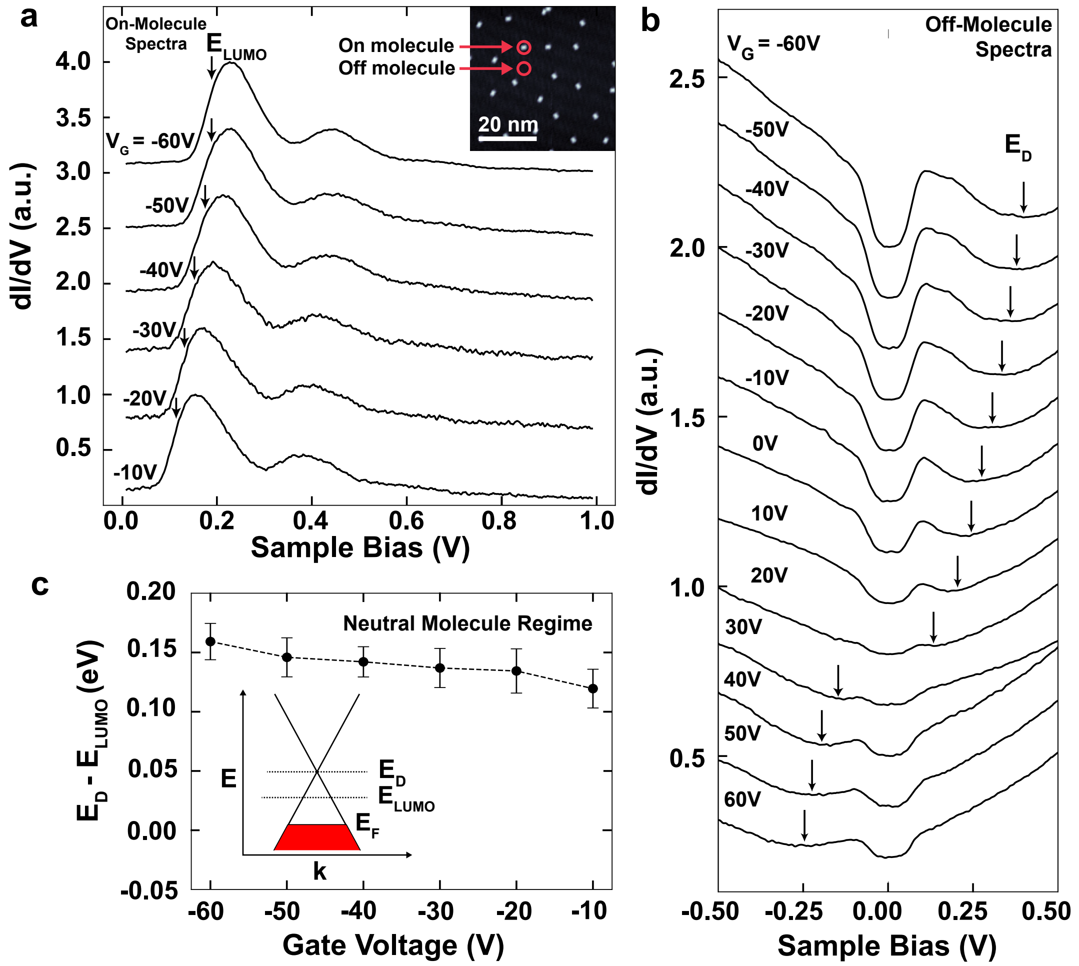

Fig. 4.3 STM spectroscopy of F$_4$TCNQ-decorated graphene field-effect transistor (a) dI/dV_S spectra measured while holding the STM tip directly above an F$_4$TCNQ molecule for a molecular concentration of 0.8 x 10^{12} cm^{-2} at the surface of a graphene FET (-60 V < V_G < -10 V). Energy location of the lowest unoccupied molecular orbital (E_L) is marked. Inset shows a representative image of the surface at this molecular concentration. (b) dI/dV_S spectra measured while holding the STM tip over bare patches of graphene ~100 Å away from nearby F$_4$TCNQ molecules for the same surface conditions measured in (a) (-60 V < V_G < 60 V, n_M = 0.8 x 10^{12} cm^{-2}). Graphene Dirac point energy (E_D) is marked. Spectroscopy parameters: $I_{setpoint}$ = 50 pA, $V_{setpoint}$ = 1 V on graphene, $I_{setpoint}$ = 10 pA, $V_{setpoint}$ = 1 V on molecule. (c) Gate-voltage dependence of the Dirac point energy relative to the molecular LUMO energy ($E_D - E_L$) for molecular concentration n_M = 0.8 x 10^{12} cm^{-2} . Inset shows a simplified representation of the electronic structure of F$_4$TCNQ molecules on graphene for large negative gate voltages (E_F = Fermi energy).

The top curve in Fig. 4.3 (b) shows an off-molecule dI/dV_S spectrum taken with the STM tip held over a bare patch of graphene ~100 Å away from any F_4TCNQ molecules for the same gate-voltage and molecular concentration used for the top curve of Fig. 4.3 (a). A depression in dI/dV_S over the range -60 mV < V_S < 60 mV can be seen that is known to occur due to phonon inelastic tunneling effects,[89] while another depression is seen at $V_S \approx 0.35$ V that marks the location of the graphene Dirac point (E_D).[89,90] The precise value of E_D is found by fitting the dI/dV_S spectra using the protocol outlined in Appendix B. The Dirac point is seen to fall in energy as the gate voltage is increased, causing the graphene to transition from being hole-doped ($E_D > E_F$) to being electron-doped ($E_D < E_F$) at $V_G \approx 20$ V for this molecular surface concentration ($n_M = 0.8 \times 10^{12}$ cm^{-2}). E_D (from Fig. 4.3 (b)) is observed to lie above E_L (from Fig. 4.3 (a)) by ~150 mV for negative gate voltages, and both quantities shift downward in energy together as the gate voltage is increased from V_G = -60 V to -10 V (Fig. 4.3 (c)). Such behavior is expected as E_F "rises" with increased gate voltage in the band structure shown in the inset to Fig. 4.3 (c).

When V_G is raised above -10 V the molecules become charged, causing them to enter a new physical regime. The transition toward this regime can be seen in the gate-dependence of E_L, which falls towards E_F with increasing V_G in Fig. 4.3 (a). Another signature that the molecules become charged (i.e., that the LUMO becomes filled) is that they become mechanically unstable during STS measurement when V_G is raised above -10V. Negatively charged molecules are observed to escape from under the STM tip during spectroscopy measurements, making it impossible to obtain reproducible "on-molecule" spectroscopy for $V_G >$ -10 V. Interestingly, this critical gate-voltage value coincides with the V_{G-set} value at which the molecular concentration begins to rise from near zero (for increasing V_{G-set}), showing that the appearance of molecules on the device surface is correlated with their charge state. Another indication of charged molecular behavior is the spatially uniform intermolecular separation, a signature of intermolecular repulsion.

4.4 Discussion

In order to better understand the charged molecular regime we investigated how changing the molecular surface concentration affects the way electrons fill up graphene states during electrostatic gating. This was accomplished by inspecting the gate-dependence of E_D for different fixed molecular concentrations. Such measurements reveal charge transfer to F_4TCNQ LUMO levels and how this leads to Fermi-level pinning. To see this, we first set the molecular concentration to a desired value (as shown in Fig. 4.5 (a)) and then measured the gate-voltage dependence of E_D (Fig. 4.5 (b)) using off-molecule dI/dV_S spectra via the procedure described above for Fig. 4.3 (b). For a pristine graphene capacitor, E_D is expected to move smoothly down in energy with increasing V_G according to the well-known expression[89]:

$$E_D(V_G) = -sgn(V_G)\hbar v_F\sqrt{\pi C|V_G - V_0|} \qquad (4.1)$$

where $v_F = 1.1 \times 10^6$ m/s is the electron Fermi velocity in graphene, C is the unit area capacitance of the device and V_0 reflects background doping. By fitting Eq. (4.1) to the gate-dependent Dirac point energy of our device before depositing molecules we are able to extract the capacitance between the graphene and the back-gate electrode: $C = (7.8 \pm 0.2) \times 10^{10} cm^{-2}V^{-1}$ (Fig. 4.4).

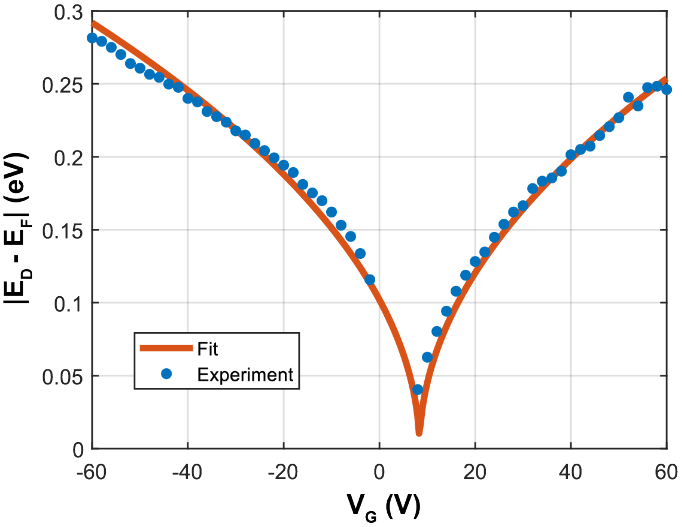

Fig. 4.4 Gate-dependence of the graphene Dirac point energy before molecule deposition. The absolute value of the Dirac point energy relative to the Fermi level is plotted as a function of gate voltage for our pristine graphene device and shows good agreement with Eq. (4.1). A capacitance of $(7.8 \pm 0.2) \times 10^{10} cm^{-2} V^{-1}$ is extracted from the fit.

For nonzero molecular concentrations, however, the E_D vs. V_G curve deviates from Eq. (4.1) and forms a “pinning” plateau at ~140 meV above E_F, with the width of the plateau increasing with increased molecular surface surface concentration (Fig. 4.5 (b)). The start of the plateau (for increasing V_G) coincides with the gate voltage value where the molecular LUMO begins to fall under E_F, thus allowing us to associate the plateau with the charging of F_4TCNQ molecules. The value of E_D at the plateau (~140 meV above E_F) is very close to the energy difference observed between E_D and E_L in Fig. 4.3 (c), providing evidence that the Fermi level is pinned to the molecular LUMO level 140 meV below E_D. This interpretation is quantitatively supported by the increased width of the pinned region (in V_G) as molecular concentration is increased (i.e., since higher molecular concentrations can store more charge). For example, the E_D plateau at a fixed molecular concentration of 4.3 x 10^{12} cm^{-2} has a width of ΔV_G = 50 ± 5 V, which corresponds to a surface charge density of $\Delta\sigma$ = (3.9 ± 0.4) x 10^{12} e^-/cm^2 that reasonably matches the molecular concentration (charge is calculated using the capacitance value acquired via Eq. (4.1)).

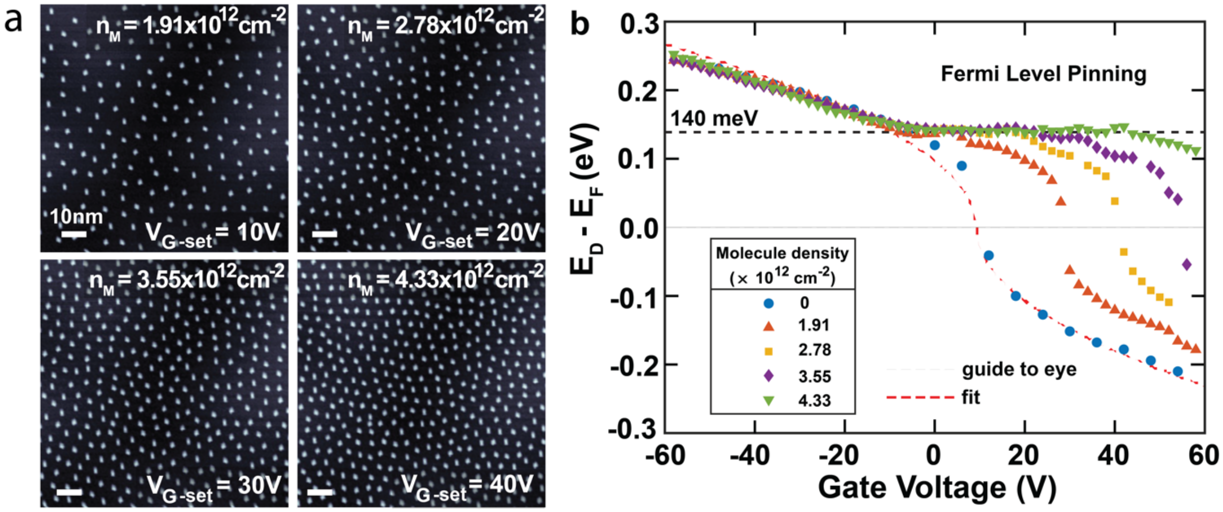

Fig. 4.5 Fermi level pinning of F4TCNQ-doped graphene field-effect transistor. (a) STM images of graphene FET surface decorated with different molecular densities for measurement of molecule-induced Fermi-level pinning shown in (b). (b) Gate-voltage dependence of Dirac point energy (E_D) measured via STS on graphene FET surface for the different molecular densities shown in (a). A concentration-dependent plateau in E_D indicates Fermi level pinning. Red dashed line shows fit of Eq. (4.1) to data for zero molecular concentration ($n_M = 0$).

The Fermi level pinning described above for the *static* molecular configurations of Fig. 4.5 is intimately related to the *dynamic* molecular reconfigurations that enable molecular concentration to be continuously tuned by gate voltage, the central focus of this paper. When the graphene Fermi level is securely pinned by molecular LUMO states, new electrons added to the device (e.g., by an increase in V_G) do not cause the Fermi level to rise in energy since LUMO levels absorb any new charge added to the graphene at E_F. On the other hand, if there are not enough molecules on the surface to pin the Fermi level, then increasing the gate voltage causes electrons to occupy graphene band states at energies *higher* than E_L. This is the origin (from an energetic perspective) of the force that drives the molecules to *move* on the surface in order to dynamically change the molecular concentration when V_{G-set} is modified under "diffusive conditions" (i.e., when $I_{SD} \neq 0$). When V_{G-set} is increased under diffusive conditions then the molecular concentration must also increase to *maintain* Fermi level pinning (the overall lowest energy state) so as to enable charge to flow into lower-energy LUMO levels rather than higher-energy Dirac band states.

These concepts allow us to formulate a simple model for predicting the expected concentration of molecules on the graphene surface for a given gate voltage. We start with the assumption that the lowest-energy electronic configuration under diffusive conditions (and when -10 V < V_G) occurs when the Fermi energy is pinned at E_L. For a given value of V_{G-set} the total charge density on the molecule-decorated FET surface ($\sigma_T = -CV_{G-set}$) will have contributions both from charge carried by the molecules (σ_M) and charge carried by the graphene Dirac band (σ_G):

$$-CV_{G-set} = \sigma_M + \sigma_G\ . \qquad (\ 4.2\ )$$

If each charged molecule contains one electron in its LUMO state (assuming that double occupancy is forbidden due to the large Hubbard energy of the LUMO state[26]) then the total molecular charge is $\sigma_M = -n_M$ where n_M is the surface concentration of molecules and σ_M has units of $|e|$. Eq. (4.2) then leads to the following expression for n_M:

$$n_M = CV_{G-set} + \sigma_G \ . \qquad (4.3)$$

Because E_F is pinned at E_L by the molecular coverage, and $E_L - E_D < 0$, σ_G can be found by integrating the density of states in the graphene band from the Dirac point to E_L, resulting in the following well-known expression:[39]

$$\sigma_G = \frac{|E_D - E_L|^2}{\pi\hbar^2 v_F^2} \qquad (4.4)$$

Combining Eqs. (4.3) and (4.4) leads to the final expression for molecular concentration as a function of V_{G-set}:

$$n_M = CV_{G-set} + \frac{|E_D - E_L|^2}{\pi\hbar^2 v_F^2} \qquad (4.5)$$

Using v_F = 1.1 x 10^6 m/s, we are able to fit Eq. (4.5) to the n_M vs. V_{G-set} data of Fig. 4.2 (g) by using $|E_D - E_L|$ and C as fitting parameters. Eq. (4.5) fits the data well for a value of $|E_D - E_L|$ = 142 ± 23 meV and a value of $C = (7.9 \pm 0.6) \times 10^{10} cm^{-2}V^{-1}$. This value of capacitance agrees well with our independently determined device capacitance of $C = (7.8 \pm 0.2) \times 10^{10} cm^{-2}V^{-1}$. A consequence of the good agreement between these capacitance values is confirmation that each F_4TCNQ molecule carries a single electron of charge, since every additional electron accumulated by increasing the gate voltage corresponds to an additional molecule.

We can further check the validity of this conceptual framework by comparing the value of $E_D - E_L$ obtained from our molecular concentration measurements with the value obtained independently from the STS measurements shown in Fig. 4.3 and Fig. 4.5. STS enables us to obtain $E_D - E_L$ in two ways: first by extracting E_L and E_D directly from the dI/dV_S spectra in Fig. 4.3 (a) and Fig. 4.3 (b) and subtracting them, and second from the E_D energy plateau caused by Fermi level pinning in Fig. 4.5. Using the first method we see from Fig. 4.3 that for V_G = -30V our on-molecule dI/dV_S spectrum yields E_L = 165 meV while our off-molecule spectrum yields E_D = 305 meV. This results in a value of $E_D - E_L$ = 140 ± 20 meV (the average value over the gate-voltage range -60 V < V_G < -10 V is $E_D - E_L$ = 143 ± 9 meV which remains quite close to this value). Using the second method, the Fermi-level pinning data of Fig. 4.5 reveals a Dirac point plateau at $E_D - E_F$ = 140 meV ± 5 meV. Since E_F is pinned at E_L under these conditions, this reflects a value of $E_D - E_L$ = 140 meV ± 5 meV. Both methods are in agreement with the value $|E_D - E_L|$ = 142 ± 23 meV obtained from the concentration-based analysis of Eq. (4.5), and thus support the overall physical picture that we have presented.

One consequence of this analysis is that measurement of molecular concentration on a graphene FET is shown to provide a new method for quantitatively determining the energy of molecular frontier orbitals with respect to the graphene Dirac point (i.e., $E_D - E_L$). This new method is potentially valuable for determining the energy alignment of highly mobile adsorbates since it can be extremely difficult to prevent them from moving when they are under an STM tip during the bias sweeps required for STS (characterizing small devices can also be quite challenging for X-ray-based probes). In our previous work, for example, we found it necessary to anchor F_4TCNQ molecules to a secondary immobile molecular template in order to probe their LUMO levels in the charged state via STS.[26] Such molecular templating, however, can alter local dielectric environments and influence molecular orbital energies.[91,92] Our new technique of measuring gate-dependent molecular concentrations allows one to bypass templating and to access molecular energy-level information via a completely different method.

4.5 Conclusion

In conclusion, we have demonstrated that molecular concentration at the surface of a graphene FET can be continuously and reversibly manipulated via a back-gate voltage applied simultaneously with source-drain current. The equilibrium molecular concentration is precisely determined by the capacitance between the back-gate electrode and the graphene, in combination with the energy difference between the Dirac point and the molecular LUMO level. The driving force behind this dynamic mechanical reconfiguration of molecular concentration is the energetic favorability of molecular Fermi-level pinning compared to filling the graphene Dirac bands. The energy alignment of the molecular LUMO level obtained from a concentration-based analysis using these concepts compares well with the value determined from STS.

5 Gate-tunable Molecular Phase Transitions on a Graphene FET

Solid-liquid phase transitions are fundamental physical processes, but atomically-resolved microscopy has yet to capture both the solid *and* liquid dynamics for such a transition. In this chapter, I present a new technique for controlling the melting and freezing of 2D molecular layers on a graphene field-effect transistor (FET) that enables imaging of phase transition dynamics via atomically-resolved scanning tunneling microscopy. Back-gate voltages applied to a F_4TCNQ-decorated graphene FET induce reversible transitions between a charge-neutral solid phase and a negatively charged liquid phase. Nonequilibrium molecular melting dynamics are visualized by rapidly heating the graphene surface with electrical current and imaging the resulting evolution toward new equilibrium states. An analytical model has been developed that explains the observed equilibrium mixed-state phases based on spectroscopic measurement of both solid and liquid molecular energy levels. Observed non-equilibrium melting dynamics are consistent with Monte Carlo simulations.

5.1 Introduction

Phase transitions reflect the collective thermodynamic behavior of large numbers of particles, but they fundamentally originate from rapid reconfigurations at the single-particle scale. Numerous techniques have been used to image the dynamics of phase transitions, including high-resolution transmission electron microscopy (TEM),[20,93] low-energy electron microscopy (LEEM),[94] scanning tunneling microscopy (STM),[95] and atomic force microscopy (AFM).[96] These techniques have been applied to a variety of different physical systems, such as electrochemical cells,[79] ion-intercalated systems,[19] surface catalysts,[97] two-dimensional materials,[98] and nanocrystals in solution.[99] However, high-resolution imaging of phase transitions at the single-atom/single-molecule level, including *both* the liquid and solid phases, has so far eluded even the most advanced microscopy due to the non-crystalline nature of liquids and their fast dynamics. Recent progress in this direction has been made using a new technique that is able to image two-dimensional (2D) molecular liquids via STM by confining molecular motion to the surface of a graphene field-effect transistor (FET) and using low temperature (4.5K) to rapidly quench dynamics.[34] Here the time evolution of the liquid state is controlled by passing current through the FET to warm it briefly and thereby control the rate of the liquid kinetics. So far this technique has only been utilized to explore 2D molecular liquids[34] and has not been applied to mixed phase solid-liquid systems.

Here we demonstrate the ability to electrically control a 2D solid-liquid phase transition while imaging all constituent particles of both phases at the atomic scale via STM. This was achieved by depositing 2,3,5,6-Tetrafluoro-7,7,8,8-tetracyanoquinodimethane (F_4TCNQ) molecules onto clean graphene FETs having back-gate and source-drain electrodes operable at T = 4.5K in an ultrahigh vacuum STM. We find that lowering the Fermi energy (E_F) of the FET via electrostatic gating causes molecular F_4TCNQ adsorbates to freeze into a solid, quasi-one-dimensional (1D) chain-phase, while raising E_F causes the molecular solid to melt into a 2D liquid phase. Scanning tunneling spectroscopy (STS) measurements reveal that molecules in the solid phase are charge-neutral while molecules in the liquid phase are negatively charged. By applying short pulses of source-drain current to transiently heat the device, we are able to observe the nonequilibrium dynamics of molecules undergoing both melting and freezing processes. We have developed an analytical theoretical framework that explains the equilibrium energetics of this first-order solid-liquid phase transition as a function of gate voltage (including the mixed phase regime), and we have performed Monte Carlo simulations that capture its nonequilibrium melting dynamics.

5.2 Methods

The key experimental technique that enables these observations is our ability to tune the diffusivity of adsorbed molecules by applying source-drain current (I_{SD}) to the graphene FET to briefly heat the surface (a sketch of the device can be seen in Fig. 5.1 (i)). When the sample is heated by I_{SD} (what we term "diffusive conditions"), simultaneous application of a back-gate voltage (V_G) reversibly drives the solid-liquid phase transition of F_4TCNQ adsorbates. If I_{SD} is applied for a sufficient amount of time, then the surface molecular configuration reaches a mixed-state equilibrium defined by a specific liquid phase molecular density set by V_G. If I_{SD} is set to zero before the surface molecules reach equilibrium then the molecular kinetics halt midway, thus allowing intermediate nonequilibrium states to be imaged as the system evolves toward equilibrium. This technique allows movies to be made of molecular evolution through changing equilibrium landscapes, as well as exploration of fast nonequilibrium dynamics as molecules transition from one equilibrium state to another.

5.3 Results

Fig. 5.1 shows the reversible melting/freezing of a partial monolayer of F_4TCNQ on a graphene FET as it transitions through different equilibrium states as a function of applied V_G. For V_G = -30 V (Fig. 5.1 (a)) the molecules all lie in a solid chain phase after flowing a current of I_{SD} = 1mA through the device for 180 sec (all images and spectroscopy are acquired only after setting I_{SD} to zero to quench molecular motion). Locating regions on the surface that exhibit the solid phase is challenging because it covers only a small fraction of the device surface (< 10%) under typical experimental conditions, which explains why it was not observed previously.[34] Close-up STM and AFM images of the solid phase reveal two similar quasi-1D chain morphologies that we call "linear" and "zigzag" (Fig. 5.1 (j)).

Subsequent raising of the gate voltage to V_G = 0 V under diffusive conditions (*i.e.*, by setting I_{SD} = 1 mA for 180 sec) causes the molecular solid to melt. This can be seen in Fig. 5.1 (b) which shows isolated F_4TCNQ molecules dotting the surface near the edge of the solid phase in the same area as Fig. 5.1 (a) (the isolated molecules belong to the liquid phase). Fig. 5.1 (b) shows an equilibrium configuration, meaning that the average concentrations of the liquid and solid phases have stopped changing with time under diffusive conditions (the time to reach equilibrium can vary strongly with gate voltage, but is typically < 60 seconds). The images in Fig. 5.1 (c), (d) show the equilibrium configurations of the same region after incrementally raising the gate voltage first to V_G = 6V and then to V_G = 30V under diffusive conditions. For every step increase in V_G the solid is seen to melt a little more until it is completely liquefied at V_G = 30V. Fig. 5.1 (e)-(h) show the same surface region as V_G is decreased back to -30V under identical diffusive conditions. The liquid-solid phase transition is seen to be completely reversible.

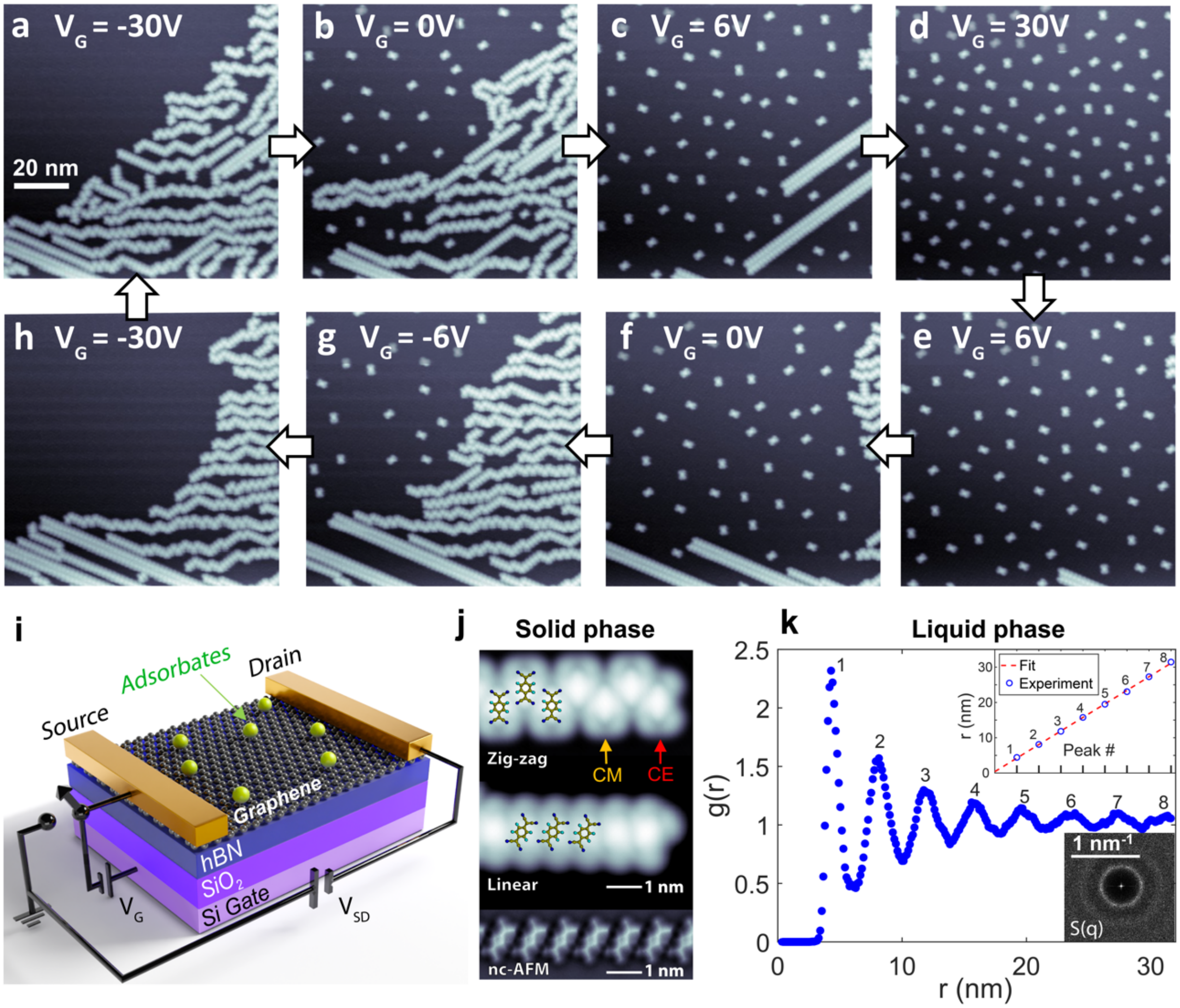

Fig. 5.1 Gate-tunable solid-liquid molecular phase transition. (a)-(d) STM images show the melting of self-assembled chains of F_4TCNQ molecules (solid phase) into isolated molecules (liquid phase) as V_G is increased from -30V, 0V, 6V to 30V. (e)-(h) The reverse phase transition (liquid to solid) is observed at the same spot on the surface with molecules coalescing from liquid phase into self-assembled chains as V_G is decreased to 6V, 0V, -6V and -30V. (i) Schematic of the experimental setup shows F_4TCNQ molecules adsorbed onto the surface of a graphene field-effect transistor (FET) device. (j) Closeup STM images of the molecular chain phase (with structural overlays) show two observed geometries (linear and zig-zag), both having a center-to-center molecular distance of 8.6 Å. A bond-resolved nc-AFM image in the bottom row (obtained with a CO tip[100]) reveals the linear geometry in greater detail. (k) The radial distribution function $g(r)$ of molecular positions in the liquid phase shows a shell-like structure characteristic of liquids having an average shell spacing of 3.84 nm. The corresponding structure factor $S(\mathbf{q})$ shown in the inset indicates that the liquid is isotropic. STM images obtained at T = 4.5K.

Justification for calling the molecular phase containing isolated molecules a liquid comes from an analysis of the molecular radial distribution function, $g(r)$, and structure factor, $S(\boldsymbol{q})$. Fig. 5.1 (k), for example, shows $g(r)$ extracted from a large-area image containing isolated molecules prepared under equilibrium conditions. $g(r)$ shows evenly-spaced peaks with a spacing of a = 3.84 nm, as expected for the shell-structure of an isotropic liquid[101]. The structure factor seen in the Fig. 5.1 (k) inset is also indicative of an isotropic liquid and shows no evidence of crystal or gas behavior[101].

Understanding the cause of the observed molecular phase transition requires understanding how charge transfers between molecules and graphene under different gating conditions. STS measurements were used to gain insight into this process by separately measuring the local electronic structure of the solid and liquid phases. Fig. 5.2 (a) shows dI/dV spectra measured on an F$_4$TCNQ chain (solid phase) compared to an isolated F$_4$TCNQ molecule (liquid phase) for V_G = -60V (this is the hole-doped graphene regime as shown by the inset electronic structure diagram in Fig. 5.2 (a)). The bare graphene spectrum for this surface (taken 10 nm away from any molecules) is shown as an inset for reference. A dip in the bare graphene local density of states (LDOS) near V = 0.34 V marks the location of the graphene Dirac point (E_D), thus verifying that graphene is in the hole-doped regime for this gate voltage. The gap-like feature at V = 0 (E_F) arises from a well-known phonon-assisted inelastic tunneling (IT) effect[89].

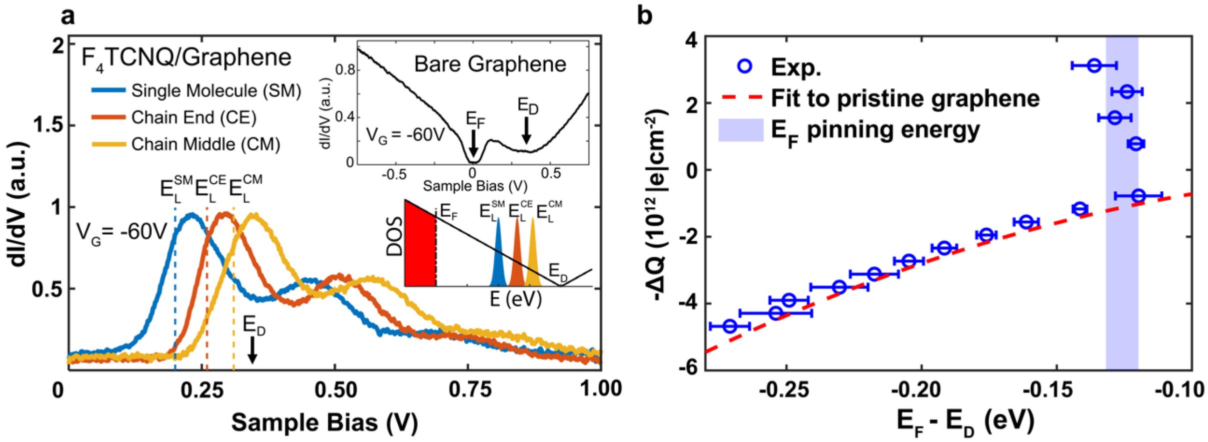

Fig. 5.2 Electronic energy level alignment between graphene and F4TCNQ molecules, and charge accumulation under electrostatic gating. (a) dI/dV spectra taken at V_G = -60 V for F$_4$TCNQ molecules at the chain middle (CM), the chain end (CE), and for single, isolated molecules (SM) (images shown in Fig. 5.1). Inset plot shows dI/dV spectrum measured on bare graphene for V_G = -60V. Inset sketch shows the relative energy alignments of the CM LUMO state, the CE LUMO state, the SM LUMO state, the Fermi energy (E_F), and the Dirac point (E_D). (b) Total charge density accumulated in the molecule/graphene surface (measured capacitively and plotted in terms of electron density) as a function of E_F - E_D (as determined by STS). The discontinuity at E_F - E_D = -0.125 eV signifies a first-order phase transition. STS spectra obtained at T = 4.5K.

The blue curve in Fig. 5.2 (a) shows the dI/dV spectrum for a single, isolated F$_4$TCNQ molecule (SM) in this hole-doped regime. The leading edge of the first peak marks the LUMO energy as discussed in previous work[26,34] (E_L^{SM} = 0.2 eV and is marked by a dashed blue line), while the second peak (V_b ~ 0.4 V) is a phonon satellite arising from intramolecular vibrations.[26] The F_4TCNQ LUMO level is unoccupied for this value of V_G. The second curve (red) shows the dI/dV spectrum measured with the STM tip held over the end molecule of an F_4TCNQ chain (the chain end (CE) as shown in Fig. 5.1(j)). The CE spectrum is nearly identical to the single molecule spectrum except that E_L is shifted up by 0.06 eV. The third curve (orange) shows the spectrum for a molecule in the middle of a chain (CM) (as shown in Fig. 5.1 (j)). Here E_L is pushed up even further by an additional 0.05 eV. The overall energy-level structure is schematically represented by the inset sketch which shows the energy level alignment of the SM LUMO, the CE LUMO, and the CM LUMO relative to E_D and E_F (the experimental energy levels of the zigzag and linear chains are identical).

5.4 Discussion

This energy-level structure has important consequences for F_4TCNQ/graphene solid-liquid phase transitions. For example, suppose that V_G were first set to V_G = -60V (the case shown in Fig. 5.2 (a)) and then slowly increased under diffusive conditions. This would cause E_F to slide to the right and to eventually intersect with E_L^{SM}. The first molecules to fill with charge due to the increasing V_G would thus be isolated F_4TCNQ molecules. As shown previously,[34] under these conditions E_F becomes *pinned* close to E_L^{SM} and so never reaches the chain orbitals (E_L^{CE} or E_L^{CM}) which therefore remain charge-neutral (i.e., unoccupied) for a wide range of V_G values. Increasing V_G while E_F is pinned in this way causes molecules to melt from the neutral solid and to fill with charge, thereby increasing the density of the charged liquid phase (separation between the isolated molecules is explained by Coulomb repulsion).

A useful thermodynamic variable to characterize this process is the total charge density in the molecule-decorated graphene system, $-\Delta Q$ (this counts the excess density of electrons). When the molecular chains begin to melt in response to increased V_G, $-\Delta Q$ exhibits a discontinuous jump when plotted as a function of E_F as shown in Fig. 5.2 (b). $-\Delta Q$ here is obtained from the relationship $-\Delta Q = CV_G$ where C is the capacitance per area between the graphene and the gate electrode. E_F and E_D are measured as a function of V_G from STM spectroscopy (by fitting the dI/dV spectrum as shown in the inset to Fig. 5.2 (a)) and the discontinuity in $-\Delta Q$ is observed to occur at $E_F - E_D \approx$ -0.125 eV. For $E_F - E_D <$ -0.125 eV the molecules are all in the charge-neutral chain phase, so any increase in $-\Delta Q$ while E_F is in this regime reflects filling of the graphene Dirac band and follows the well-known parabolic dependence of graphene.[90] When E_F reaches the critical value of $E_F - E_D$ = -0.125 eV, however, charge begins to flow into the F_4TCNQ LUMO states as the chain phase melts to accommodate the additional charge. The molecules have a high quantum capacitance at this energy, so device charge accumulates rapidly in this regime as E_F is increased and exhibits discontinuous behavior as shown in Fig. 5.2 (b). The E_F dependence of $-\Delta Q$ in Fig. 5.2 (b) is reminiscent of the temperature dependence of transferred heat in a standard temperature-driven solid-liquid melting transition (such as ice to water) where latent heat must be provided to increase entropy as the solid converts to a liquid. Here E_F is analogous to temperature and the number of excess electrons ($-\Delta Q$) is analogous to entropy, so one can think of "latent charge" as being necessary to induce 2D molecular melting in our devices.[54]

These insights enable us to develop a theoretical model for quantitatively understanding the microscopic energetics of the F_4TCNQ/graphene solid-liquid phase transition. We first note that the F_4TCNQ molecules and graphene both exchange electrons with the gate which acts as a reservoir. The thermodynamics of such an open system is described by the grand potential. Under our low-temperature experimental conditions (20~30K with current flow) the entropy contribution $T\Delta S$ to the grand potential is expected to be small, and so we model the grand potential as follows:

$$\Phi = \mathrm{U} - E_F N_e \,. \tag{5.1}$$

Here U is the total energy and N_e is the total number of electrons relative to a reference state (i.e., the state where all electrons occupy graphene band states with energy $E < E_L^{SM}$ and the molecules are uncharged). Since the LUMO energy of the chains is higher than that of the isolated molecules, we ignore the possibility of the chains becoming charged and assume that electrons occupy either single-molecule LUMO states or graphene Dirac band states. The graphene contribution to the total energy relative to the reference state is denoted by $U_g(E_F) = \int_{E_L}^{E_F} \epsilon \; g(\epsilon) A \; d\epsilon$, where $g(\epsilon)$ is found from the well-known linear band model[39] to be $g(\epsilon) = \frac{2A(E_D-\epsilon)}{\pi\hbar^2 v_F^2}$. If we assume that our system has a total of N molecules that are all in the neutral chain phase, then the molecular energy can be approximated as $U_s(N) \approx -\alpha N$ where $-\alpha$ corresponds to the energy per bond between adjacent molecules. We denote the number of electrons in this pure solid phase as $N_{e,s}$, in which case the grand potential is

$$\Phi_{\mathrm{s}} = U_s(N) + U_g(E_F) - E_F N_{e,s} \,. \tag{5.2}$$

On the other hand, if the N molecules are all in the charged liquid phase then the molecules are each charged by one electron in the LUMO and the molecular contribution to the total energy becomes $U_l(N) = E_L N$ (for simplicity we have dropped the superscript "SM" from E_L). We denote the number of electrons in this pure liquid phase as $N_{e,l}$, in which case the grand potential is

$$\Phi_l = U_l(N) + U_g(E_F) - E_F N_{e,l} \,. \tag{5.3}$$

The critical Fermi level (E_F^c) at which the phase transition occurs is determined by setting $\Phi_{\mathrm{s}} = \Phi_l$. At this Fermi level $N_{e,l} - N_{e,s} = N$ since N electrons are needed to charge the molecules, thereby yielding $E_F^c = E_L + \alpha$. For $E_F < E_F^c$ all of the electrons reside in graphene band states and all of the molecules are condensed into solid chains due to the energy gain of bond formation. For $E_F > E_F^c$, on the other hand, all of the molecules are in the charged liquid state. The transition from the solid phase to the liquid phase does *not* occur when $E_F = E_L$ because melting the chains requires extra energy to break the bond between a chain end molecule and its neighbor (i.e., the latent heat of melting). The process of adding a charged, isolated molecule to the liquid phase only becomes energetically favorable when the Fermi level reaches a value equal to E_L *plus* the energy required to break one bond (α). This insight allows us to, in principle, experimentally obtain α by comparing the measured value of E_F^C at which the phase transition occurs (which is marked by Fermi level pinning) to spectroscopic measurements of E_L. Experimentally we observe E_F^c to be 120±20 meV below the Dirac point energy and E_L to be 140±5 meV below the Dirac point (E_L was determined previously[34]). The difference between these quantities is on the order of our experimental uncertainty, and so we are not yet able to extract an accurate value of α from our data. We are, however, able to place an upper limit on α: $\alpha \lesssim 40$ meV (this is reasonably consistent with a DFT-based estimate of α (see SI)).

While the grand potential is continuous at the phase transition, its first derivative with respect to E_F is not. From Eqs. (5.2) and (5.3) we see that $\frac{\partial \Phi_l}{\partial E_F}$ and $\frac{\partial \Phi_s}{\partial E_F}$ differ by N at $E_F = E_F^c$, confirming that this is a first-order phase transition and that the "latent charge" required for complete conversion of N molecules in the solid phase to the liquid phase is the charge of N electrons. This is consistent with the experimental discontinuity in $-\Delta Q$ seen in Fig. 5.2 (b) which reflects the charge transferred to melted F_4TCNQ while E_F is pinned at the critical value. The preceding discussion has focused on equilibrium conditions of the pure liquid phase ($E_F > E_F^c$) versus pure solid phase ($E_F < E_F^c$), but we are also able to characterize the nonequilibrium solid-liquid (mixed phase) coexistence regime (i.e., unstable excursions from $E_F = E_F^c$) where the proportion of molecules in the chain and liquid phases can be adjusted from one equilibrium state to another (Fig. 5.3). Fig. 5.3 (a) shows a plot of the experimental liquid phase molecular density (N_l /A, where A is the graphene area) versus $V_G - V_0$ where V_0 = -10V is the gate voltage at which isolated molecules *first* appear in STM images. The yellow dots in Fig. 5.3 (a) show that the experimental equilibrium values for N_l/A exhibit a linear dependence on gate voltage. The magenta dots, on the other hand, show experimental nonequilibrium data obtained by changing V_G and I_{SD} in such a way that diffusive conditions do not last long enough for the system to fully equilibrate. Fig. 5.3 (b)-(g) show a full cycle of the system (measured at a single location on the device) as it evolves from one equilibrium configuration to a different one (yellow dots) and then back again by transitioning through a series of intermediate nonequilibrium states (magenta dots).

We start with Fig. 5.3 (b) which shows a patch of the surface that was initially in an equilibrium state at $V_G - V_0$ = 60 V. At this gate voltage a relatively high liquid phase density ($N_l/A = 4.1 \times 10^{12}$ molecules/cm^2) coexists with a much lower concentration of the solid phase. The gate voltage was then changed to $V_G - V_0$ = 50 V under *non-diffusive* conditions (i.e., I_{SD} = 0) to set a new equilibrium target, but without allowing the system to evolve toward the new target (since the kinetics are quenched by keeping I_{SD} = 0). The resulting nonequilibrium configuration is denoted t = 0 and is visually identical to the equilibrium state at $V_G - V_0$ = 60 V. Fig. 5.3 (c) shows the same region after subjecting it to diffusive conditions (by setting I_{SD} = 1.1 mA) for Δt = 50 ms while holding the gate voltage constant at $V_G - V_0$= 50 V. The solid phase density is seen to increase, but equilibrium is not yet established. Fig. 5.3 (d) shows the same region after allowing it to evolve for an additional 50ms under diffusive conditions while maintaining $V_G - V_0$ = 50 V. The system is now in equilibrium with N_l/A reduced to 3.5×10^{12}molecules/cm^2 and the solid density correspondingly increased. Fig. 5.3 (e)-(g) show the same process in reverse as V_G is reset to the original value of $V_G - V_0$ = 60 V . The system is observed to evolve back to its original equilibrium configuration after passing through a nonequilibrium (Fig. 5.3 (f)) regime.

The mixed phase solid/liquid configurations observed in Fig. 5.3 can be understood within our theoretical framework in a straightforward way. To do this we consider the total energy of a mixed phase state containing N_l molecules in the liquid phase and $N - N_l$ molecules in the chain phase given by

$$U(N_l, E_F) = U_l(N_l) + U_s(N - N_l) + U_g(E_F), \qquad (5.4)$$

where U_l, U_s, U_g, and N are defined the same as for Eqs. (5.2) and (5.3). Here N is constant, and E_F is determined by V_G and N_l. Only N_l remains variable, and its value at equilibrium N_l^{eq} is obtained by minimizing Eq. (5.4) with respect to N_l. The resulting expression for N_l^{eq} per unit area is

$$\frac{N_l^{eq}}{A} = CV_G + \frac{|E_D - (E_L + \alpha)|^2}{\pi\hbar^2 v_F^2}, \tag{5.5}$$

where A is the area of the graphene capacitor, E_L is the LUMO energy, E_D is the Dirac point energy, and v_F is the Fermi velocity near the Dirac point ($1.1 \times 10^6\ m/s$). This expression is similar to an expression derived in ref. [34] using a different approach, but the new expression differs in the last term of which arises due to the energy required to break a bond (α), a factor not considered in ref. [34]. Eq. (5.5) is plotted in Fig. 5.3 (a) (white dashed line) and is seen to match the equilibrium data (yellow dots) quite well. The nonequilibrium behavior (magenta dots) can be explained by plotting U from Eq. (5.4) as a color map depending on both V_G and N_l in Fig. 5.3 (a). The low-energy region of $U(N_l, V_G)$ is seen to correspond to precisely the equilibrium density defined by Eq. (5.5) (as expected). Excursions from equilibrium, as shown by the magenta dots, thus push the system to higher energy. The energy landscape of Fig. 5.3 (a) is consistent with the experimentally observed tendency of the system to relax back down in energy to the equilibrium configuration.

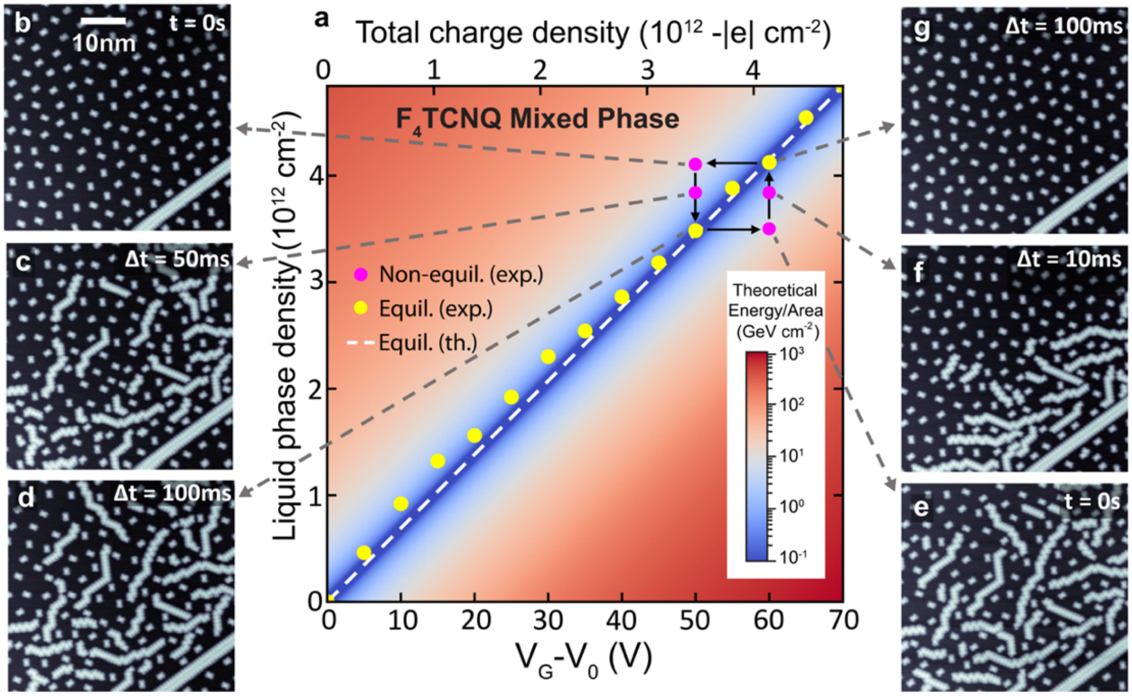

Fig. 5.3 F$_4$TCNQ chain freezing and melting under non-equilibrium conditions.
(a) Experimental values of the equilibrium liquid phase molecule density (N_l/A) are plotted as yellow dots and non-equilibrium values as magenta dots. The theoretical total energy of the equilibrium mixed phase of F$_4$TCNQ/graphene is also shown (color scale) as a function of liquid phase surface density and gate voltage (V_0 is the gate voltage at which melting first begins). The minimum energy configuration corresponds to the dashed white line (obtained from Eq. (5.5)). (b) STM image of the non-equilibrium molecular state obtained by switching V_G -V_0 to 50 V starting from the equilibrium state at V_G -V_0 = 60 V and not allowing the system to evolve under diffusive conditions (t = 0). (c) Molecular chains condense into a new non-equilibrium state after allowing the system to evolve for 50ms under diffusive conditions (I_{SD} = 1.15 mA, V_G -V_0 = 50 V). (d) Molecular chain condensation advances to this equilibrium state after waiting an additional 50ms under diffusive conditions (I_{SD} = 1.15 mA, V_G -V_0 = 50 V). (e) STM image of the non-equilibrium state obtained by switching V_G -V_0 to 60 V and not allowing the system to evolve under diffusive conditions (t = 0). (f) Molecular chains have partially melted in this new non-equilibrium state obtained after allowing the system to evolve for 50ms under diffusive conditions (I_{SD} = 1.11 mA, V_G -V_0 = 60 V). (g) Molecular chains have melted even further in this equilibrium state obtained after waiting an additional 100ms under diffusive conditions (I_{SD} = 1.11 mA, V_G -V_0 = 60 V), thus returning the molecular density to its initial configuration in (b). STM images obtained at T = 4.5K.

A more dramatic example of nonequilibrium behavior is shown in Fig. 5.4 which exhibits the time evolution of a nonequilibrium melting process at the molecular solid-liquid interface. The STM image in Fig. 5.4 (a) shows that the equilibrium configuration (t = 0) at V_G = -20 V exhibits a region of high solid phase density (upper left) and zero liquid phase density everywhere else. The surface was then put into a nonequilibrium state by rapidly changing the gate voltage to V_G = 60V (corresponding to an expected high equilibrium liquid phase concentration). The system was then allowed to evolve under diffusive conditions for Δt = 500μs before being quenched and imaged as shown in Fig. 5.4 (b). This nonequilibrium snapshot shows a "wave" of liquid phase molecules emanating from the molecular solid like water from a melting glacier. The width of the liquid layer extends outward from the solid by ~80nm and exhibits an interparticle spacing that is mostly constant. Fig. 5.4 (c) shows the same area after allowing it to evolve under diffusive conditions for another 700μs. The layer of liquid now extends outward from the solid by more than 160nm.

The theoretical framework discussed up to now is inadequate to model this type of nonequilibrium dynamics. To better understand this melting process we have generalized our overall model to account for: (i) multiple chains, (ii) isolated *uncharged* molecules, and (iii) screened Coulomb interactions between ionized molecules. We have numerically simulated this more complete model using the Monte Carlo method to explain the dynamics shown in Fig. 5.4 (a)-(c). An initial configuration was chosen with molecules arranged into chains to mimic the F_4TCNQ solids we observe experimentally (Fig. 5.4 (d)). All model parameters were constrained by experiment except for α (for which we only have an upper bound), but our results do not strongly depend on the precise value of α. A fixed number of electrons was added to the system at the start of the calculation to simulate the gating process, and the resulting liquid phase density and E_F value were subsequently determined. Overall, the simulation produced results quite similar to the experiment. For example, isolated molecules were observed to dissociate from chains after only a few Monte Carlo steps and to move towards empty graphene regions (Fig. 5.4 (e), (f)), similar to the flow of molecules observed experimentally in Fig. 5.4 (b), (c).

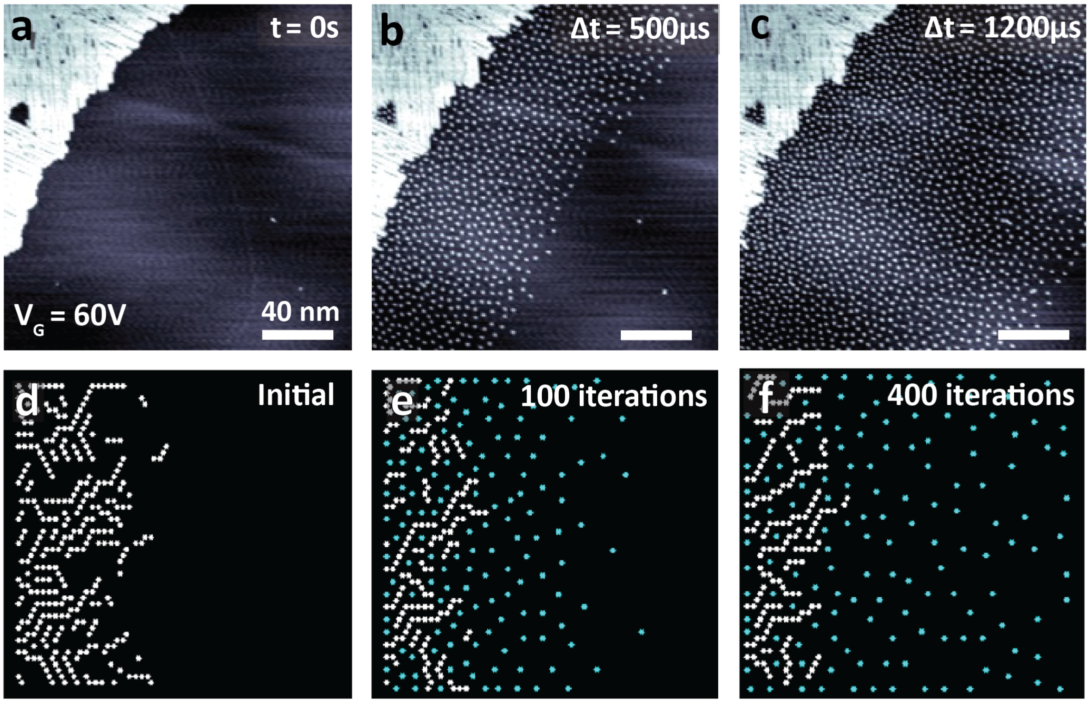

Fig. 5.4 Non-equilibrium melting of the F4TCNQ solid. (a) STM image of equilibrium F_4TCNQ solid formed under diffusive conditions on graphene FET at $V_{G\text{-set}} = -20V$. V_G was stepped up to $V_G = 60$ V before imaging, but the system was not allowed to evolve under diffusive conditions (*t* = 0). (b) Same region of surface after allowing it to evolve under diffusive conditions for Δt = 500μs ($I_{SD} = 1.3$ mA, $V_G = 60$ V). A "wave" of charged liquid phase molecules can be seen emanating from the solid interface. (c) Same region after allowing the system to evolve for an additional Δt = 700μs under diffusive conditions (V_G = 60 V). The flow of the charged molecular liquid has extended even further from the condensed phase interface. (d)-(f) Monte Carlo simulations of F_4TCNQ molecules disassociating from chains to model the behavior shown in (a)-(c). Molecules colored in blue are charged and can be seen flowing outward from the charge-neutral condensed phase interface. STM images obtained at T = 4.5K.

5.5 Conclusion

In conclusion, we have observed a gate-tunable first-order solid-liquid phase transition for F_4TCNQ molecules adsorbed onto the surface of a graphene FET. We are able to control and image the relative abundances of liquid and solid phases for different equilibrium conditions and to directly visualize the nonequilibrium dynamics of this system with single-molecule resolution for *both* the solid and liquid phases. We have developed an analytical model that explains the gate-dependent equilibrium properties of this system with the only unknown parameter being the energy of cohesion of the molecular solid. The techniques described here provide a new method for experimentally extracting this parameter, and our results put an experimental upper bound on it equal to 40meV per molecule. Monte Carlo simulations show reasonable agreement with the highly nonequilibrium kinetics observed in our experiment. The phenomenology observed here should be generalizable to other adsorbate/surface systems that are gate-tunable.

6 Gate-tunable Molecular Diffusion on a Graphene FET

The ability to tune surface diffusion using electrostatic gating is potentially useful for controlling surface reactions, catalysis and material deposition. In this chapter I will demonstrate our control over the diffusion of F_4TCNQ molecules at the surface of a graphene field-effect transistor (FET) by electrostatic gating. We have found that by tuning the applied gate voltage the molecular charge state can be switched from negatively to neutral, leading to a dramatic change in molecular diffusion behavior. The diffusion barrier was not found to depend strongly on the applied gate voltage for charged molecules, but it increases rapidly for lower gate voltages for neutral molecules. By using a "freeze-frame" heating technique in our scanning tunneling microscope (STM) we were able to track molecule positions and identify distinct molecular diffusion paths associated with different charge states. *Ab initio* DFT calculations were used to calculate the diffusion barrier, but did not fully explain the gate-dependent trends observed in the experimental diffusion data.

6.1 Introduction

Surface diffusion plays a central role in many fundamental processes such as catalysis,[102,103] mass transport in porous materials,[104,105] and thin-film deposition.[106,107] In catalytic applications the surface diffusion rate directly controls reaction rates, while for thin-film deposition control of the surface diffusion rate is crucial to the formation of ultra-stable glasses with minimal two-level systems.[107] Usually the surface diffusion rate is controlled by changing the temperature T of a system since surface diffusion is a thermally activated process governed by the Boltzmann factor $e^{-\Delta/k_BT}$, where Δ is the surface diffusion barrier. However, it is in principle also possible to control the diffusion rate by tuning the surface diffusion barrier Δ, a much less explored option. The ability to tune the diffusion barrier allows surface diffusion processes to be controlled independently of temperature. While previous studies have demonstrated that atomic diffusive behavior is sensitive to the charge state of adsorbates,[108] this effect has so far not been exploited for dynamically modifying surface diffusion rates in device-tunable systems.

Here we demonstrate the ability to control the diffusive motion of an adsorbed molecule on a graphene field effect transistor (FET) by electrostatic gating. We measured the gate voltage-dependent diffusion barrier of molecules adsorbed to the FET surface by directly tracking the diffusive motion of individual molecules under different gating conditions. The molecule studied was 2,3,5,6-Tetrafluoro-7,7,8,8-tetracyanoquinodimethane (F_4TCNQ) which has previously been found to have a switchable charge state that is tunable by electrostatic gating on graphene.[34] We found that the charge state of this molecule strongly affects its diffusive behavior. In particular, when the molecule is uncharged its diffusion barrier is strongly dependent on the applied gate voltage, but when the molecule is charged its diffusion barrier is independent of applied gate voltage. Detailed tracking of molecular orientations reveals that the charge state of the molecule determines the energetically favored diffusion paths for different applied gate voltages, thus explaining the gate voltage dependence of the diffusion barrier for charged versus uncharged molecules. DFT calculations of the minimum energy diffusion barrier agree well with the experimentally measured values, but fail to perfectly reproduce the preferred diffusion paths under some conditions.

6.2 Methods

To study the diffusive behavior of gate-tunable molecules, we observed molecular diffusion at different temperatures. F_4TCNQ molecules were first deposited onto a graphene FET under ultra-high vacuum. The sample was then cooled down to 4.5K in a cryogenic STM for measurement. The molecular density on the graphene surface was adjusted to $(3 \pm 1) \times 10^{11}\ cm^{-2}$ under an applied gate voltage of 5V while flowing source-drain current through the device, following the procedure described in ref. [34]. A typical surface molecule density is shown in Fig. 6.1 (a). The tip was then withdrawn $2\mu m$ from the surface and a diode heat source located close to the sample was used to heat the graphene device for 60s. The temperature of the sample was monitored by a thermometer diode close to the sample plate. The heating procedure was controlled by a PID feedback loop to rapidly heat and maintain the target temperature (typically between 10K and 35 K) for 60s before the device was cooled back down to 4.5K. After the temperature of the device cooled back down to 4.5K we imaged the surface with the STM and tracked the centroid positions of each molecule in our field of view (typically $100\ \text{nm} \times\ 100\ \text{nm}$).[109] Using this method, which we refer to as "direct heating", we can produce a freeze-frame movie of molecular motion occurring as a result of each heating cycle.

6.3 Results

A series of STM images taken after performing the protocol described above is shown in Fig. 6.1 (a)-(d) where individual molecular trajectories have been overlaid. The drift of the scan frame after each heating cycle was seen to be small (typically ~3 nm per heating cycle). The individual molecular tracks were then analyzed to extract the ensemble-averaged mean-square displacement (MSD) as a function of time. An example of the molecular MSD is plotted for different heating temperatures in Fig. 6.1 (e). A diffusive MSD in two dimensions follows the well-known relation $\langle \Delta r^2 \rangle = 4Dt^{\alpha}$, where Δr is the root mean square molecular displacement from the origin at time t, D is the diffusion constant, and α is the power law of the diffusion ($\alpha = 1$ describes perfect Brownian motion, $\alpha < 1$ is subdiffusive, and $\alpha > 1$ is superdiffusive). Our experimental data shows $\alpha = 0.97 \pm 0.1$ for all the curves in Fig. 6.1 (e), indicating that the movement of molecules under these conditions is well characterized by Brownian motion. By taking the logarithm of the MSD we are able to extract the diffusion constant as the intercept term. As seen in the data of Fig. 6.1 (g) we observe that the molecular diffusion constant increases exponentially with linearly increasing heating temperature since the intercept of the MSD logarithm curves are roughly evenly spaced apart. This method allows us to extract the molecular diffusion constant for different heating temperatures and gating conditions.

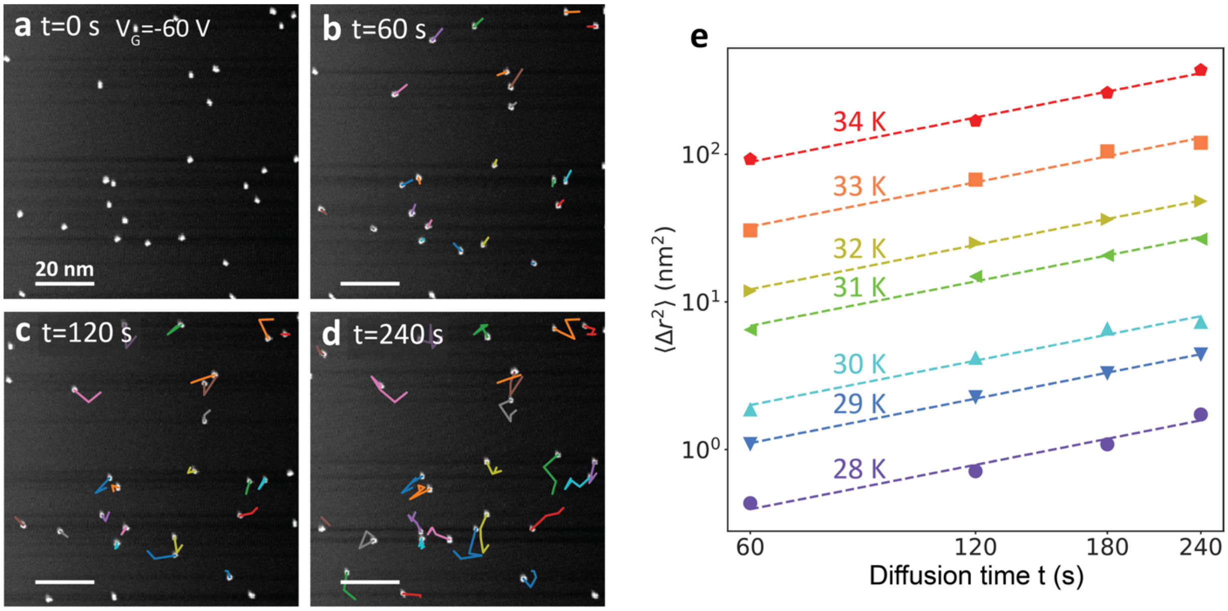

Fig. 6.1: Tracking molecular diffusion on a graphene surface. (a)-(d) A series of STM topographs shows F$_4$TCNQ molecules diffusing on graphene after each heating step. Overlaid molecular tracks show the trajectories of diffusion. (e) Mean squared displacement of the tracked molecules as a function of diffusion time. The diffusion constant D is found from the intercept of the log mean square displacement.

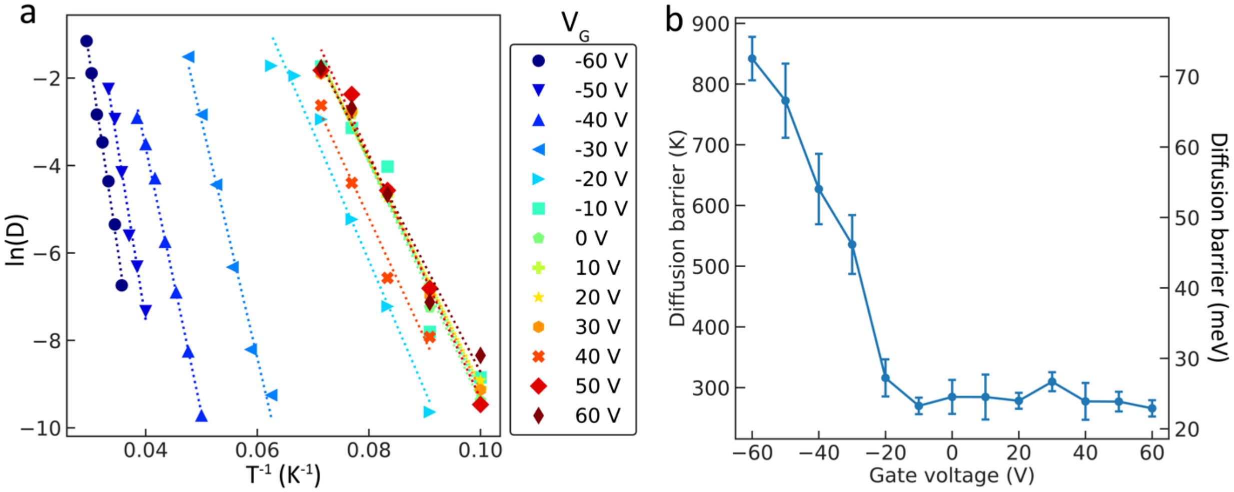

Fig. 6.2 Gate-dependent molecular diffusion barrier. (a) Extracted diffusion constants D plotted as a function of heating temperature and gate voltage. The diffusion constants are roughly constant for $V_G > -20\ V$, but vary strongly with V_G for $V_G < -20\ V$. (b) The diffusion barrier E_a is extracted from the slope of $\log(D)$ and shows a strong dependence on gate voltage for $V_G < -20\ V$.

Fig. 6.2 (a) shows a series of extracted diffusion constants as a function of heating temperature for different applied gate voltages (V_G), where $-60\text{V} \leq V_G \leq 60\text{V}$. The measured diffusion constants for the different applied gate voltages are plotted as connected points versus 1/T, where T is the temperature. All diffusion constants were measured in the same scan area.

For classic Brownian diffusion in two-dimensions the diffusion barrier E_a is related to the diffusion constant D by

$$\log(D) = \log\left(\frac{a\nu_0^2}{4}\right) - \frac{E_a}{k_B T}, \tag{6.1}$$

where a is the distance per jump to a neighboring adsorption site, ν_0 is the attempt frequency, and T is the temperature at which the diffusion occurs. By performing a linear fit to our $\log(D)$ curves, we estimate the diffusion barrier energy for each applied gate voltage and plot it in Fig. 6.2 (b). The resulting gate voltage-dependent diffusion barrier curve (Fig. 6.2 (b)) exhibits two distinct features: (1) The diffusion barrier E_a is nearly independent of the applied gate voltage for $V_G \geq -20V$, and (2) The diffusion barrier E_a increases dramatically for $V_G \leq -20V$, with E_a at V_G = -60V reaching 3.5 times its value at V_G = -20V. We note that the critical gate voltage V_G = -20V roughly coincides with previously reported gate voltages above which F_4TCNQ molecules become negatively charged on similar graphene FETs.[34]

In order to better understand the diffusion behavior in these two distinct gate voltage regimes, we require more detailed information about the molecular diffusion paths. The direct heating method allows us to track molecular motion with reasonable precision, but the error on molecular position after drift correction is still greater than a single lattice constant of graphene. In order to minimize drift and increase our precision regarding the molecular position, we utilized an alternate heating method which we call “current heating”. Here we first follow the same aforementioned procedure for preparing the surface with $(3 \pm 1) \times 10^{11}$ molecules cm^{-2}. The tip is then withdrawn 300nm away from the surface, and a 60 sec. source-drain current pulse is applied to the graphene FET to produce Joule heating and induce molecular diffusion. The source-drain current is then switched off, allowing the graphene to cool down which causes the molecules to stop diffusing on the surface. The tip is then approached to the graphene surface and STM imaging is performed. This “snapshot” of the surface taken after current heating allows the motion of individual molecules to be tracked with high precision, since current heating is local to the device and thus produces significantly less thermal drift for the scan piezos.

We investigated which diffusion paths the molecules were taking on the graphene lattice by tracking both molecular displacements *and* molecular orientational changes occurring between consecutive scan frames. STM images of F_4TCNQ molecules show 3 different orientations for the long axis of the molecule that are separated by 120° from each other as shown in Fig. 6.3 (a). These images are consistent with DFT calculations that suggest that the minimum energy molecular geometries correspond to the center ring and long axis of the F4TCNQ molecule aligning with one of the 3 equivalent “bridge” sites on graphene, as shown in Fig. 6.3 (b). By calculating the image moment of each molecule in the STM images, molecular orientations were classified as one of the 3 distinct orientations. To track the displacement of a particular molecule between two snapshots we first identified its position and molecular orientation in the initial snapshot. We then re-centered and re-oriented the reference frame of the molecule in the initial snapshot such that its centroid lies at the origin and the long axis of the molecule is oriented at 0°. The final molecular position and orientation in the subsequent snapshot was then measured relative to the initial position and orientation.

The resulting displacements for all molecules between consecutive snapshots are aggregated and represented as scatter plots in Fig. 6.3 (c)-(e) and (g)-(i) for different values of V_{SD}. A molecule that has moved a displacement of $(\Delta x, \Delta y)$ between frames is represented as a point with coordinates $(\Delta x, \Delta y)$ in the scatter plot, and the color of the point indicates whether or not the molecule has changed its orientation after moving. Blue points indicate molecules whose orientation remained the same, while orange points indicate molecules that have undergone a change in orientation. Fig. 6.3 (c)-(e) show molecular displacements when the current heating experiment is performed under the condition V_G = 60V (*i.e.* when the molecules are clearly in the charged regime), and Fig. 6.3 (g)-(i) show molecular displacements when the experiment is performed under V_G = -60V (*i.e.* when the molecules are clearly in the neutral regime). Fig. 6.3 (c)-(e) show that the charged molecular displacements are not continuous but instead fall into a discretized triangular lattice with a lattice constant of 2.46 Å, which matches the lattice constant of graphene. For uncharged molecules (Fig. 6.3 (g)-(i)) we observe *additional* points halfway between the triangular lattice pattern produced by charged molecules seen in Fig. 6.3 (c)-(e). In addition, by classifying the motion of the molecules into three categories: (1) no movement, (2) movement without orientation change, (3) movement with orientation change, we can track how their relative population changes as a function of applied source-drain voltage. The percentage of molecules falling into each of these three categories is plotted as a function of applied source-drain voltage in Fig. 6.3 (f) for charged molecules (under conditions V_G=60V), and in Fig. 6.3(j) for uncharged molecules (under conditions V_G=-60V). Fig. 6.3 reveals a striking difference in diffusion paths between charged (Fig. 6.3 (c)-(e)) and uncharged molecules (Fig. 6.3 (g)-(i)). While charged molecules primarily jump to neighboring adsorption sites without rotating, uncharged molecules also rotate as they move to neighboring adsorption sites.

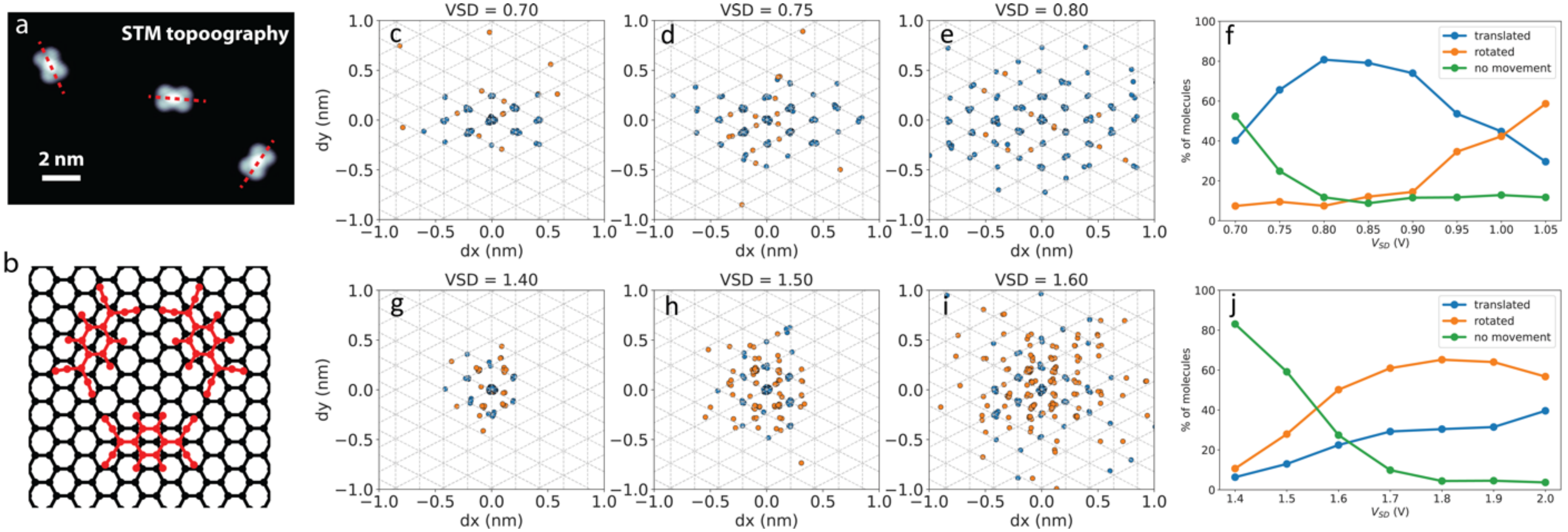

Fig. 6.3 Gate-dependent molecular displacements during diffusion. (a) A STM image of F₄TCNQ molecules on a graphene surface. Three discrete molecular orientations are observed, separated from each other by 120°. (b) Schematic of the minimum energy molecular geometry on graphene, with molecules centered on the " bridge" site. There are 3 equivalent molecular orientations, which explains the molecular 3 orientations observed in (a). (c)-(e) Negatively charged molecules are heated with I_{SD} through the graphene device for 60s under $V_G = 60V$ while increasing V_{SD}. Molecular displacements between two scan frames are represented in real-space as points in a scatter plot, with molecules diffusing under conditions (c) $V_{SD} = 0.7\ V$, (d) $V_{SD} = 0.75\ V$, (e) $V_{SD} = 0.8\ V$. A triangular lattice with lattice constant $a = 2.46$ Å is overlaid on the scatter plots, indicating discrete jumps between stable adsorption sites. Blue dots represent molecules which have not changed their orientation. Orange dots represent molecules that have changed orientation. (f) The percentage of molecules that fall into each movement category (no movement, translation only, and translation with rotation) is plotted as a function of V_{SD}. For charged molecules, translation *without rotation* is dominant. (g)-(i) Neutral molecules are heated using I_{SD} for 60s under $V_G = -60V$ for increasing values of V_{SD}. Molecular displacements between two scan frames recorded under conditions (f) $V_{SD} = 1.4\ V$, (g) $V_{SD} = 1.5\ V$, (h) $V_{SD} = 1.6\ V$. (j) The percentage of molecules that fall into each of the three movement categories is plotted as a function of V_{SD}. For neutral molecules translation *with rotation* is dominant.

6.4 Discussion

The observed triangular lattice of displacements provides crucial information about the diffusion paths taken by the molecules. To explain why the molecular displacements form a triangular lattice, we first consider the neighboring sites that a F_4TCNQ sitting on a “bridge” site can jump to. Fig. 6.4 (a)-(c) shows a molecular jump to a neighboring adsorption site by a translation with no rotational motion, which we refer to as diffusion path “T”. There are 4 equivalent nearest neighbor sites that the molecule can jump to by a translation of a lattice vector (shown as blue dots in Fig. 6.4 (a)). The set of all possible consecutive jumps that a molecule can take following diffusion path “T” forms a triangular lattice with a lattice constant of 2.46 Å, which matches the lattice constant of graphene. Fig. 6.4 (b), (c) show how a molecule might transition between binding sites for a “T” diffusion event. Another possible diffusion path involves a translation accompanied by a 60° rotation, as shown in Fig. 6.4 (d)-(f), which we refer to as path “TR”. For this type of diffusion there are also 4 equivalent nearest neighbor sites that the molecule can jump to (shown as blue dots in Fig. 6.4 (d)). The set of all possible jumps taken in this way forms a Kagome lattice with an inter-site distance of 1.26 Å, which is half the lattice constant of graphene. Fig. 6.4 (e), (f) show the process of a “TR” diffusion event. A third possible diffusion path involves a translation accompanied by a 60° rotation that moves the molecule to a further site than seen for “TR” events, as shown in Fig. 6.4 (g)-(i) We refer to this as diffusion path “TR2”. The molecular jumps following the “TR” and “TR2” paths account for the additional orange points that appear in between the blue triangular lattice points formed by “T” jumps.

The experimental results shown in Fig. 6.3 suggest that “T” diffusion paths are favored when molecules are uncharged while “TR” and “TR2” paths are favored when molecules are charged. The relative prevalence of the different diffusion paths also depends on the source-drain voltage used to heat the graphene (Fig. 6.3 (f), (j)). For lower V_{SD} the number of favored diffusion path events is significantly larger than non-favored diffusion path events, whereas at larger source-drain voltages the number of non-favored diffusion path events increases. This suggests that the non-favored paths are thermally activated at higher temperatures.

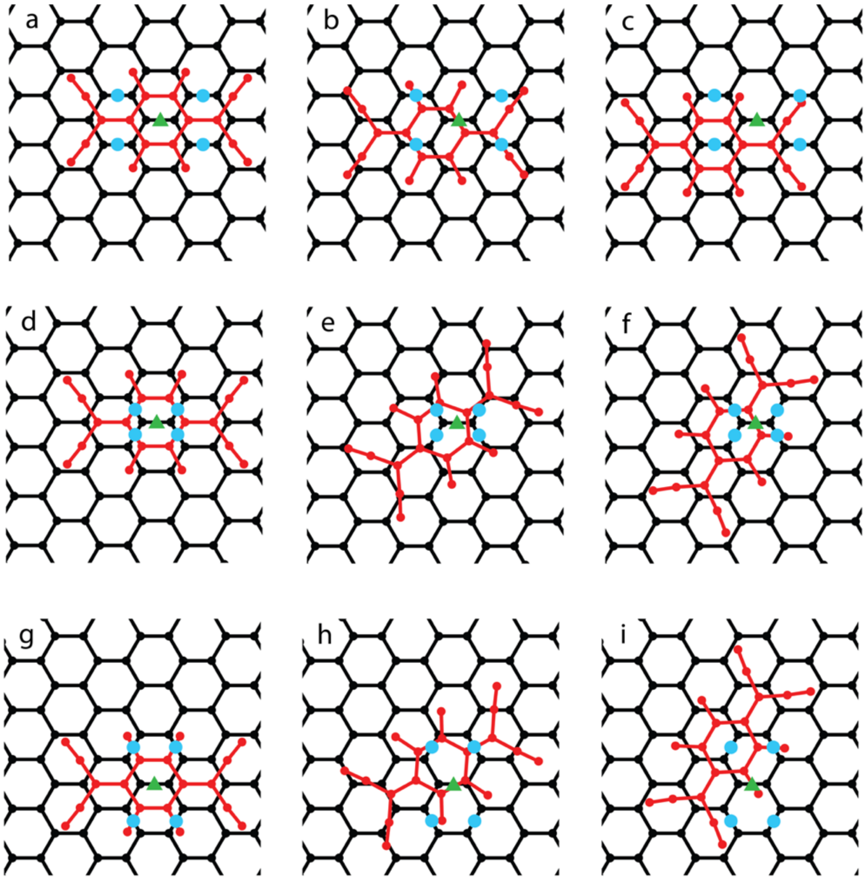

Fig. 6.4 Schematic of molecular diffusion paths. (a) Schematic of a F_4TCNQ molecule sitting on an initial "bridge" site. The green triangle labels the original position of the molecular center. Blue dots label the equivalent neighboring bridge sites that the molecule can jump to by pure translational movement through the diffusion path T. (b) A transition state along the diffusion path T between the green triangle and a blue dot. (c) Final state geometry of the molecule for a diffusion path T. (d) Schematic of a F_4TCNQ molecule sitting on an initial "bridge" site. Blue dots label the equivalent neighboring bridge sites that the molecule can jump to by a translation + rotation of 60° along diffusion path TR. (e) A transition state along the diffusion path TR. (f) Final state geometry of the molecule for diffusion path TR. (g) Schematic of a F_4TCNQ molecule sitting on an initial "bridge" site. Blue dots label the equivalent neighboring bridge sites that the molecule can jump to by a translation + rotation of 60° through diffusion path TR2. (h) A transition state along the diffusion path TR2. (i) Final state geometry of the molecule for diffusion path TR2.

In order to explain the molecules' preference for different diffusion paths under different conditions, we calculated the diffusion barrier as a function of gate voltage and molecular charge state for different diffusion paths (calculations were performed by the Lischner group). To obtain the diffusion barrier from DFT, we first calculated the energy of a series of smoothly varying molecular geometries transitioning between the initial adsorption geometry and the final adsorption geometry for each of the three paths. During these series calculations, the charge of the molecule was not constrained. Then, we identified the transition state geometry corresponding to the maximum barrier height for each of the three paths. After the transition state is identified, we restricted the net charge of the F_4TCNQ molecule to be 0 for $V_G < -20V$

and 1 electron charge for $V_G > -20V$, in accordance with the molecular charge state found in previous experiments.[34] The diffusion barrier was then calculated for each of the three paths by taking the difference in total energy between the transition state geometry and the initial molecular adsorption geometry while restricting the charge.

The result of the gate-dependent diffusion barrier calculation is shown in Fig. 6.5 (a). For charged molecules path "T" has the lowest diffusion barrier (for the transition state geometry shown in Fig. 6.4 (b)). For charge neutral molecules, however, path "TR" has the lowest diffusion barrier (for the transition state geometry shown in Fig. 6.4 (e)). The calculated diffusion barrier for path "TR2" appears to be the highest of the three paths under all gate voltages. The position-dependent total energy of path "T" is plotted as a function of the diffusion path coordinates in Fig. 6.5 (b) for V_G=60V (charged case). The calculated diffusion barrier is 32 meV, which agrees reasonably well with the experimentally measured value of 23 meV. The "TR" path, on the other hand, has a more complex shape that exhibits two energy maxima situated at symmetric positions about the halfway point, with a calculated diffusion barrier of 51 meV. This value agrees reasonably with the experimentally measured diffusion barrier of 73 meV. The gate-dependence of the diffusion barrier for uncharged molecules has the correct trend but is much weaker than experimentally observed. This might be due to artificial constraints imposed on the charge transfer between the molecule and substrate in our calculations, which weakens the sensitivity of the total energy to applied electric fields. Such charge transfer effects are difficult to capture accurately using DFT.[110,111]

In order to clarify how much the three different diffusion paths each contributed to the total molecular diffusion, we transformed the experimental scatter plots shown in Fig. 6.3 into 2D histograms of the probability of a molecule jumping to each adsorption site from a starting bridge site (note that this does not directly tell us the diffusion path taken due to site overlap for the different paths). We then fitted the experimental data with a theoretical probability map produced via Monte Carlo simulation. The fit parameters for the Monte Carlo simulation were taken to be the probabilities for a molecule to take each of the three different diffusion paths. This process allowed us to extract the experimental probabilities for a molecule to take each different diffusion path. In Fig. 6.5 (c), (e), each colored bar represents an adsorption site (where the molecule's center aligns with a "bridge site"), while its shading denotes the experimental probabilities that a charged (Fig. 6.5 (c)) and neutral (Fig. 6.5 (e)) molecule starting from the origin lands on that particular "bridge" site after a current pulse. Fig. 6.5 (d), (f) shows the corresponding Monte Carlo fits for a charged (Fig. 6.5 (d)) and neutral (Fig. 6.5 (f)) molecule starting from the origin and jumping to different adsorption sites on the graphene lattice via the different diffusion paths. The molecular jumps in our simulations were uncorrelated to each other and the hopping probabilities of each of the 3 paths were adjusted until the squared difference between the experimental probability map and the simulated probability map converged to a minimum.

A comparison of Fig. 6.5 (c) and (d) suggests that the probability of a charged molecule taking path "T" as opposed to other paths is 98%. A comparison of Fig. 6.5 (e) and (f) suggests that the probability of a neutral molecule taking path "TR2" is the highest, at 48%, and the probability of a neutral molecule taking path "TR" is only 13%, despite DFT calculations indicating that path "TR" is the lowest energy path. Path "T", on the other hand, accounts for 39% of the jumps. Although the overall trend holds true that charged molecules move primarily by path "T", uncharged molecules appear to primarily move by path "TR2" instead of path "TR", which is contrary to the DFT predictions.

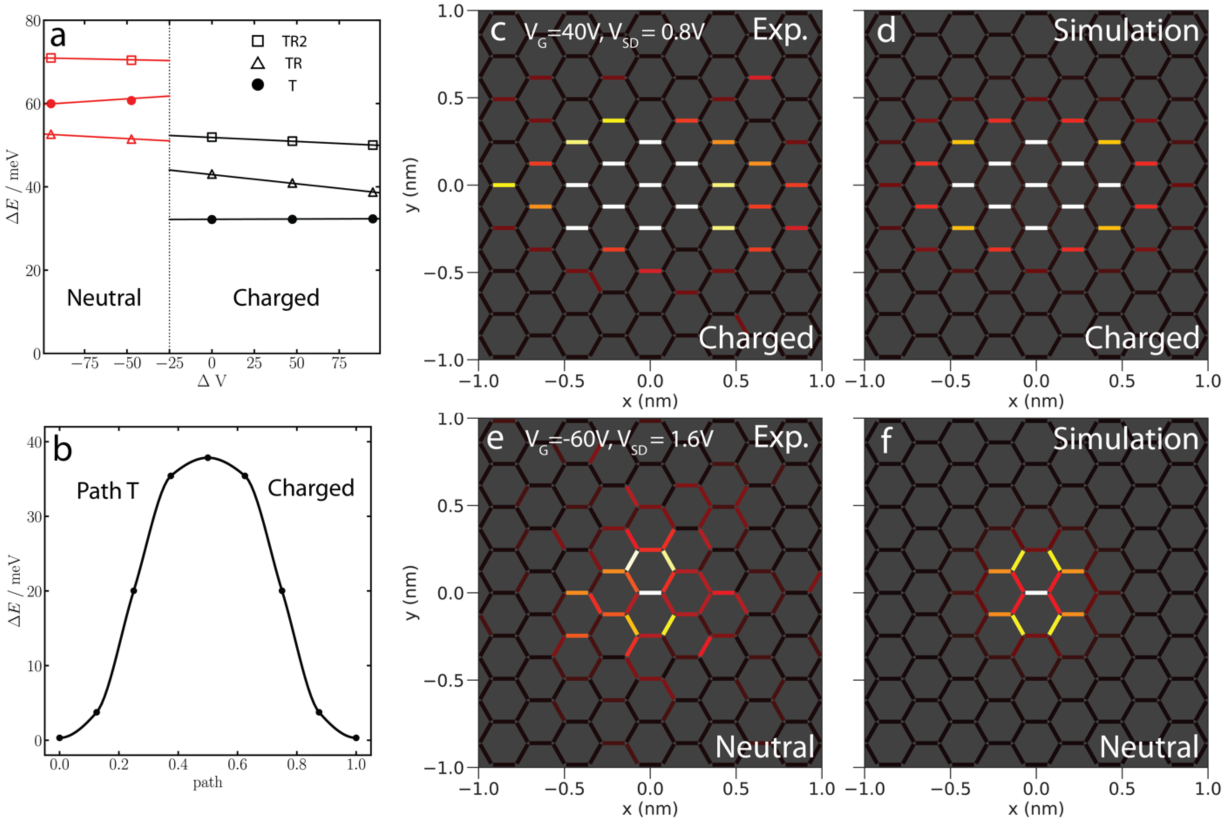

Fig. 6.5 Molecular diffusion barriers calculated from DFT and diffusion probability maps. (a) Diffusion barriers for the three diffusion paths ("T", "TR", "TR2") obtained from DFT for neutral molecules under conditions $V_G < -20\ V$ and for charged molecules under conditions $V_G > -20\ V$. (b) Diffusion barrier profile of path "T" for the charged molecule case. (c) Experimentally observed histogram of molecular jumps to each adsorption site under current pulsing conditions for $V_G = 40\ V$ and $V_{SD} = 0.8\ V$ (the charged molecule case). (d) Theoretical histogram of charged molecule jumps to each adsorption site using a Monte Carlo method fitted to the charged molecule data of (c). Molecules moving by path "T" constitute 98% of all molecules which have moved. (e) Experimentally observed histogram of neutral molecule jumps to each adsorption site under current pulsing conditions of $V_G = -60\ V$ and $V_{SD} = 1.6\ V$ (the neutral molecule case). (f) Theoretical histogram of neutral molecule jumps to each adsorption site using a Monte Carlo method fitted to the neutral molecule data of (e). Molecules moving to different adsorption sites by path "T", "TR", and "TR2" have respective probabilities of 39%, 13% and 48%.

6.5 Conclusion

We have demonstrated the ability to use an electrostatic gate to control the diffusion behavior of F_4TCNQ molecules on graphene. We find that the surface diffusion barrier is not only strongly dependent on gate voltage, but it also exhibits two different regimes depending on the charge state of the molecules. We attribute this difference to the distinct diffusion paths preferred by the molecules when they are charged versus when they are neutral. By tracking molecular motion with STM, we find that the preferred diffusion path of a charged molecule is a simple translation to a neighboring bridge site. The preferred diffusion path of a charge neutral molecule, on the other hand, involves a 60° rotation. DFT calculations of the diffusion barrier reasonably match experimentally determined values, but the preferred diffusion path for uncharged molecules does not match the DFT prediction.

7 Resonant Transport in molecule-decorated Graphene Devices

Ion-decorated graphene holds great promise for realizing low-power neuromorphic devices due to the tunability of graphene's conductance through chemical doping by adsorbed ions. Fine electrical control over lithium intercalation in graphene heterostructures has been successfully demonstrated,[112,113] and graphene synapses based on lithium electrochemical systems have also been fabricated.[78] In contrast to lithium-based technology, molecular ions have not yet been explored as an option for controlling the conductivity of graphene devices. Molecular ions are attractive for this application because of their relative low-cost of synthesis and their potential to be modified by functionalization.[114] Furthermore, since lithium orbital levels are far away from the graphene Fermi level, lithium modifies the graphene conductivity only by changing the carrier concentration and not through the formation of electrically resonant states on the graphene surface. Molecules such as F_4TCNQ, on the other hand, have resonances near the Fermi level that should strongly influence electron scattering in graphene, thereby causing significant conductivity changes. This phenomenon has not yet been reported for molecule/device systems with well-defined resonant scatterers.

In this chapter, I will present measurements of resonant scattering phenomenon observed in transport measurements of F_4TCNQ-decorated graphene transistors.

7.1 Introduction

Impurities on graphene are known to modify graphene conductivity by chemical doping and electron scattering. While scattering generally lowers the carrier mobility in graphene,[60,115] chemical doping can change the conductivity in either direction by modifying the carrier concentration. This can be implemented by impurities introduced to graphene through ion sputtering, ion deposition in vacuum, or ion intercalation in an electrochemical environment. Sputtering can effectively produce defects in graphene by knocking out carbon atoms as well as by ion implantation. However, sputtering is imprecise and creates a variety of different defects, leading to a range of different (and poorly controlled) electronic properties associated with different defects. Sputtering also irreversibly modifies the surface and is thus not ideal for information storage applications. Using deposited alkali ions as scatterers on graphene also suffers from similar problems of irreversibility. Once ions are deposited, their concentration on the graphene surface cannot be reversibly tuned, and adsorbed alkali ions can typically only be removed by annealing to high temperatures.

Electrochemical intercalation is a possible solution to achieve reversible and precise control over the conductivity of graphene. Lithium ions embedded in solid electrolytic polymers can be intercalated between graphene layers by applying voltages between a two-terminal graphene device and a counter electrode. Since lithium is an electron donor when adsorbed on graphene, the intercalated lithium concentration can be used to control the carrier concentration in graphene and thus its conductivity.[112,113] Such devices are useful for simulating neuronal plasticity since current pulses can be used to modify the device responsiveness to subsequent current pulses (*i.e.* the devices have "memory").[12,13,116]

Charge-carrying molecules can also perform a similar function, but they have not been as widely used to modify the conductivity of graphene. Here I will present transport measurements of the conductivity of F_4TCNQ-decorated graphene transistors where the surface molecule density can be reversibly controlled by an applied gate voltage. Scanning tunneling microscopy was used to characterize the surface molecular concentration, while two-probe differential conductance measurements were simultaneously used to monitor changes in the graphene conductivity. Using the device gate voltage to control when isolated molecules appear on the graphene surface provides control over when the resulting molecular resonance is observed in the graphene electrical conductance versus gate voltage characteristic curve. A plateau in the graphene conductance as a function of gate voltage is observed that can be explained by Fermi level pinning due to charge-tunable molecular LUMO states on the surface. We have developed a model that explains the conductivity of F_4TCNQ-decorated graphene based on Boltzmann transport theory that accounts for modifications to the graphene band structure due to the molecular LUMO resonance. The model captures experimentally observed features arising from molecular resonances and Fermi level pinning.

7.2 Methods

To measure the conductance of F_4TCNQ-decorated graphene devices, F_4TCNQ molecules were first deposited onto graphene FETs in ultra-high vacuum. Devices were then transferred into an STM held at a temperature of 4.5K. The experimental setup for measuring the conductance of the molecule-decorated device in the STM is shown in Fig. 7.1. To change the surface molecule density, a gate voltage V_{G-set} was applied to the device while simultaneously heating it with a diode heater on the STM stage. After allowing the molecular density to reach equilibrium for 180 s, the diode heater was turned off and the device was allowed to cool back down to 4.5K. The mechanism for changing the surface molecule density is described in detail in chapters 4 and 5. Heating the graphene device with the diode produces a more homogeneous distribution of single molecules on the surface compared to Joule heating the device using source-drain current (this is advantageous for observing sharper features in conductance measurements). After cooling the device to 4.5K, gate-dependent differential conductance measurements were performed by setting the DC voltage to $V_S = 0$ and applying a wiggle voltage V_{AC} of 20 meV to the source electrode. Switch S1 was then closed so that a lock-in amplifier connected in series to a current preamplifier could be used to detect the dI/dV_{AC} signal. The gate voltage was then ramped from -60V to 60V while recording dI/dV_{AC}.

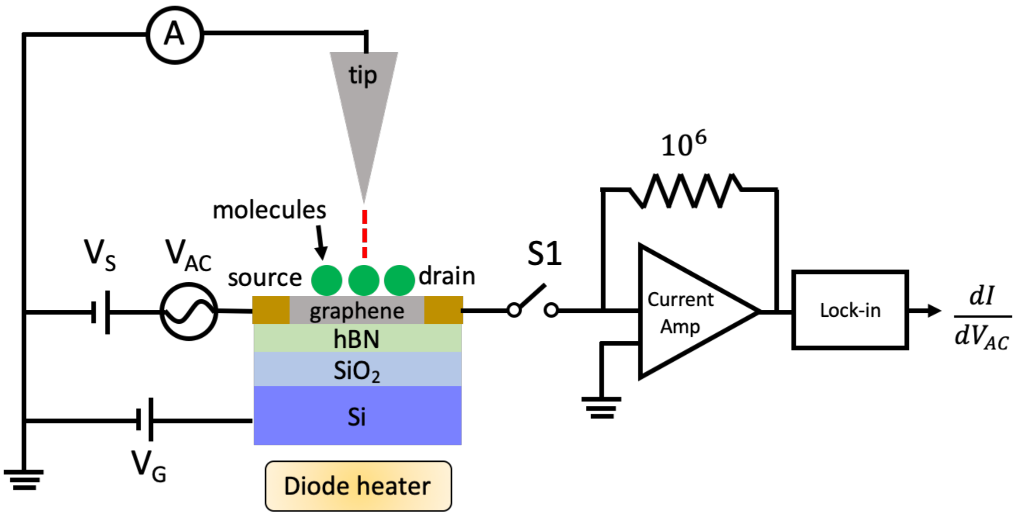

Fig. 7.1 Conductance measurement experimental setup. The surface molecule density of a molecule-decorated graphene device is adjusted by simultaneously applying a gate voltage V_{G-set} while heating the device with a diode heater. After the heater is turned off, a wiggle voltage V_{AC} is applied to the device and a lock-in amplifier is used to measure the differential conductance dI/dV_{AC} as a function of gate voltage V_{G-set}. V_S sets the sample/tip bias voltage.

7.3 Results

The surface molecule density obtained as a function of V_{G-set} is shown in Fig. 7.2. As expected from previous experiments, the surface molecule density varies roughly linearly with V_{G-set}. For this sample molecules start appearing on the surface near $V_G = 0V$ (this voltage can change due to impurity-induced offsets).

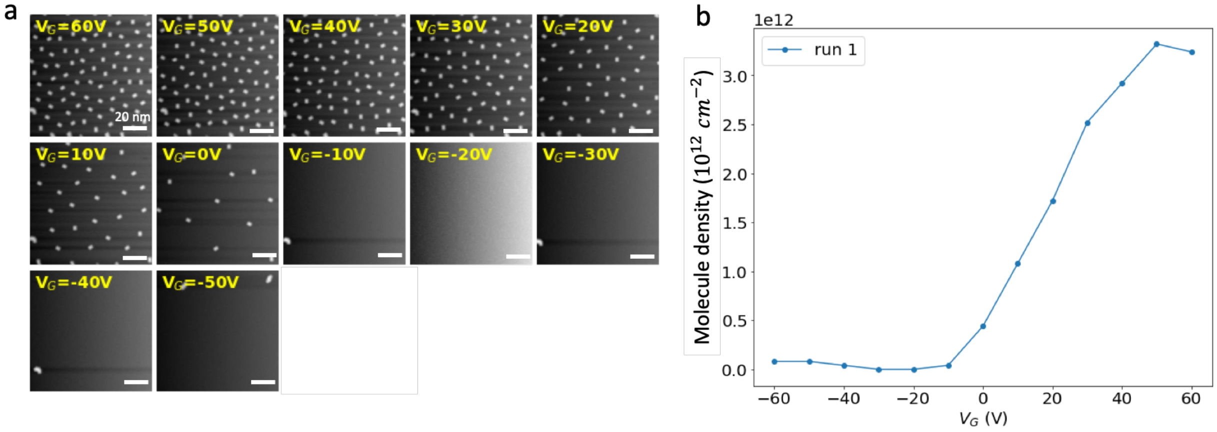

Fig. 7.2 Molecule density on graphene as a function of V_{G-set}. (a) STM topography of the graphene surface after setting the molecule density during a heating cycle with V_{G-set}. (b) Surface molecule density of the sample region shown in (a) as a function of V_{G-set}.

The gate-dependent conductance measured for the different molecular concentrations determined by each V_{G-set} is shown in Fig. 7.3 (a). For surfaces prepared under the condition $V_{G-set} \leq -10V$ (where the molecular concentration is near zero) the electrical conductance curves are very similar and exhibit a characteristic minimum conductivity when the Fermi level is at the graphene Dirac point near $V_G = 0$. Asymmetry in the electron and hole conductance indicates the existence of non-resonant impurities on the surface that skew the spectral weight by the mechanism explained in section 3.3.2. As V_{G-set} is increased to 0V (and charged molecules begin to populate the surface), we notice two features: (1) a dip appears near $V_G = -20$V in the device conductance, and (2) the minimum conductivity point shifts to the right. The gate voltage where the first dip occurs will be referred to as V_{LUMO} and the position of the minimum conductivity point will be referred to as V_D. As V_{G-set} is increased even further (causing more molecules to populate the surface), we notice that the dip at V_{LUMO} deepens and widens, and spans a larger range in V_G. The position of V_D also shifts to the right with increasing V_{G-set}. The difference between V_D and V_{LUMO} is plotted as a function of the surface molecule density in Fig. 7.3 (c).

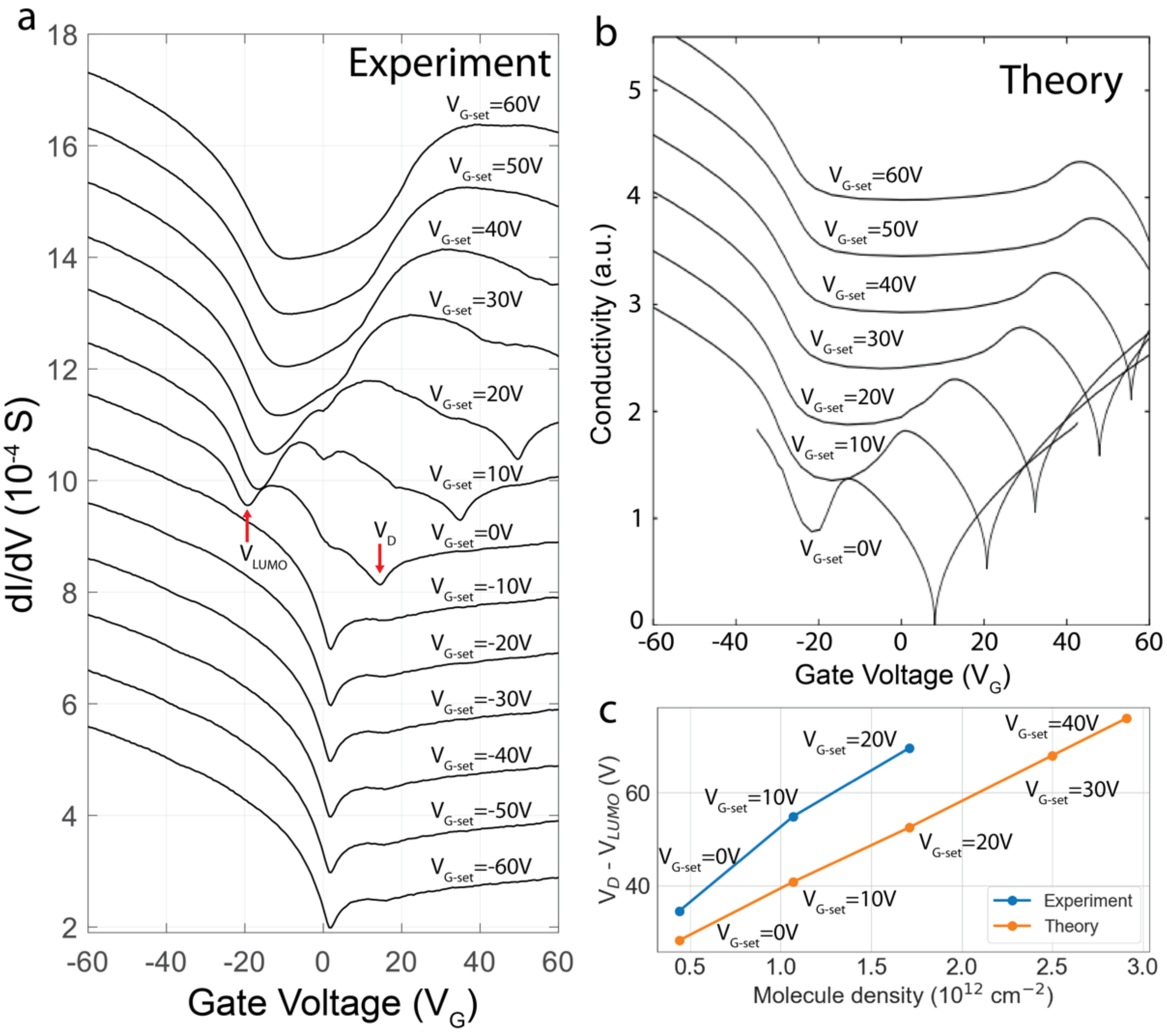

Fig. 7.3 Gate-dependent conductivity of a F_4TCNQ-decorated graphene device as a function of $\mathbf{V_{G-set}}$. (a) The gate-dependent conductance of the device is plotted as a function of the setting gate voltage V_{G-set} (which determines the molecular concentration). Molecules appear on the surface for $V_{G-set} \geq -10V$ and a molecule resonance becomes visible at $V_G = -20V$. Fermi level pinning due to the molecular LUMO states is responsible for shifting spectral features to the right. (b) Theoretical conductivity of the graphene-molecule system calculated using Boltzmann transport theory. The molecule resonance and the shift of spectral features qualitatively match experimental observations. (c) The gate voltage difference between V_D and V_{LUMO} is plotted as a function of the surface molecule density. $V_D - V_{LUMO}$ is roughly linear in surface molecule density.

7.4 Discussion

In order to explain these observations we use the model developed in section 3.3.3 to calculate the gate-dependent conductivity. Here we utilize the impurity band structure resulting from the continuum model of section 3.3.3. The electrical conductivity can be calculated from the band velocity and the Fermi wavevector using (3.77), assuming that the scattering time constant τ is independent of energy or band index. While this is only an approximate model, the density of states contributed by the molecular resonance is reasonably captured in the model. To compare the conductivity between theory and experiment, we plot it as a function of gate voltage (similar to Fig. 3.11 (b)) instead of Fermi energy (as shown in Fig. 3.11 (a)). To convert Fermi energy to carrier density we first find the reference Fermi level ε_F^{CN} that corresponds to charge neutrality for the molecule-decorated graphene system, corresponding to a density of states $g(\varepsilon)$. Since molecules take electrons from the previously charge neutral graphene, which has a density of states $g_G(\varepsilon)$, the total electron density counting from a given energy ε_{min} is then

$$\int_{\varepsilon_{min}}^{0} g_G(\varepsilon)d\varepsilon = \frac{\varepsilon_{min}^2}{\pi\hbar^2 v_F^2} = \int_{\varepsilon_{min}}^{\varepsilon_F^{CN}} g(\varepsilon)d\varepsilon\,. \tag{7.1}$$

Next, the carrier density n relative to the charge neutral system can be defined using

$$n = \int_{\varepsilon_F}^{\varepsilon_F^{CN}} g(\varepsilon)d\varepsilon\,, \tag{7.2}$$

where ε_F is the Fermi level. Finally, the carrier density is converted to a gate voltage using $V_G = n/C$, where the device geometric capacitance is $C = 6.5\times 10^{10}$ electron charges $\mathrm{cm}^{-2}V^{-1}$.

The calculated conductivities for realistic values of the surface molecule density are plotted in Fig. 7.3 (b). The theoretical results exhibit key features similar to the experiment as follows: (1) a dip in conductivity near $V_{LUMO} = -20V$, and (2) shifting of spectral features to higher gate voltage for increased molecular density. The theoretical difference between V_D and V_{LUMO} for different surface molecule densities is also found to vary linearly with the surface molecule density (Fig. 7.3 (c)). This can be explained by the fact that each single molecular orbital hosts one electron, thus more charge is needed to raise the Fermi level for a higher surface molecule density. The total density of electrons needed to raise the Fermi level from the molecular orbital to the Dirac point is equal to the charge density $C(V_D - V_{LUMO})$, which can be expressed as

$$C(V_D - V_{LUMO}) = n_M + n_0, \tag{7.3}$$

where n_M is the surface molecule density and $n_0 = \frac{|E_D - E_{LUMO}|^2}{\pi\hbar^2 v_F^2}$ is the integrated graphene density of states between the Dirac point energy and molecular orbital energy. Since $n_M = CV_{G-set} + n_0$ from Eq. (4.5), we have

$$V_D - V_{LUMO} = V_{G-set} + \frac{2n_0}{C}, \tag{7.4}$$

which predicts that $V_D - V_{LUMO}$ varies linearly with V_{G-set} with a slope of 1. The experimentally measured $V_D - V_{LUMO}$ is seen to be ~30% higher than this predicted value. It is possible that this is due to inhomogeneity in the device capacitance, where fringing fields can cause the average device capacitance to become higher near the edges of the graphene sheet. Nevertheless, it is clear that the Fermi level pinning effect observed in the conductivity is explained by the extra quantum capacitance introduced by the presence of isolated molecules on the surface.

7.5 Conclusion

In conclusion, we are able to correlate changes in the microscopic distribution of molecules on a graphene device to changes in the device's macroscopic transport properties. In particular, a reduction in conductivity due to the molecular resonance is observed as the local molecular density is increased. Pinning of the Fermi level by molecular LUMO states is also observed through a plateau in conductivity over a wide range of gate voltages. The gate voltage range over which the Fermi level is pinned is observed to vary linearly with the surface molecular density, in agreement with theoretical predictions based on Boltzmann transport. The sharp features observed in the device conductivity suggests that changes in the surface molecular concentration is reasonably uniform over a macroscopic scale.

8 Electromigration of single-molecule adsorbates

The previous chapter showed that molecular resonances reduce the conductivity of graphene due to electron-molecule scattering, but these same scattering processes can also induce a force that pushes molecules across the device surface. The force resulting from electrons scattering off an impurity under current flow was first related to electrical conductivity in a jellium model by Das and Peierls and called a “wind force”.[117] Such a force is capable of moving atoms and molecules in well-specified directions, producing a phenomenon called electromigration.

In this chapter I present a study of electromigration forces on isolated F_4TCNQ molecules at the surface of a graphene device.

8.1 Introduction

Electromigration is the current-driven migration of atoms or impurities in a conductor over time. Even though electromigration forces are typically very small, they cause insidious damage to microelectronic devices through the cumulative effects of current flow, eventually leading to breakage of thin conductor wires and device failure. It is thus important to understand this force in order to ameliorate its effect in device applications. On the other hand, electromigration forces also present opportunities for fabricating nanogap devices for actuating nanomechanical systems, and for facilitating nanoengineering.[118] Numerical methods have been used to model the fundamental electromigration properties of single impurities,[119,120] but experimentally measuring those properties for individual atoms or molecules has never been done. One reason this is hard is the difficulty of combining devices and atomically-resolved microscopy. Another reason is the local inhomogeneity of electric fields at the microscopic scale which makes it challenging to measure electric field directions and magnitudes at any given point in a driven adsorbate’s trajectory. Although macroscopic experiments have been used to estimate electromigration forces by measuring the average transport rate of ensembles of impurities,[42,65,66] the detailed structure of these impurities is unknown, and so the obtained electromigration force is an average quantity. Some attempts have been made to quantify electromigration forces at the nanoscale, but even the smallest electromigrating object reported to date is ~100 nm in size and composed of hundreds of thousands of atoms.[23]

Here we study the electromigration of single F_4TCNQ molecules at the surface of a graphene FET. Scanning tunneling microscopy was used to image molecular motion after passing source-drain current through the device to induce electromigration in molecules. Scanning tunneling potentiometry (STP) was used to determine the average electric field direction in nearby regions of the device so that the electron flow direction could be identified. We find that molecules move in the same direction as the electron flow (opposite to the current) even though the current carriers are holes under our experimental conditions. Our experimental results indicate that the electron wind force dominates over the direct force by a factor of ~200 in driving the motion of molecules across a graphene surface. The direction of molecular motion is explained intuitively by strong inter-cone scattering in graphene induced by the rapidly oscillating potential of the molecule, which causes large momentum transfer to molecules in the direction of electron motion. The role of inter-cone scattering is important because if only intra-cone scattering were permitted (as in the case of slowly varying potentials), then momentum transfer should push the molecules in the direction of hole motion. Force calculations using a non-equilibrium Green's function (NEGF) method confirm this intuitive picture of electromigration, and yields detailed real-space information about charge redistribution and the local forces induced by current flow.

8.2 Methods

F$_4$TCNQ molecules were deposited onto a graphene FET in ultra-high vacuum which was then transferred into an STM held at 4.5K. The surface molecule density was set using the gate-voltage procedure described in previous chapters to prepare a desired surface molecule density. A schematic of the procedure used to induce and observe electromigration of molecules is shown in Fig. 8.1. A STM scan of the surface is taken before applying the source-drain current required to induce electromigration, as shown in Fig. 8.2 (a). The STM tip is then withdrawn $\sim 2\mu m$ from the surface and a source-drain current pulse lasting ~10s is applied to the device to induce electromigration. A gate voltage of $V_G = -20$ V is typically applied to the device during the electromigration current pulse to ensure that molecules remain uncharged and do not interact strongly with each other via Coulomb repulsion during the electromigration. This also ensures that the graphene is unambiguously in the p-doped regime, as shown in chapter 4. After the source-drain current is turned off the STM tip is re-approached onto the same area of the surface and another scan is taken to visualize the resulting surface molecular configuration. The drift of the scan frame between individual scans is very minimal (typically less than 0.1 nm) and can be neglected.

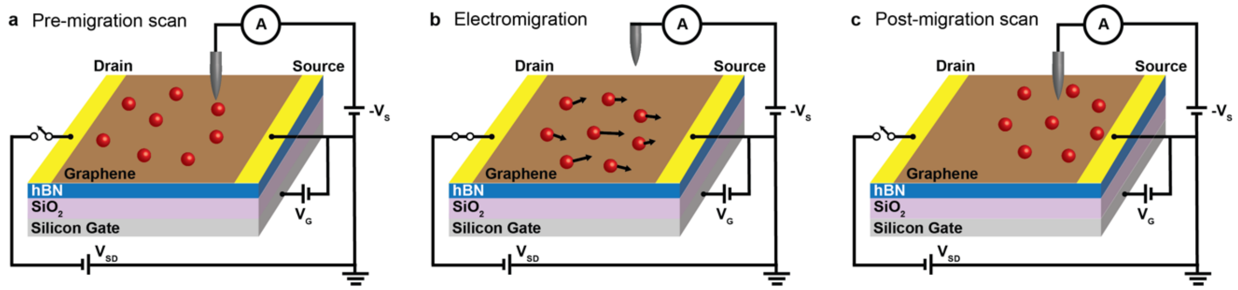

Fig. 8.1 Electromigration experimental setup. (a) F$_4$TCNQ molecules deposited onto a graphene FET are first imaged with a STM to determine initial molecular positions. (b) The STM tip is withdrawn, and a source-drain voltage V_{SD} is subsequently applied to the device, causing current to flow through the graphene and molecules to electromigrate. (c) After V_{SD} is turned off, the STM tip is re-approached onto the surface, and another image is taken to determine the movement of individual molecules.

8.3 Results

Some examples of surface molecular configuration changes are shown in Fig. 8.2 (a)-(d) and (e)-(h). Fig. 8.2 (b)-(d) show the surface molecular configuration after consecutive positive polarity source-drain current pulses were applied to the device for 20 to 90 s, where $V_{SD} = 0.5$ V and $I_{SD} = 240\ \mu A$. The molecules are observed to move towards the lower left corner of the image, the direction of electromigration. Fig. 8.2 (f)-(h) show the surface molecular configuration after consecutive negative polarity source-drain current pulses were applied to the device for 30 to 340 s, where $V_{SD} = -0.5$ V and $I_{SD} = 240\ \mu A$. The molecules can be seen moving towards the top right corner, the direction of electron flow for this opposite polarity bias. The direction of molecular motion is clearly current-polarity dependent, with molecules impeding each other and aggregating into clusters, thus resembling a traffic jam.

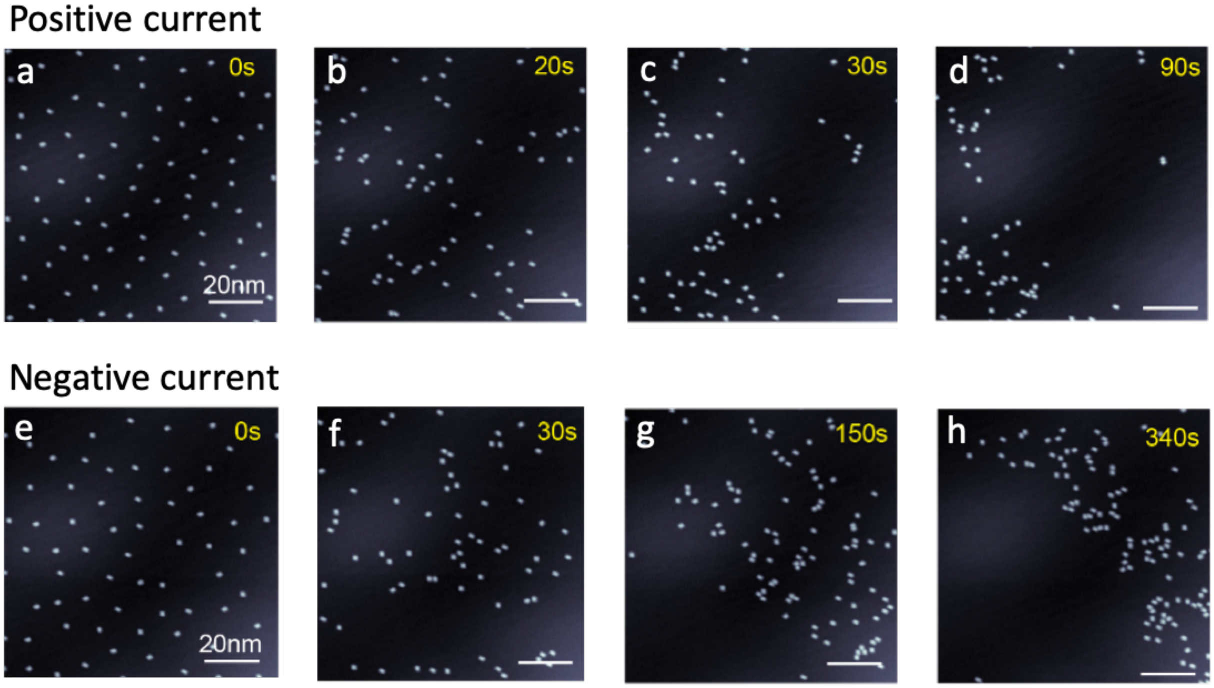

Fig. 8.2 Current-polarity dependent migration of molecules. (a)-(d) STM topography images of the surface molecular configuration evolution after a series of positive-polarity source-drain current pulses ($V_{SD} = 0.5$ V and $I_{SD} = 240\ \mu A$) were applied to the device. The duration of the current pulses are indicated in the top right corner of the images. (e)-(h) The surface molecular configuration evolution after a series of negative-polarity source-drain current pulses ($V_{SD} = -0.5$ V and $I_{SD} = 240\ \mu A$) were applied to the device. Molecules can be seen moving towards opposite directions for positive-polarity current and negative-polarity current. In both cases the molecules are moving in the direction of electron flow.

In order to study the electromigration of individual molecules isolated from the effects of other molecules, the surface molecule density was tuned to a lower value of $\sim 2 \times 10^{11}\ cm^{-2}$ via the method described in chapter 4. This allowed identification of individual molecule trajectories via particle tracking software[109] in STM images taken before and after the current pulse. To compare electromigration behavior for different values of V_{SD}, 15 current pulsing and imaging cycles were applied to the device for each value of V_{SD}, and an ensemble average molecular velocity was calculated over the duration of the electromigration current pulses from the resulting particle trajectories. Examples of molecular trajectories obtained after applying the electromigration pulse cycles are shown in Fig. 8.3. Fig. 8.3 (a) shows molecular trajectories after a series of source-drain current pulses where a negative source-drain voltage of $V_{SD} = -0.42$

V, I_{SD} = 100 μA was applied. On average, molecules are seen to drift to the top left corner, but the motion resembles a biased random walk. Fig. 8.3 (b) shows molecular trajectories after a series of source-drain current pulses with opposite polarity where the source-drain voltage used was V_{SD}= 0.51 V, I_{SD} = 120 μA. In this case molecules are observed to drift in the opposite direction, towards to bottom right. Similar behavior was seen for multiple graphene FET devices.

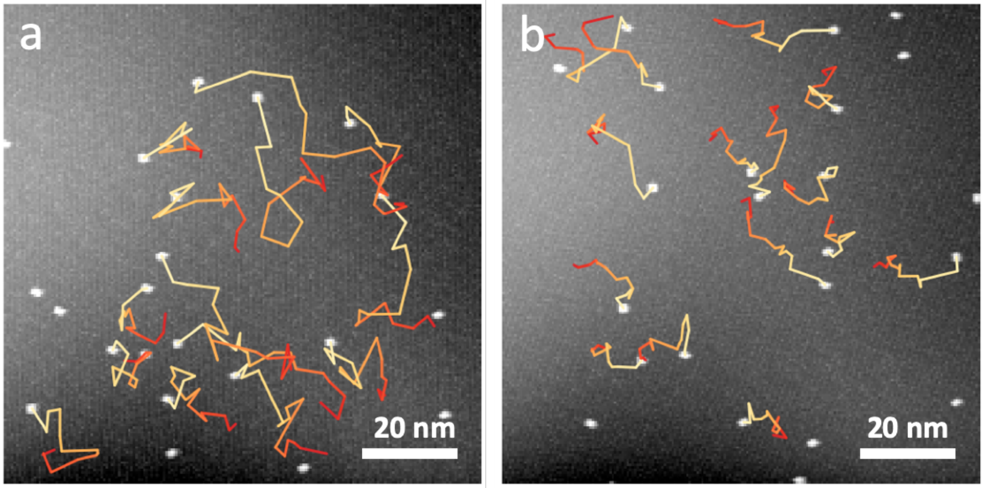

Fig. 8.3 Molecular trajectories during electromigration. Molecular trajectories are shown for electromigration experiments performed under (a) V_{SD}=-0.42V, I_{SD} = 100 μA and (b) V_{SD}=0.51V, I_{SD} = 120 μA. A current pulse of 60s was passed through the graphene device before each scan frame was taken. Molecules display current polarity-dependent motion in the direction of electron flow.

Fig. 8.4 shows the average drift velocity and diffusion constant of all molecules within a single scan window as a function of V_{SD}. The average displacement vector of all molecules in the scan window between every two consecutive scans is plotted as an arrow and connected head-to-tail to indicate the average displacement of the molecules, as shown in Fig. 8.4 (a), (b). The average drift velocity is calculated by dividing the average molecular displacement by the duration of active current through the device (typically 60 s). For negative V_{SD}, as shown in Fig. 8.4 (a), the total length of the arrows increases as the magnitude of the applied source-drain voltage is increased, and the average direction of motion is towards the top left. For positive V_{SD}, as shown in Fig. 8.4 (b), the total length of the arrows also increases as the magnitude of the applied source-drain voltage is increased, and the average direction of motion is towards the bottom right. All arrows are approximately collinear, indicating that the average molecular drift velocity is time-independent. Fig. 8.4 (c),(d) indicate that the magnitude of the average drift velocity increases exponentially with applied V_{SD}. The diffusion constant of the molecular motion D was obtained by subtracting the average drift from the molecular motion and then fitting the mean square displacement of the drift-corrected molecules using Eq. (6.1).

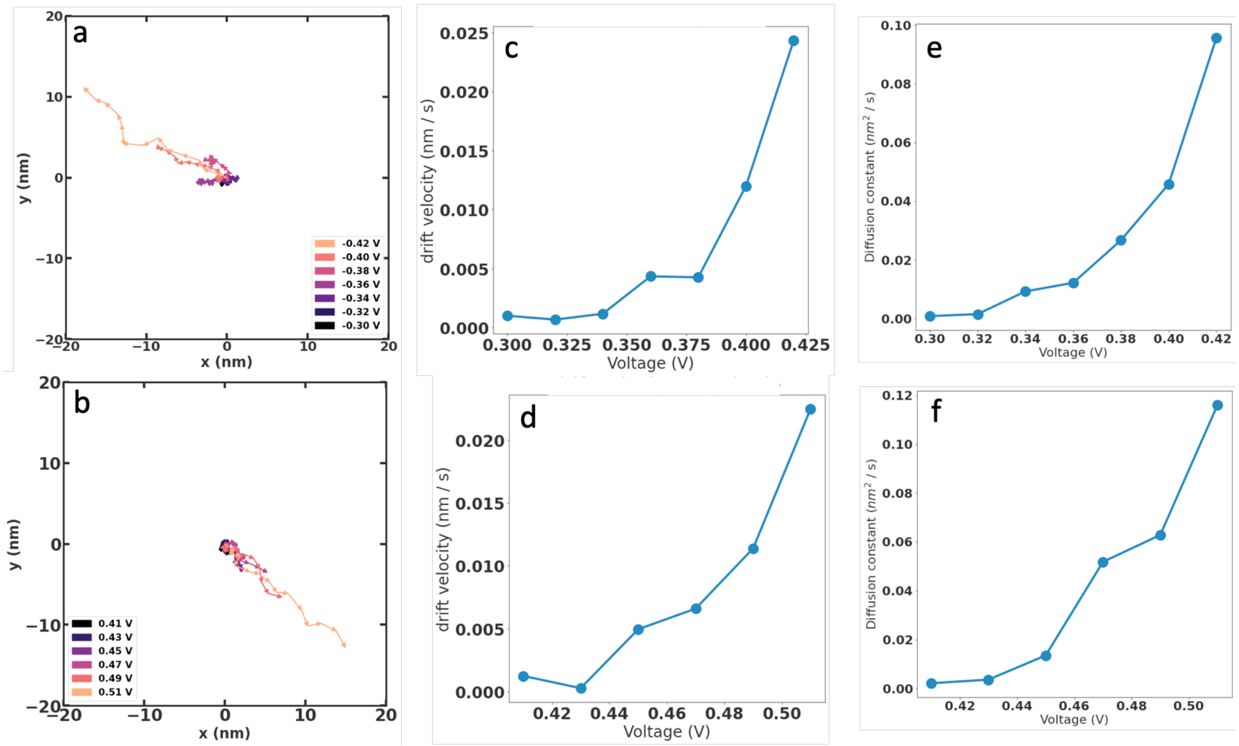

Fig. 8.4 Average drift velocity of molecules. (a)-(b) The average drift velocity of all molecules between two consecutive scans are plotted as an arrow and connected head-to-tail to indicate the average direction and magnitude of motion, for (a) negative V_{SD} and (b) positive V_{SD} applied to the device. (c)-(d) The average magnitude of the drift velocity is shown as a function of V_{SD} for (c) negative V_{SD} and (d) positive V_{SD}. (e)-(f) The average diffusion constant is shown as a function of V_{SD} for (e) negative V_{SD} and (f) positive V_{SD}.

In order to correlate molecular motion with the local in-plane electric field, we mapped out the local electrochemical potential gradient using STP. Fig. 8.5 (a)-(d) show a series of STP measurements under applied V_{SD} taken close to the area where electromigration of single molecules was measured. The in-plane electric field was extracted by fitting a plane to the potential maps for each V_{SD} applied and determining the gradient. It was found that for positive V_{SD} electrons move towards the bottom right of the scan frame, whereas for negative V_{SD}, electrons move towards the top left of the scan frame, thus the molecules were found to move in the same direction as electrons. Fig. 8.5 (e) shows the magnitude of the fitted in-plane electric field as a function of V_{SD}. The in-plane electric field is roughly linear to the applied V_{SD}, as expected for a device with Ohmic contacts. The value of the in-plane electric field was found to be ~5 $\mu V\ nm^{-1}$ for every 1 V of V_{SD} applied.

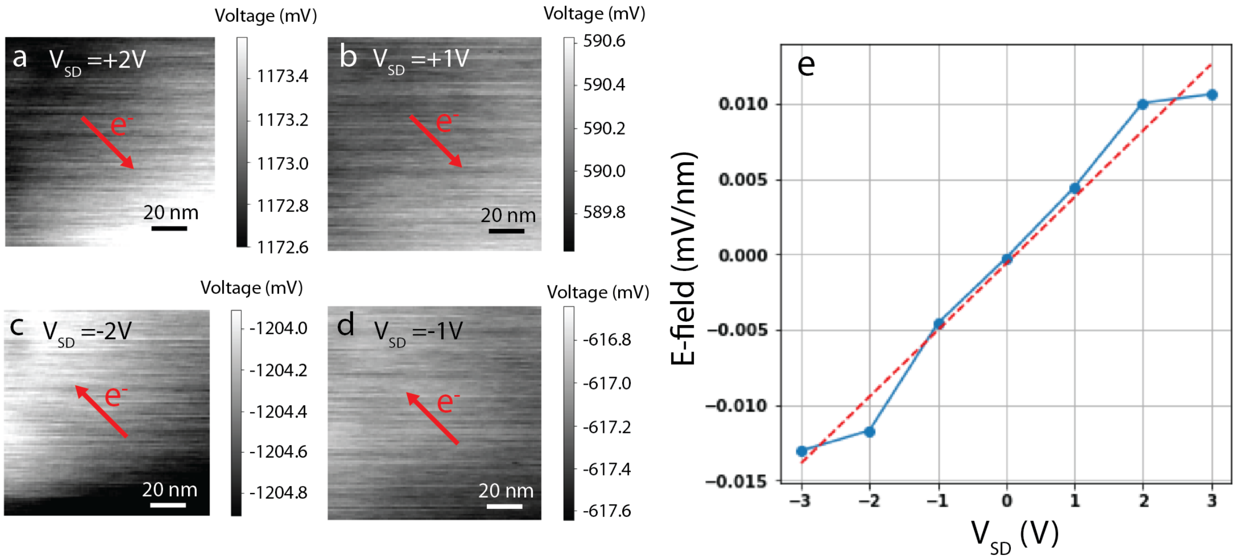

Fig. 8.5 Scanning tunneling potentiometry measurement of the in-plane electric field. (a)-(d) STP potential maps of the graphene device surface, taken at a location on the device near the location of the electromigration experiments. A V_{SD} of (a) 2V, (b) 1V, (c) -2V, (d) -1V was applied to the device. For positive V_{SD}, electrons move towards the bottom right, whereas for negative V_{SD}, electrons move towards the top left. (e) Magnitude of the electric field as a function of V_{SD}.

8.4 Discussion

To obtain the magnitude of the total electromigration force F_{total}, we make use of the Einstein relation $D = \mu k_b T$, which relates the diffusion constant D to the mobility of the molecules $\mu = v_d / F_{total}$ and temperature T, where v_d is the molecular drift velocity. The total force can then be found using

$$F_{total} \equiv \frac{v_d}{\mu} = \frac{k_b T v_d}{D}, \tag{8.1}$$

where k_b is the Boltzmann constant. For an applied V_{SD} of -0.42V, the diffusion constant is found to be 0.096 $nm^2 s^{-1}$ and the drift velocity is 0.025 $nm\ s^{-1}$. Under a temperature of 20K, the estimated total force on the molecule is found to be 0.07 pN.

The effective valence Z^* of the molecule, defined as the ratio between the total force and the applied electric field, can be calculated using

$$Z^* \equiv \frac{F_{total}}{eE}. \tag{8.2}$$

Using an electric field of $E \approx 2.1\ \mu V\ nm^{-1}$ under V_{SD}=-0.42V, we find that the effective valence of F_4TCNQ is $Z^* \approx 200$. Since the highest direct force the electric field can apply on a charged molecule is at most eE, a Z^* of 200 suggests that the wind force is ~200 times stronger than the direct force.

We now turn our attention to explaining the direction of the wind force. In a normal p-doped semiconductor with parabolic bands, where the Fermi surface is near the Γ point, and all scattering is limited to the first Brillouin zone (a good approximation for slowly varying potentials), as illustrated in Fig. 8.6, the wind force can be calculated as a sum of scattering processes[64,121]

$$\langle \mathbf{F}_W \rangle = -\sum_{k,k'} \hbar(\mathbf{k}' - \mathbf{k}) \frac{2\pi}{\hbar} \left|\widetilde{U}_{k'k}\right|^2 [1 - g(\mathbf{k}')] g(\mathbf{k}) \delta(\mathcal{E}_{k'} - \mathcal{E}_k) \quad , \tag{8. 3}$$

where $\widetilde{U}$ is the screened adsorbate-graphene potential, $g(\mathbf{k})$ is the non-equilibrium distribution function as defined in (3.72), and the delta function $\delta(\mathcal{E}_{k'} - \mathcal{E}_k)$ ensures elastic scattering. This expression has an intuitive interpretation: the wind force on the adsorbate is just the opposite of the momentum change $\hbar(\mathbf{k}' - \mathbf{k})$ of the incoming electron. In this model electrons scattering off a potential in a crystal are similar to free electrons scattering off a potential in vacuum, in that the momentum change of electrons is equal to their change in crystal momentum $\hbar(\mathbf{k}' - \mathbf{k})$. Since there are more left-going filled states and more empty right-going empty states, this model predicts that the force pushing on an adsorbate will be in the same direction as the electric field, hence a hole-wind emerges.

The scattering process in graphene is more complicated because large momentum transfers can occur if inter-cone scattering is allowed. For instance, a scattering event with a large momentum transfer is shown in Fig. 8.6. The scattering wavevector illustrated corresponds to a momentum transfer that now pushes the adsorbate in the opposite direction of the electric field. To calculate the total force, one must sum over all scattering processes for every $\mathbf{k}$ and $\mathbf{k}'$ pair in reciprocal space, each scattering weighted by the matrix element $\left|\widetilde{U}_{k'k}\right|^2$. If the adsorbate potential has large Fourier components on the order of $1/a$, where a is the graphene lattice constant, the total wind force produced may redirect opposite the direction of the electric field, creating an electron-wind force in the direction of electron flow. Moreover, backscattering in graphene is suppressed between different valleys and pseudospins if the scattering potential does not break the sublattice symmetry. The direction of the final wind force obtained by summing over these factors is thus not immediately clear and can depend on details of the adsorbate potential. For an extended object like an organic molecule, the potential varies on the same scale as the graphene lattice and we thus expect substantial scattering amplitudes on the order of $1/a$.

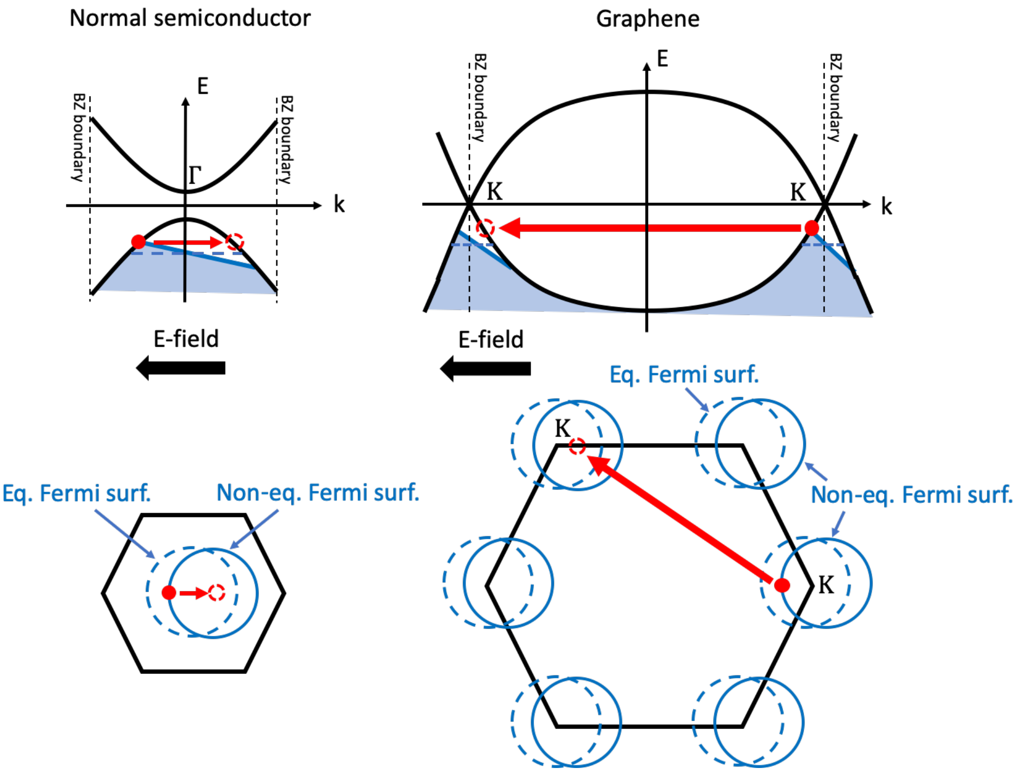

Fig. 8.6 Schematic of electron scattering processes in a normal semiconductor and graphene. Electron scattering in a semiconductor and in graphene is visualized. For a normal semiconductor with scattering only in the first Brillouin zone, a hole-wind is predicted. For graphene, large scattering wavevectors can lead to the emergence of an electron-wind even in the hole-doped limit.

In order to precisely calculate the total force on F_4TCNQ molecules we performed a NEGF calculation for F_4TCNQ-decorated graphene.[120] The two-electrode DFT-NEGF calculation (performed by M. L. Cohen's group) was set up over a finite unit cell in the x-direction, as shown in Fig. 8.7 where a finite bias difference V is applied between the left and right electrodes, and electrons flow towards to +x direction. Periodic boundary conditions were used in the y-direction. The electronic contribution to the force on the atom located at position $\mathbf{R}_i$ can be calculated using

$$\mathbf{F}_i(V) = -Tr[\hat{\rho}(V)\frac{\partial \hat{H}(V)}{\partial \mathbf{R}_i}] \;, \tag{8. 4}$$

where $\hat{H}(V)$ is the electronic Hamiltonian, and $\hat{\rho}(V)$ is the electronic density matrix element at finite bias V. The current-induced non-equilibrium atomic force is then $\mathbf{F}_{neq,i}(V) = \mathbf{F}_i(V) - \mathbf{F}_i(V = 0)$.[69,70,122] By summing the force on all atoms in the molecule, the total electromigration force can be calculated.

$$\mathbf{F}_{EM}(V) = \sum_{i\in adsorbate} \mathbf{F}_{neq,i}(V) \;. \tag{8. 5}$$

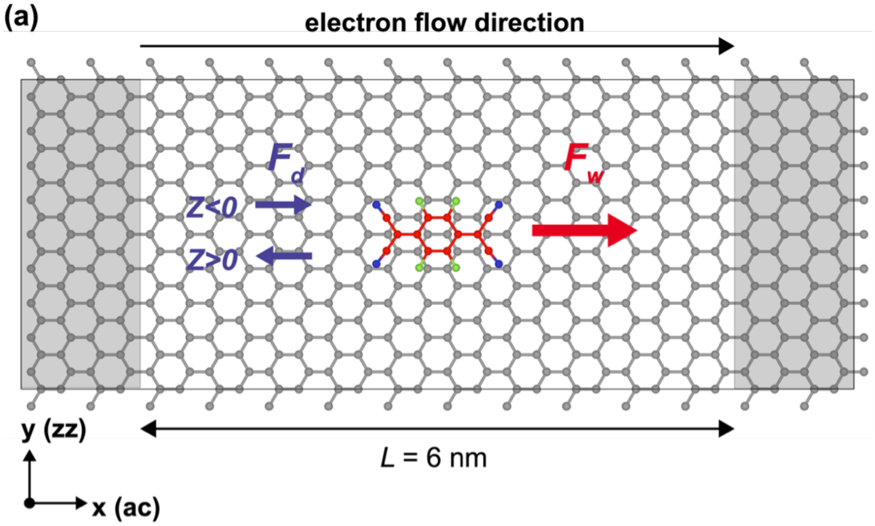

Fig. 8.7 Atomic structure used in the DFT-NEGF calculation. The atomic structure of an F_4TCNQ molecule adsorbed on graphene is shown. The shaded regions indicate electrode regions. The chemical potential is raised by $eV/2$ at the right electrode and lowered by $-eV/2$ at the left electrode so that electrons flow towards the +x direction. Adapted from ref. [120].

In the low-bias regime the wind force can be reduced to the form[69,70]

$$\langle \mathbf{F_W} \rangle = -\int \delta\rho(\mathbf{r}) \nabla_{\mathbf{R}_i} v^l(\mathbf{r})\, d\mathbf{r} - \sum_{jk} \Delta\rho_{jk} \langle \phi_j | \nabla_{\mathbf{R}_i} v_{ps}^{nl}(\mathbf{r}) | \phi_k \rangle \,, \tag{8.6}$$

where $\nabla_{\mathbf{R}_i} v^l(\mathbf{r})$ is the gradient of the local part of the DFT potential, $\nabla_{\mathbf{R}_i} v_{ps}^{nl}(\mathbf{r})$ is the gradient of the non-local part of the pseudopotential, and $|\phi_i\rangle$ is the pseudo-atomic orbital basis for electron wavefunctions. In order to gain some insight into the microscopic origin of the wind force, we can roughly divide the current-induced charge density $\delta\rho$ into two components $\delta\rho = \delta\rho_1 + \delta\rho_2$, where $\delta\rho_1$ and $\delta\rho_2$ represent the induced electron charge density residing in the graphene substrate and in the molecule, respectively. These induced charge densities are plotted in Fig. 8.8. We note that $\delta\rho_1$ (the induced electron density in graphene) piles up around the molecule on the upwind side of the electron flow (the -x side) and decreases on the downwind side of the electron flow (the +x side). This feature is known as the Landauer dipole, or the residual resistivity dipole, and is considered to be the fundamental source of resistivity at the microscopic scale. $\delta\rho_2$, on the other hand, can be thought of as a screening response of electrons within the molecule to the outside charge build-up $\delta\rho_1$. The local polarizability of the molecule causes this second dipole to form on the molecule opposite the direction of the Landauer dipole. The distribution of $\delta\rho_2$ thus has a deficiency of electrons in the -x direction and a surplus of electrons in the +x direction, which produces a force in the +x direction on positively charged ions at the center of $\delta\rho_2$. This means that the molecule experiences a force pointing in the direction of electron flow (an electron wind force).

We find that the wind force dominates the direct force by 1 to 2 orders of magnitude. However, comparison of the calculated wind force magnitude to experiment is only approximate. For a current density of $\sim 3\ A/m$ (estimated from a total current of 100 μA over the device width of 30 μm), the calculated total force is $\sim 1.6\ pN$. This is roughly an order of magnitude larger than the experimentally estimated force of 0.07 pN. It is possible that this discrepancy stems from inaccurate estimation of the graphene current density since electrons are assumed to travel ballistically in the NEGF calculation. In reality the graphene conductivity is influenced by scattering with defects in the device substrate, which likely decreases the total force due to decreased current density.

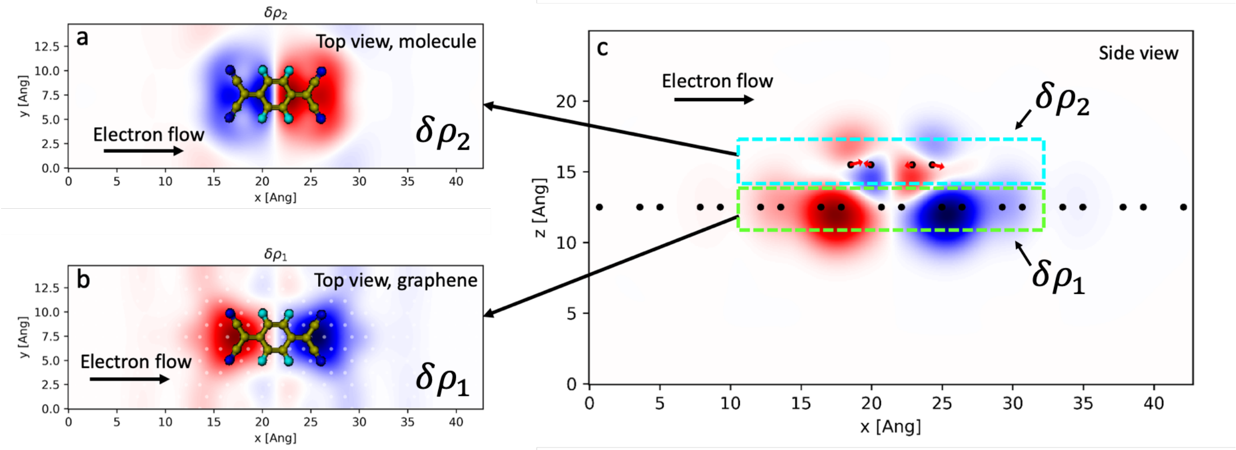

Fig. 8.8 Calculated charge distribution obtained from NEGF. The integrated nonequilibrium electron charge density distribution is plotted (a) within a ± 1.5 Å range from the molecular plane for $\delta\rho_2$ (top view), and (b) within a ± 1.5 Å range from the graphene plane for $\delta\rho_1$ (top view), and (c) along the length of the molecule (side view). Red represents excess electron density and blue represents electron density deficiency. In the graphene layer electrons can be seen piling up on the upwind side of electron flow with a deficiency on the downwind side. This corresponds to the Landauer dipole. The electron density on the molecule itself has opposite polarity to the Landauer dipole and induces an electron wind force towards +x for the positively charged ion cores. Here the charge density has been smeared with a Gaussian function with standard deviation = 0.15 Å to emphasize the polarization. Calculations performed by Y. W. Choi.

8.5 Conclusion

In conclusion, we have demonstrated the ability to simultaneously control and image electromigration of single molecules on a graphene FET by delivering source-drain current pulses to the device and using a STM to image the resulting molecular motion. The direction of molecular motion is consistent with an electron-wind force, even though the graphene charge carriers are holes under experimental conditions. Graphene band structure effects and strong inter-cone scattering induced by the molecule potential explain the direction of momentum transfer to the molecules. NEGF was used to visualize the nonequilibrium charge distribution around the molecule, which also confirms the direction of the experimentally observed electromigration. Lastly, the magnitude of the electromigration force was estimated by evaluating the Einstein relation with the observed average electromigration velocity and diffusion constant.

9 Conclusion

To conclude, I have presented several different ways of controlling molecular motion at the atomic scale, including tuning the density of molecular adsorbates through Fermi level pinning, tuning the molecular phase by controlling the charge state of the molecules, tuning the diffusion barrier through electrostatic gating, and using in-plane current to drive electromigration of molecules. The techniques for controlling molecules demonstrated in this dissertation are not only generally reversible, but also drive device-scale changes of the surface molecular distribution, enabling us to directly correlate local images of the surface obtained by STM to global changes in device properties (such as conductivity). It was found that the ability to change the charge state of adsorbed molecules is a useful tool for exerting molecular control because it changes the inter-molecular Coulomb interaction and can lead to dramatic changes in the surface molecular distribution. Force and momentum were also found to transfer non-trivially for a molecular scatterer experiencing electromigration in graphene, where the direction of the electromigration force can depend on the specific molecular potential. The collection of techniques for molecular control presented in this dissertation will hopefully one day become useful tools for assembling and operating nanoscale machines.

Appendix A: Capacitive navigation in STM

Due to the relatively small size of typical exfoliated graphene/hBN devices (~30 microns), special techniques are needed to navigate the STM tip onto conductive areas of the device. One method used to achieve this goal is measuring the capacitive pickup current between the tip and graphene sample.[123] By sweeping the tip with the coarse motors across a wide range over the graphene sample, the edges of the graphene can be detected as sharp transitions in the capacitive pickup current. However, due to the presence of the conductive back gate (Si layer), the background capacitance is usually large compared to the small change in capacitance as the tip is swept across the conductive regions of the device. To achieve good contrast, therefore, good background compensation is needed. Practically, one can use the back gate to compensate for the background capacitive current in a typical circuit as shown in Fig. A1. In Fig. A1, the tip-sample, sample-gate, and tip-gate capacitances are represented as $C_{t\text{-}s}$, $C_{s\text{-}g}$, and $C_{t\text{-}g}$. The AC current flowing between tip and sample $\tilde{I}_{t-s}$ can be expressed as

$$\tilde{I}_{t-s} = i\omega C_{t-s}\tilde{V}_S\ , \tag{A.1}$$

where $\tilde{V}_S$ is the oscillation voltage applied to the sample. The AC current flowing between the tip and gate can be expressed as

$$\tilde{I}_{t-g} = i\omega C_{t-g}\tilde{V}_G, \tag{A.2}$$

where $\tilde{V}_G$ is the oscillation voltage applied to the gate. To obtain minimum background capacitive current, one needs to have these two currents cancel each other, such that $\tilde{I}_{t-s} + \tilde{I}_{t-g} = 0$. To achieve this, one can invert the signal $\tilde{V}_S$ (with 180° phase shift) and apply it to the gate while adjusting the signal amplitude with a variable resistor R_{var} such that $C_{t-g}\tilde{V}_G = -C_{t-s}\tilde{V}_S$. Deviations from zero current is then amplified by the STM current preamp and sent to the lock-in for measurement.

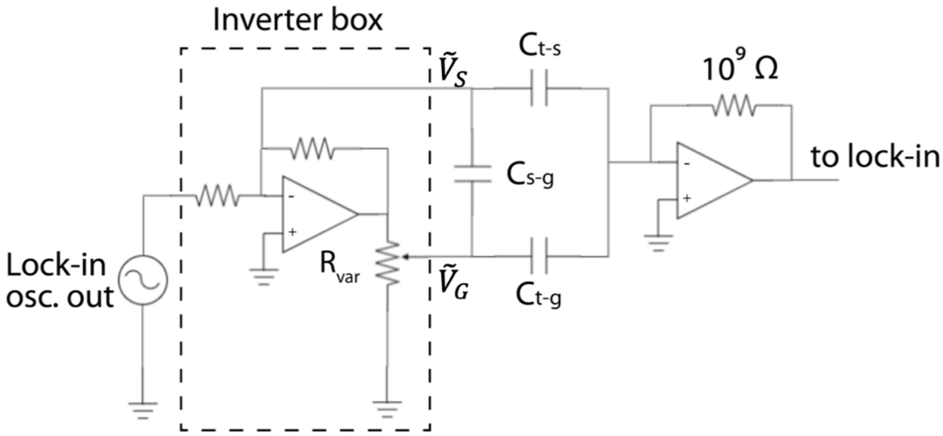

Fig. A1. Capacitive pickup current measurement setup. $C_{t\text{-}s}$ denotes the capacitance between tip and sample, $C_{s\text{-}g}$ denotes the capacitance between sample and back gate, $C_{t\text{-}g}$ denotes the capacitance between tip and back gate.

Fig. A2 (a) shows an SEM image of a typical graphene/hBN FET device contacted by Cr/Au pads. A map of the conductive regions on the device produced by capacitive pickup current scanning is shown in Fig. A2(b). The contour of the graphene, as well as the metal contacts is clearly visible due to a sharp change in tip-sample capacitance as the tip is scanned across from conductive regions to non-conductive regions. Using this method, the STM tip can be safely and reliably navigated onto the graphene device with micron precision.

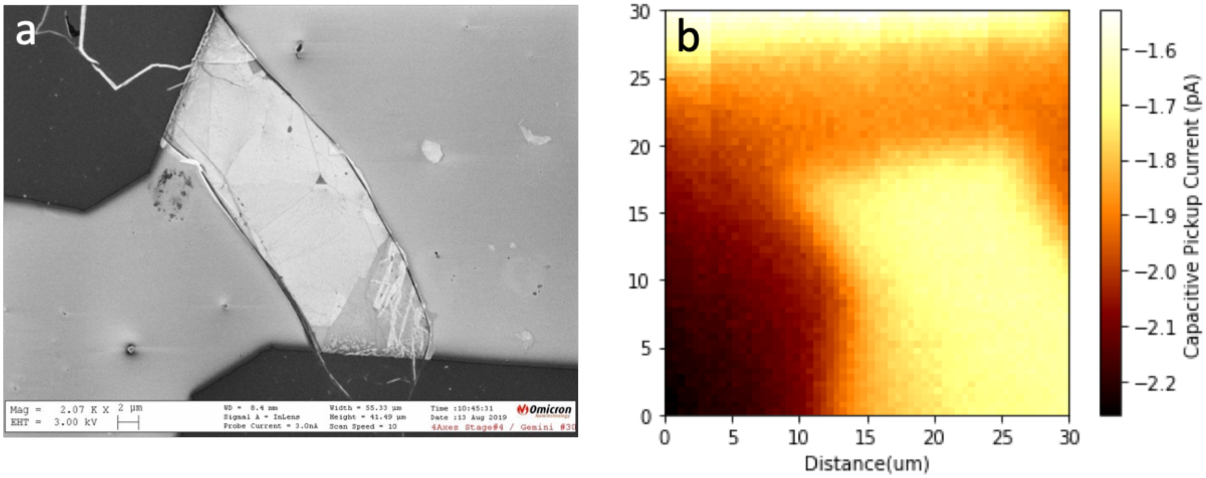

Fig. A2. Graphene device imaged by SEM and capacitive pickup (a) SEM image of a graphene/hBN FET and (b) a map of conductive regions on the device produced by capacitive pickup current scanning. The darker regions correspond to conductive areas consisting of the graphene sheet and two Au electrodes.

Appendix B: Fitting the Dirac Point Energy from STS

In order to obtain the experimental graphene Dirac point energy (E_D), we perform a fit on the scanning tunneling spectroscopy (STS) dI/dV data. The Dirac point causes a dip in the dI/dV spectra, but finding its precise energy is complicated by a well-known phonon gap feature that occurs in graphene STS and which appears in all of our calibrated dI/dV spectra (this gap-like feature is caused by phonon-assisted inelastic tunneling[89]). The phonon gap feature has been shown to span the energy range -65 meV < E < 65 meV and thus offsets spectral features away from the Fermi level by 65 meV.[89,124] Consequently, obtaining the true value of E_D requires that this inelastic offset be taken into account. For ease of fitting, the phonon gap feature can be removed via a simple mathematical algorithm whereby we "cut out" the phonon gap and stitch together the data outside of the phonon gap region by joining the two resulting curves (i.e., the positive and negative bias branches of the dI/dV spectrum) at the Fermi level and then perform a fit on the collapsed data. Due to finite broadening of the phonon gap feature,[124] we stitch together the dI/dV branches starting at ±100 meV to eliminate the phonon gap feature entirely. After finding the energy of the Dirac-point-induced minimum in dI/dV from our fit, we then shift this energy by the known value of the phonon gap (65 meV) to obtain the correct E_D value. The following protocol describes this fitting procedure in detail:

1. We first collapse the dI/dV spectrum by stitching together the dI/dV branches having $|V_b| > 100$ meV at zero energy such that the new values of energy are assigned as $V_b' = V_b - sgn(V_b) \times 100$ meV.

2. We then find the Dirac-point-induced dip in the collapsed dI/dV spectrum about the minimum by using a Gaussian function: $y(V_b') = -ae^{-\frac{(V_b' - b)^2}{c}} + d$.

3. We reverse the collapsing process of step 1 by adding back 100 meV to the fitted value of the parameter b by using $\beta = b + sgn(b) \times 100$ meV.

4. To account for the phonon gap energy, we then subtract the known energy of 65 meV to obtain the final value of E_D: $E_D = \beta - sgn(b) \times 65$ meV.

Bibliography

1. Feynman, R. P., "There's plenty of room at the bottom", *Resonance* **16**, 890 (2011).
2. Crommie, M. F., Lutz, C. P. & Eigler, D. M., "Confinement of Electrons to Quantum Corrals on a Metal Surface", *Science* **262**, 218–220 (1993).
3. Manoharan, H. C., Lutz, C. P. & Eigler, D. M., "Quantum mirages formed by coherent projection of electronic structure", *Nature* **403**, 512–515 (2000).
4. Gomes, K. K., Mar, W., Ko, W., Guinea, F. & Manoharan, H. C., "Designer Dirac fermions and topological phases in molecular graphene", *Nature* **483**, 306–310 (2012).
5. Tsai, H. Z., Lischner, J., Omrani, A. A., Liou, F., Aikawa, A. S., Karrasch, C., Wickenburg, S., Riss, A., Natividad, K. C., Chen, J., Choi, W. W., Watanabe, K., Taniguchi, T., Su, C., Louie, S. G., Zettl, A., Lu, J. & Crommie, M. F., "A molecular shift register made using tunable charge patterns in one-dimensional molecular arrays on graphene", *Nature Electronics* **3**, 598–603 (2020).
6. Huff, T., Labidi, H., Rashidi, M., Livadaru, L., Dienel, T., Achal, R., Vine, W., Pitters, J. & Wolkow, R. A., "Binary atomic silicon logic", *Nature Electronics* **1**, 636–643 (2018).
7. Lipkowski, J. & Ross, P. N., "Electrocatalysis", (1998).
8. Ooka, H., Huang, J. & Exner, K. S., "The Sabatier Principle in Electrocatalysis: Basics, Limitations, and Extensions", *Frontiers in Energy Research* **9**, 1–20 (2021).
9. Marom, R., Amalraj, S. F., Leifer, N., Jacob, D. & Aurbach, D., "A review of advanced and practical lithium battery materials", *Journal of Materials Chemistry* **21**, 9938–9954 (2011).
10. Jagadale, A., Zhou, X., Xiong, R., Dubal, D. P., Xu, J. & Yang, S., "Lithium ion capacitors (LICs): Development of the materials", *Energy Storage Materials* **19**, 314–329 (2019).
11. Frackowiak, E., "Carbon materials for supercapacitor application", *Physical Chemistry Chemical Physics* **9**, 1774–1785 (2007).
12. Sharbati, M. T., Du, Y., Torres, J., Ardolino, N. D., Yun, M. & Xiong, F., "Low-Power, Electrochemically Tunable Graphene Synapses for Neuromorphic Computing", *Advanced Materials* **30**, (2018).
13. Huh, W., Lee, D. & Lee, C.-H., "Memristors Based on 2D Materials as an Artificial Synapse for Neuromorphic Electronics", *Advanced Materials* 2002092 (2020). doi:10.1002/adma.202002092
14. Schedin, F., Geim, A. K., Morozov, S. V., Hill, E. W., Blake, P., Katsnelson, M. I. & Novoselov, K. S., "Detection of individual gas molecules adsorbed on graphene", *Nature Materials* **6**, 652–655 (2007).
15. Agbonlahor, O. G., Muruganathan, M., Imamura, T. & Mizuta, H., "Adsorbed Molecules as Interchangeable Dopants and Scatterers with a Van der Waals Bonding Memory in Graphene Sensors", *ACS Sensors* **5**, 2003–2009 (2020).
16. Cui, K., Mali, K. S., Ivasenko, O., Wu, D., Feng, X., Walter, M., Müllen, K., De Feyter, S. & Mertens, S. F. L., "Squeezing, then stacking: From breathing pores to three-dimensional ionic self-assembly under electrochemical control", *Angewandte Chemie - International Edition* **53**, 12951–12954 (2014).
17. Cui, K., Ivasenko, O., Mali, K. S., Wu, D., Feng, X., Müllen, K., De Feyter, S. & Mertens, S. F. L., "Potential-driven molecular tiling of a charged polycyclic aromatic compound",

Chemical Communications **50**, 10376–10378 (2014).

18. Lee, S. L., Fang, Y., Velpula, G., Cometto, F. P., Lingenfelder, M., Müllen, K., Mali, K. S. & De Feyter, S., "Reversible Local and Global Switching in Multicomponent Supramolecular Networks: Controlled Guest Release and Capture at the Solution/Solid Interface", *ACS Nano* **9**, 11608–11617 (2015).
19. Rasouli, H. R., Kim, J., Mehmood, N., Sheraz, A., Jo, M. K., Song, S., Kang, K. & Kasirga, T. S., "Electric-Field-Induced Reversible Phase Transitions in a Spontaneously Ion-Intercalated 2D Metal Oxide", *Nano Letters* **21**, 3997–4005 (2021).
20. Kühne, M., Börrnert, F., Fecher, S., Ghorbani-Asl, M., Biskupek, J., Samuelis, D., Krasheninnikov, A. V, Kaiser, U. & Smet, J. H., "Reversible superdense ordering of lithium between two graphene sheets", *Nature* **564**, 234–239 (2018).
21. Willke, P., Druga, T., Ulbrich, R. G., Schneider, M. A. & Wenderoth, M., "Spatial extent of a Landauer residual-resistivity dipole in graphene quantified by scanning tunnelling potentiometry", *Nature Communications* **6**, 1–5 (2015).
22. Feenstra, R. M. & Briner, B. G., "The search for residual resistivity dipoles by scanning tunneling potentiometry", *Superlattices and Microstructures* **23**, 699–709 (1998).
23. Tao, C., Cullen, W. G. & Williams, E. D., "Visualizing the electron scattering force in nanostructures", *Science* **328**, 736–740 (2010).
24. Homoth, J., Wenderoth, M., Druga, T., Winking, L., Ulbrich, R. G., Bobisch, C. A., Weyers, B., Bannani, A., Zubkov, E., Bernhart, A. M., Kaspers, M. R. & Mo, R., "Electronic Transport on the Nanoscale : Ballistic Transmission and Ohm ' s Law 2009", (2009).
25. Clark, K. W., Zhang, X. G., Vlassiouk, I. V., He, G., Feenstra, R. M. & Li, A. P., "Spatially resolved mapping of electrical conductivity across individual domain (Grain) boundaries in graphene", *ACS Nano* **7**, 7956–7966 (2013).
26. Wickenburg, S., Lu, J., Lischner, J., Tsai, H.-Z., Omrani, A. A., Riss, A., Karrasch, C., Bradley, A., Jung, H. S., Khajeh, R., Wong, D., Watanabe, K., Taniguchi, T., Zettl, A., Neto, A. H. C., Louie, S. G. & Crommie, M. F., "Tuning charge and correlation effects for a single molecule on a graphene device", *Nature Communications* **7**, 13553 (2016).
27. Lee, J., Wong, D., Velasco Jr, J., Rodriguez-Nieva, J. F., Kahn, S., Tsai, H.-Z., Taniguchi, T., Watanabe, K., Zettl, A., Wang, F., Levitov, L. S. & Crommie, M. F., "Imaging electrostatically confined Dirac fermions in graphene quantum dots", *Nature Physics* **12**, 1032–1036 (2016).
28. Ge, Z., Wong, D., Lee, J., Joucken, F., Quezada-Lopez, E. A., Kahn, S., Tsai, H.-Z., Taniguchi, T., Watanabe, K., Wang, F., Zettl, A., Crommie, M. F. & Velasco, J. J., "Imaging Quantum Interference in Stadium-Shaped Monolayer and Bilayer Graphene Quantum Dots", *Nano Letters* **21**, 8993–8998 (2021).
29. Li, S., Chen, S., Li, J., Wu, R. & Ho, W., "Joint Space-Time Coherent Vibration Driven Conformational Transitions in a Single Molecule", *Physical Review Letters* **119**, 176002 (2017).
30. Cocker, T. L., Peller, D., Yu, P., Repp, J. & Huber, R., "Tracking the ultrafast motion of a single molecule by femtosecond orbital imaging", *Nature* **539**, 263–267 (2016).
31. Magnussen, O. M. & Groß, A., "Toward an Atomic-Scale Understanding of Electrochemical Interface Structure and Dynamics", *Journal of the American Chemical Society* **141**, 4777–4790 (2019).
32. Matsushima, H., Lin, S. W., Morin, S. & Magnussen, O. M., "In situ video-STM studies

of the mechanisms and dynamics of electrochemical bismuth nanostructure formation on Au", *Faraday Discussions* **193**, 171–185 (2016).

33. Tansel, T. & Magnussen, O. M., "Video STM studies of adsorbate diffusion at electrochemical interfaces", *Physical Review Letters* **96**, 2–5 (2006).
34. Liou, F., Tsai, H.-Z. Z., Aikawa, A. S., Natividad, K. C., Tang, E., Ha, E., Riss, A., Watanabe, K., Taniguchi, T., Lischner, J., Zettl, A. & Crommie, M. F., "Imaging Reconfigurable Molecular Concentration on a Graphene Field-Effect Transistor", *Nano Letters* **21**, 8770–8776 (2021).
35. Ugeda, M. M., Bradley, A. J., Shi, S. F., Da Jornada, F. H., Zhang, Y., Qiu, D. Y., Ruan, W., Mo, S. K., Hussain, Z., Shen, Z. X., Wang, F., Louie, S. G. & Crommie, M. F., "Giant bandgap renormalization and excitonic effects in a monolayer transition metal dichalcogenide semiconductor", *Nature Materials* **13**, 1091–1095 (2014).
36. Mak, K. F. & Shan, J., "Photonics and optoelectronics of 2D semiconductor transition metal dichalcogenides", *Nature Photonics* **10**, 216–226 (2016).
37. Oh, S., Crommie, M. F. & Cohen, M. L., "Simulating the Nanomechanical Response of Cyclooctatetraene Molecules on a Graphene Device", *ACS Nano* **13**, 1713–1718 (2019).
38. Bozhko, S. I., Krasnikov, S. A., Lübben, O., Murphy, B. E., Radican, K., Semenov, V. N., Wu, H.-C., Levchenko, E. A., Chaika, A. N., Sergeeva, N. N. & Shvets, I. V, "Correlation between charge-transfer and rotation of C60 on WO2/W(110)", *Nanoscale* **5**, 3380–3386 (2013).
39. Castro Neto, A. H., Guinea, F., Peres, N. M. R., Novoselov, K. S. & Geim, A. K., "The electronic properties of graphene", *Reviews of Modern Physics* **81**, 109–162 (2009).
40. Lechner, C. & Sax, A. F., "Adhesive Forces Between Aromatic Molecules and Graphene", *The Journal of Physical Chemistry C* **118**, 20970–20981 (2014).
41. González-Herrero, H., Gómez-Rodríguez, J. M., Mallet, P., Moaied, M., Palacios, J. J., Salgado, C., Ugeda, M. M., Veuillen, J. Y., Yndurain, F. & Brihuega, I., "Atomic-scale control of graphene magnetism by using hydrogen atoms", *Science* **352**, 437–441 (2016).
42. Vijayarangamuthu, K., Ahn, S., Seo, H., Yoon, S. H., Park, C. M. & Jeon, K. J., "Temporospatial Control of Graphene Wettability", *Advanced Materials* **28**, 661–667 (2016).
43. de la Torre, B., Švec, M., Hapala, P., Redondo, J., Krejčí, O., Lo, R., Manna, D., Sarmah, A., Nachtigallová, D., Tuček, J., Błoński, P., Otyepka, M., Zbořil, R., Hobza, P. & Jelínek, P., "Non-covalent control of spin-state in metal-organic complex by positioning on N-doped graphene", *Nature Communications* **9**, 1–9 (2018).
44. Bardeen, J., "Tunneling from a many-particle point of view", *Physical Review* **131**, 1083–1086 (1963).
45. Tersoff, J. & Hamann, D. R., "Theory of the scanning tunneling microscope", *Physical Review B* **31**, 805–813 (1985).
46. Sakurai, J. J. & Napolitano, J., "*Modern Quantum Mechanics*", (Cambridge University Press, 2017). doi:DOI: 10.1017/9781108499996
47. S., N. K., K., G. A., V., M. S., D., J., Y., Z., V., D. S., V., G. I. & A., F. A., "Electric Field Effect in Atomically Thin Carbon Films", *Science* **306**, 666–669 (2004).
48. Lee, J., Wong, D., Velasco, J., Rodriguez-Nieva, J. F., Kahn, S., Tsai, H. Z., Taniguchi, T., Watanabe, K., Zettl, A., Wang, F., Levitov, L. S. & Crommie, M. F., "Imaging electrostatically confined Dirac fermions in graphene quantum dots", *Nature Physics* **12**, 1032–1036 (2016).

49. Wehling, T. O., Balatsky, A. V., Katsnelson, M. I., Lichtenstein, A. I., Scharnberg, K. & Wiesendanger, R., "Local electronic signatures of impurity states in graphene", *Physical Review B - Condensed Matter and Materials Physics* **75**, 1–5 (2007).
50. Wehling, T. O., Novoselov, K. S., Morozov, S. V., Vdovin, E. E., Katsnelson, M. I., Geim, A. K. & Lichtenstein, A. I., "Molecular doping of graphene", *Nano Letters* **8**, 173–177 (2008).
51. Ohta, T., Bostwick, A., Seyller, T., Horn, K. & Rotenberg, E., "Controlling the electronic structure of bilayer graphene", *Science* **313**, 951–954 (2006).
52. Xia, J., Chen, F., Li, J. & Tao, N., "Measurement of the quantum capacitance of graphene", *Nature Nanotechnology* **4**, 505–509 (2009).
53. Likharev, K. K., "Phase transitions", in *Statistical Mechanics: Lecture notes* 4–41 (IOP Publishing, 2019). doi:10.1088/2053-2563/aaf503ch4
54. Rehn, D. A., Li, Y., Pop, E. & Reed, E. J., "Theoretical potential for low energy consumption phase change memory utilizing electrostatically-induced structural phase transitions in 2D materials", *npj Computational Materials* **4**, (2018).
55. Kapfer, S. C. & Krauth, W., "Two-dimensional melting: From liquid-hexatic coexistence to continuous transitions", *Physical Review Letters* **114**, 1–5 (2015).
56. Schroeder, D. V, "*An introduction to thermal physics*", (Addison Wesley, 2000).
57. Ashcroft, N. W. & Mermin, N. D., "The Semiclassical Theory of Conduction in Metals", in *Solid State Physics* 244–250 (Holt-Saunders, 1976).
58. Wehling, T. O., Yuan, S., Lichtenstein, A. I., Geim, A. K. & Katsnelson, M. I., "Resonant Scattering by Realistic Impurities in Graphene", *Physical Review Letters* **105**, 56802 (2010).
59. Robinson, J. P., Schomerus, H., Oroszlány, L. & Fal'Ko, V. I., "Adsorbate-limited conductivity of graphene", *Physical Review Letters* **101**, 7–10 (2008).
60. Chen, J.-H., Jang, C., Adam, S., Fuhrer, M. S., Williams, E. D. & Ishigami, M., "Charged-impurity scattering in graphene", *Nature Physics* **4**, 377–381 (2008).
61. Yan, J. & Fuhrer, M. S., "Correlated charged impurity scattering in graphene", *Physical Review Letters* **107**, 1–5 (2011).
62. Regan, B. C., Aloni, S., Ritchie, R. O., Dahmen, U. & Zettl, A., "Carbon nanotubes as nanoscale mass conveyors", *Nature* **428**, 924–927 (2004).
63. Solenov, D. & Velizhanin, K. A., "Adsorbate transport on graphene by electromigration", *Physical Review Letters* **109**, 1–5 (2012).
64. Velizhanin, K. A., Dandu, N. & Solenov, D., "Electromigration of bivalent functional groups on graphene", *Physical Review B* **89**, 155414 (2014).
65. Huntington, H. B., "*Electromigration in metals*", *Diffusion in solids: recent developments* (Academic Press New York, 1975).
66. Knaak, J. & Eichenauer, W., "Die wanderung von protonen und deuteronen in palladium unter einfluß eines elektrischen feldes", *Zeitschrift fur Naturforschung - Section A Journal of Physical Sciences* **23**, 1783–1789 (1968).
67. Landauer, R., "Spatial variation of currents and fields due to localized scatterers in metallic conduction", *IBM Journal of Research and Development* **44**, 251–259 (2000).
68. Sorbello, R. S., "*Theory of Electromigration*", *Solid State Physics - Advances in Research and Applications* **51**, (1998).
69. Bevan, K. H., Zhu, W., Stocks, G. M., Guo, H. & Zhang, Z., "Local fields in conductor surface electromigration: A first-principles study in the low-bias ballistic limit", *Physical*

Review B - Condensed Matter and Materials Physics **85**, 1–9 (2012).

70. Bevan, K. H., Guo, H., Williams, E. D. & Zhang, Z., "First-principles quantum transport theory of the enhanced wind force driving electromigration on Ag(111)", *Physical Review B - Condensed Matter and Materials Physics* **81**, 1–9 (2010).
71. Bly, D. & Rous, P., "Theoretical study of the electromigration wind force for adatom migration at metal surfaces", *Physical Review B - Condensed Matter and Materials Physics* **53**, 13909–13920 (1996).
72. Datta, S., "*Electronic Transport in Mesoscopic Systems*", *Cambridge Studies in Semiconductor Physics and Microelectronic Engineering* (Cambridge University Press, 1995). doi:DOI: 10.1017/CBO9780511805776
73. Barreiro, A., Rurali, R., Hernández, E. R. & Bachtold, A., "Structured graphene devices for mass transport", *Small* **7**, 775–780 (2011).
74. Feenstra, R. M. & Martenssson, P., "Fermi-Level Pinning at the Sb/GaAs(110) Surface Studied by Scanning Tunneling Spectroscopy", *Physical Review Letters* **61**, 447–450 (1988).
75. Spicer, W. E., Newman, N., Spindt, C. J., Liliental-Weber, Z. & Weber, E. R., "““Pinning”” and Fermi level movement at GaAs surfaces and interfaces", *Journal of Vacuum Science & Technology A: Vacuum, Surfaces, and Films* **8**, 2084–2089 (1990).
76. Grassman, T. J., Bishop, S. R. & Kummel, A. C., "An atomic view of Fermi level pinning of Ge(100) by O2", *Surface Science* **602**, 2373–2381 (2008).
77. Hurdax, P., Hollerer, M., Puschnig, P., Lüftner, D., Egger, L., Ramsey, M. G. & Sterrer, M., "Controlling the Charge Transfer across Thin Dielectric Interlayers", *Advanced Materials Interfaces* **7**, 1–7 (2020).
78. Sharbati, M. T., Du, Y., Torres, J., Ardolino, N. D., Yun, M. & Xiong, F., "Low-Power, Electrochemically Tunable Graphene Synapses for Neuromorphic Computing", *Advanced Materials* **30**, 1–6 (2018).
79. Cai, Z. F., Yan, H. J., Wang, D. & Wan, L. J., "Potential- and concentration-dependent self-assembly structures at solid/liquid interfaces", *Nanoscale* **10**, 3438–3443 (2018).
80. Pinto, H., Jones, R., Goss, J. P. & Briddon, P. R., "P-type doping of graphene with F4-TCNQ", *Journal of Physics Condensed Matter* **21**, 23–26 (2009).
81. Barja, S., Garnica, M., Hinarejos, J. J., Vázquez De Parga, A. L., Martín, N. & Miranda, R., "Self-organization of electron acceptor molecules on graphene", *Chemical Communications* (2010).
82. Khomyakov, P. A., Giovannetti, G., Rusu, P. C., Brocks, G., Van Den Brink, J. & Kelly, P. J., "First-principles study of the interaction and charge transfer between graphene and metals", *Physical Review B - Condensed Matter and Materials Physics* (2009). doi:10.1103/PhysRevB.79.195425
83. Kumar, A., Banerjee, K., Dvorak, M., Schulz, F., Harju, A., Rinke, P. & Liljeroth, P., "Charge-Transfer-Driven Nonplanar Adsorption of F4TCNQ Molecules on Epitaxial Graphene", *ACS Nano* **11**, 4960–4968 (2017).
84. Coletti, C., Riedl, C., Lee, D. S., Krauss, B., Patthey, L., Von Klitzing, K., Smet, J. H. & Starke, U., "Charge neutrality and band-gap tuning of epitaxial graphene on SiC by molecular doping", *Physical Review B - Condensed Matter and Materials Physics* **81**, 1–8 (2010).
85. Akiyoshi, H., Goto, H., Uesugi, E., Eguchi, R., Yoshida, Y., Saito, G. & Kubozono, Y., "Carrier Accumulation in Graphene with Electron Donor/Acceptor Molecules", *Advanced*

Electronic Materials **1**, 1–5 (2015).

86. Lu, J., Tsai, H.-Z., Tatan, A. N., Wickenburg, S., Omrani, A. A., Wong, D., Riss, A., Piatti, E., Watanabe, K., Taniguchi, T., Zettl, A., Pereira, V. M. & Crommie, M. F., "Frustrated supercritical collapse in tunable charge arrays on graphene", *Nature Communications* **10**, 477 (2019).
87. Pavliček, N., Swart, I., Niedenführ, J., Meyer, G. & Repp, J., "Symmetry dependence of vibration-assisted tunneling", *Physical Review Letters* **110**, 1–5 (2013).
88. Qiu, X. H., Nazin, G. V. & Ho, W., "Vibronic states in single molecule electron transport", *Physical Review Letters* **92**, 1–4 (2004).
89. Zhang, Y., Brar, V. W., Wang, F., Girit, C., Yayon, Y., Panlasigui, M., Zettl, A. & Crommie, M. F., "Giant phonon-induced conductance in scanning tunnelling spectroscopy of gate-tunable graphene", *Nature Physics* **4**, 627–630 (2008).
90. Decker, R., Wang, Y., Brar, V. W., Regan, W., Tsai, H.-Z., Wu, Q., Gannett, W., Zettl, A. & Crommie, M. F., "Local Electronic Properties of Graphene on a BN Substrate via Scanning Tunneling Microscopy", *Nano Letters* **11**, 2291–2295 (2011).
91. Järvinen, P., Hämäläinen, S. K., Banerjee, K., Häkkinen, P., Ijäs, M., Harju, A. & Liljeroth, P., "Molecular self-assembly on graphene on SiO2 and h-BN substrates", *Nano Letters* **13**, 3199–3204 (2013).
92. Cochrane, K. A., Schiffrin, A., Roussy, T. S., Capsoni, M. & Burke, S. A., "Pronounced polarization-induced energy level shifts at boundaries of organic semiconductor nanostructures", *Nature Communications* **6**, (2015).
93. Nakamuro, T., Sakakibara, M., Nada, H., Harano, K. & Nakamura, E., "Capturing the Moment of Emergence of Crystal Nucleus from Disorder", *Journal of the American Chemical Society* **143**, 1763–1767 (2021).
94. Hannon, J. B., Hibino, H., Bartelt, N. C., Swartzentruber, B. S., Ogino, T. & Kellogg, G. L., "Dynamics of the silicon (111) surface phase transition", *Nature* **405**, 552–554 (2000).
95. Pedramrazi, Z., Herbig, C., Pulkin, A., Tang, S., Phillips, M., Wong, D., Ryu, H., Pizzochero, M., Chen, Y., Wang, F., Mele, E. J., Shen, Z.-X., Mo, S.-K., Yazyev, O. V & Crommie, M. F., "Manipulating Topological Domain Boundaries in the Single-Layer Quantum Spin Hall Insulator 1T′–WSe2", *Nano Letters* **19**, 5634–5639 (2019).
96. Alessandrini, A. & Facci, P., "Phase transitions in supported lipid bilayers studied by AFM", *Soft Matter* **10**, 7145–7164 (2014).
97. Xiang, W., Yang, N., Li, X., Linnemann, J., Hagemann, U., Ruediger, O., Heidelmann, M., Falk, T., Aramini, M., DeBeer, S., Muhler, M., Tschulik, K. & Li, T., "3D atomic-scale imaging of mixed Co-Fe spinel oxide nanoparticles during oxygen evolution reaction", *Nature Communications* **13**, 1–14 (2022).
98. Xu, L., Wang, L., Liu, H., Li, F., Li, D., Cao, Y., Wu, C. C., Bai, X. & Qi, J., "Atomic-scale dynamics of the phase transition in bilayer PtSe2", *Journal of Materials Chemistry C* **9**, 5261–5266 (2021).
99. Li, B., Zhou, D. & Han, Y., "Assembly and phase transitions of colloidal crystals", *Nature Reviews Materials* **1**, 1–13 (2016).
100. Kim, M. & Chelikowsky, J. R., "CO tip functionalization in subatomic resolution atomic force microscopy", *Applied Physics Letters* **107**, (2015).
101. Hansen, J.-P. & McDonald, I. R., "Static Properties of Liquids: Thermodynamics and Structure", in *Theory of Simple Liquids* (eds. HansenJ.-P. & McDonaldI. R. B. T.-T. of S. L. (Third E.) 46–77 (Academic Press, 2006). doi:https://doi.org/10.1016/B978-

012370535-8/50005-7
102. Wong, C. & Yang, R. T., "Surface Diffusion", *Catalysis Reviews* **31**, 129–214 (1989).
103. Vlachos, D. G., Schmidt, L. D. & Aris, R., "The effects of phase transitions, surface diffusion, and defects on surface catalyzed reactions: Fluctuations and oscillations", *The Journal of Chemical Physics* **93**, 8306–8313 (1990).
104. Medveď, I. & Černý, R., "Surface diffusion in porous media: A critical review", *Microporous and Mesoporous Materials* **142**, 405–422 (2011).
105. Choi, J. G., Do, D. D. & Do, H. D., "Surface diffusion of adsorbed molecules in porous media: Monolayer, multilayer, and capillary condensation regimes", *Industrial and Engineering Chemistry Research* **40**, 4005–4031 (2001).
106. Debenedetti, P. G. & Stillinger, F. H., "Supercooled liquids and the glass transition", *Nature* **410**, 259 (2001).
107. Pérez-Castañeda, T., Rodríguez-Tinoco, C., Rodríguez-Viejo, J. & Ramos, M. A., "Suppression of tunneling two-level systems in ultrastable glasses of indomethacin", *Proceedings of the National Academy of Sciences of the United States of America* **111**, 11275–11280 (2014).
108. Repp, J., Steurer, W., Scivetti, I., Persson, M., Gross, L. & Meyer, G., "Charge-State-Dependent Diffusion of Individual Gold Adatoms on Ionic Thin NaCl Films", *Physical Review Letters* **117**, 1–5 (2016).
109. Allan, D. B., Caswell, T., Keim, N. C., van der Wel, C. M. & Verweij, R. W., "soft-matter/trackpy: Trackpy v0.5.0", (2021). doi:10.5281/ZENODO.4682814
110. Sini, G., Sears, J. S. & Brédas, J. L., "Evaluating the performance of DFT functionals in assessing the interaction energy and ground-state charge transfer of donor/acceptor complexes: Tetrathiafulvalene-tetracyanoquinodimethane (TTF-TCNQ) as a model case", *Journal of Chemical Theory and Computation* **7**, 602–609 (2011).
111. Steinmann, S. N., Piemontesi, C., Delachat, A. & Corminboeuf, C., "Why are the interaction energies of charge-transfer complexes challenging for DFT?", *Journal of Chemical Theory and Computation* **8**, 1629–1640 (2012).
112. Bediako, D. K., Rezaee, M., Yoo, H., Larson, D. T., Zhao, S. Y. F., Taniguchi, T., Watanabe, K., Brower-Thomas, T. L., Kaxiras, E. & Kim, P., "Heterointerface effects in the electrointercalation of van der Waals heterostructures", *Nature* **558**, 425–429 (2018).
113. Zhao, S. Y. F., Elbaz, G. A., Bediako, D. K., Yu, C., Efetov, D. K., Guo, Y., Ravichandran, J., Min, K. A., Hong, S., Taniguchi, T., Watanabe, K., Brus, L. E., Roy, X. & Kim, P., "Controlled Electrochemical Intercalation of Graphene/h-BN van der Waals Heterostructures", *Nano Letters* **18**, 460–466 (2018).
114. Yao, M., Sano, H., Ando, H. & Kiyobayashi, T., "Molecular ion battery: A rechargeable system without using any elemental ions as a charge carrier", *Scientific Reports* **5**, 1–8 (2015).
115. Yan, J. & Fuhrer, M. S., "Correlated Charged Impurity Scattering in Graphene", *Physical Review Letters* **107**, 206601 (2011).
116. Shi, Y., Liang, X., Yuan, B., Chen, V., Li, H., Hui, F., Yu, Z., Yuan, F., Pop, E., Wong, H.-S. P. & Lanza, M., "Electronic synapses made of layered two-dimensional materials", *Nature Electronics* **1**, 458–465 (2018).
117. Das, A. K. & Peierls, R., "The force of electromigration", *Journal of Physics C: Solid State Physics* **8**, 3348–3352 (1975).
118. Tsutsui, M. & Taniguchi, M., "Single Molecule Electronics and Devices", *Sensors* **12**,

7259–7298 (2012).
119. Heinze, S., Wang, N. P. & Tersoff, J., "Electromigration forces on ions in carbon nanotubes", *Physical Review Letters* **95**, 28–31 (2005).
120. Choi, Y. W. & Cohen, M. L., "Resonantly Enhanced Electromigration Forces for Adsorbates on Graphene", *Physical Review Letters* (2022).
121. Solenov, D. & Velizhanin, K. A., "Adsorbate Transport on Graphene by Electromigration", *Physical Review Letters* **109**, 95504 (2012).
122. Di Ventra, M. & Pantelides, S. T., "Hellmann-Feynman theorem and the definition of forces in quantum time-dependent and transport problems", *Physical Review B* **61**, 16207–16212 (2000).
123. Li, G., Luican, A. & Andrei, E. Y., "Self-navigation of a scanning tunneling microscope tip toward a micron-sized graphene sample", *Review of Scientific Instruments* **82**, (2011).
124. Brar, V. W., Wickenburg, S., Panlasigui, M., Park, C.-H., Wehling, T. O., Zhang, Y., Decker, R., Girit, Ç., Balatsky, A. V., Louie, S. G., Zettl, A. & Crommie, M. F., "Observation of Carrier-Density-Dependent Many-Body Effects in Graphene via Tunneling Spectroscopy", *Physical Review Letters* **104**, 036805 (2010).